University of Alberta

ELECTRICAL PROPERTIES OF AL-GE GRANULAR SUPERCONDUCTING FILMS

by

Yikai Yang

A thesis submitted to the Faculty of Graduate Studies and Research
in partial fulfillment of the requirements for the degree of

Master of Science

Department of Physics

Spring 2014
Edmonton, Alberta

In memory of my beloved mother, who brought me life and joy.

Abstract

A granular superconductor is a system that consists of two types of materials, one is superconducting, and the other is insulating. Instead of alloying, these two materials form a granular structure where superconducting grains are embedded in an insulating matrix. This is a seemingly simple structure, yet has complicated consequences that, to this day, physicists don't fully comprehend. In this dissertation, I will first give a brief review of the background theories and the development of the field of granular superconductors. Then account in details how we conducted a series of resistivity measurements with and without magnetic field. In the last part, I will also make an attempt to analyze the recent results we obtained and hopefully will shine light on the mystery of granular superconductors.

Acknowledgements

If anyone in the future would ever open and read this thesis, it is most likely to be someone pursuing an academic career or ambition through a graduate school. Then he or she must know how lonely and arduous is this journey, and more importantly, how precious are the favours done by other people down the road. I personally found this couldn't be more true in the past two years of my Master's program. I would like to, first of all, thank my families for their support extended for thousands of miles from home to me. A big "thank you" goes to my supervisor, Dr. John P. Davis, for his effort in preparing me into a true physicist. If one day, I am able to enrol into a Ph.D. program and somehow survive it, it is of much due to his training for me. I am also going to gladly express my gratitude to my colleagues who showed me the real definition of teamwork. Among these fine scientists, I'd like specially thank Dr. X. Rojas, with whom I shared the low temperature lab of our group, for his helpful explanations, demonstrations, and discussions. Throughout the two years of graduate study, I encountered and benefited from so many brilliant professors, in addition to my own supervisor, that I cannot enumerate all the names. Yet hereby I feel much obliged to thank Prof. K. Beach, Prof. F. Marsiglio, and Prof. J. Beamish for the knowledge they shared with me with patience, which were keys to my success in obtaining this degree. Last but not the least, I cannot spare four additional names from my thank list here: Greg Popowich, Don Mullin, Paul Zimmermann, and Tony Paget. Without their expertise and favours upon me, none of my experiments would even start to work.

Contents

List of Tables

List of Figures

Chapter 1

Introduction

1.1 Historical review of the history of superconductivity

Despite the fact that this thesis will focus mostly on granular superconductivity, the author decided it is helpful to see the whole picture by starting this dissertation with a glance at the entire area of superconductivity. Thus this section will be my attempt to document some of the most important established facts and theories about superconductivity.

1.1.1 Discovery of superconductivity

The well known Dutch physicist, and Nobel laureate, Heike Kamerlingh Onnes was the first scientist to discover superconductivity when studying the low temperature properties of pure metals [1]. Since then, many known metals have turned out to be superconducting at low temperatures. Below is a table (figure 1.1) taken from ref. [2] of a list of the transition temperatures of some superconductors.

For superconductors, the most prominent phenomenon is the occurrence of zero resistivity. Demonstrated in figure 1.2 is a typical resistivity curve as a function of temperature of a superconductor, the outstanding feature is that the resistivity of the sample suddenly drops from some finite value to zero at a certain temperature, which is called the superconducting transition temper-

substance	Tc (K)	
Al	1.2	
Hg	4.1	first superconductor, discovered 1911
Nb	9.3	higest T_c of an element at normal pressure
Pb	7.2	
Sn	3.7	
Ti	0.39	
Tl	2.4	
V	5.3	
W	0.01	
Zn	0.88	
Zr	0.65	
Fe	2	high pressure
H	300	predicted, under high pressure
O	30	high pressure, maximum T_c of any element
S	10	high pressure
Nb_3Ge	23	A15 structure, highest known T_c before 1986
$Ba_{1-x}Pb_xBiO_3$	12	first perovskite oxide structure
$La_{2-x}Sr_xCuO_4$	35	first high T_c superconductor
$YBa_2Cu_3O_{7-\delta}$	92	first superconductor above 77K
$HgBa_2Ca_2Cu_3O_{8+\delta}$	135-165	highest T_c ever recorded
K_3 C_{60}	30	fullerene molecules
YNi_2B_2C	17	borocarbide superconductor
MgB_2	38	discovery announced in January 2001
Sr_2RuO_4	1.5	possible p-wave superconductor
UPt_3	0.5	"heavy fermion" exotic superconductor
$(TMTSF)_2ClO_4$	1.2	organic molecular superconductor
ET-BEDT	12	organic molecular superconductor

Figure 1.1: A list of the superconducting transition temperatures for some superconductors. Table taken with permission from ref. [2].

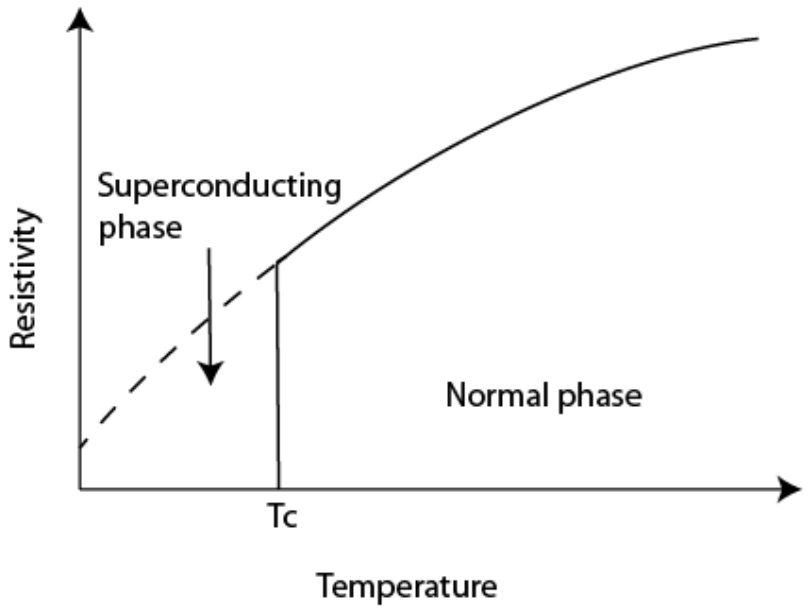

Figure 1.2: A generic resistivity curve as a function of temperature for a superconductor.

ature (denoted by T_c). It is now known that this is a sign of a superconductor going through a thermodynamic phase transition from the normal state to a superconducting state. This sudden change in resistivity indicates an abrupt disappearance of electric field inside the superconductor, according to a fundamental law of electrodynamics: $\mathbf{E} = \rho\mathbf{j}$. By the definition of conductivity, $\mathbf{j} = \sigma\mathbf{E}$, it is then obvious that in order to have finite current in the material, it must be true that the conductivity of the material is infinite at this point. Thus the electric current will go through the sample without any dissipation. If we were to make a ring from such a superconductor, inject an electrical current into it, and cool it down below its transition temperature, then the current should never decay. This is indeed true, as a similar experiment has been conducted [3], and the result verified as postulated. This proves valid the statement that a material in the superconducting state has absolute zero electrical resistance as if it is an "ideal" conductor. However, the current that exists in a superconductor cannot be infinitely large, and experiments show that there is a current threshold (known as the critical current, denoted by I_c) above which the superconductivity will be destroyed. This current threshold is an innate character of each individual superconductor [4].

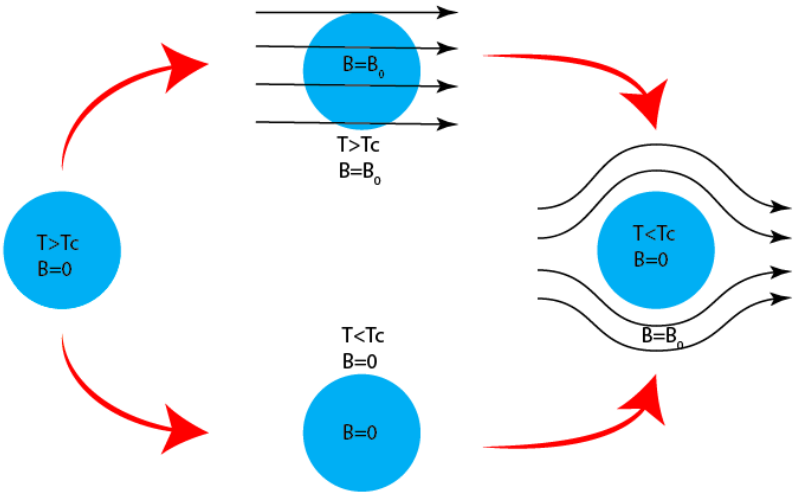

Figure 1.3: A schematic demonstration of the Meissner-Ochsenfeld effect.

Superconductivity and magnetic field

One of the striking and characteristic phenomena of superconductors is that they are perfect diamagnetic materials when becoming superconducting, as long as there isn't a too strong external magnetic field that prevents it. It is called the Meissner-Ochsenfeld effect, which can be illustrated as in figure 1.3: the external magnetic field will be expelled from the inside of the material once it becomes superconducting. This can be achieve, either by applying a magnetic field first and then dropping the temperature to below transition temperature (the upper path of figure 1.3), or by first lowering the temperature to below transition temperature first before any applying magnetic field (the lower path of figure 1.3). This feature implies that a superconductor is not equivalent to an ideal conductor. In an ideal conductor where resistivity is zero below some certain temperature, if we take the upper path of figure 1.3, then the magnetic field will be trapped inside of the conductor once it become "ideal" and has no reason to be expelled from the material. Therefore a zero resistivity material is not necessarily a superconductor, and consequently not an adequate definition of superconductor.

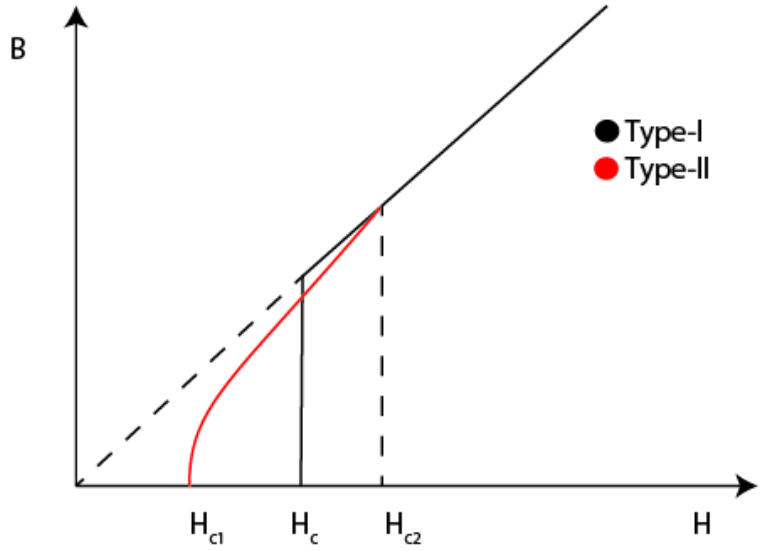

Figure 1.4: Magnetization curve of type-I and type-II superconductors [5].

Type-I and type-II superconductors

Starting from the Meissner-Ochsenfeld effect, behavioural differences further divide various superconductors into mainly two categories: type-I and type-II superconductors. In short, a type-I superconductor is a superconductor that is either in the Meissner state, when the external magnetic field is completely expelled from the material, or in normal state, when superconductivity is destroyed by a too strong magnetic field or a too high temperature. As for type-II superconductors, there exists one additional state between the Meissner state and the normal state, an intermediate state (Abrikosov state/phase) where the normal and the superconducting states both exist but in different parts of the material.

One way to show this difference between the two types of superconductors is by comparing the magnetization curves as a function of external magnetic field as in figure 1.4. As seen in figure 1.4, the absent linear part (indicated by the dashed line extended along the magnetization curve) of the magnetization curve of type-I superconductor is when the magnetic flux is expelled from the sample, and thus the field inside of the material is zero. The linear part of the curve above "H_c" (known as the critical field) is where the field is too strong

and superconductivity is completely suppressed, the material is now simply paramagnetic. On the contrary, the magnetization curve of a type-II superconductor appears to be more complicated as there is a non-linear part of the curve between the total absent part and paramagnetic part. This non-linear magnetization curve takes place when the external field starts to penetrate the material, destroying superconductivity in some regions but not all at once, and as the strength of the field goes higher and higher, more and more flux enters the superconductor and more and more regions become "normal." In the end, the entire sample enters the normal state, and becomes paramagnetic as in the case of type-I superconductors. A real world picture of the Abrikosov state is illustrated in figure 1.5(a), in which we can see magnetic flux lines penetrate a superconductor through some well defined channels. In fact, these channels are surrounded by persistent supercurrent, separating them from the superconducting regions in the form of vortices. In experiments, these vortices have been observed multiple times under microscopes, an example is shown in figure 1.5(b).

Another way of seeing this behavioural difference between type-I and type-II superconductors is by looking at differences between their critical fields (the field above which superconductivity is suppressed) as functions of temperature. A generic comparison of such is shown in figure 1.6(a) and 1.6(b), in which we find that the curve for type-II superconductor branches into two from its onset while that of type-I superconductor doesn't. Experimentally, it is relatively easy to measure H_c for type-I superconductors or H_{c2} (upper critical field) for type-II superconductors, as above these two curves, superconductivity is completely suppressed in both types of superconductors, a simple resistance measurement can map out the curve. However, it is much different and more difficult to map out H_{c1} (lower critical field) for type-II superconductors since that, superconductivity still exists in the material when it is in the region (Abrikosov state) between H_{c1} and H_{c2}, and as long as there is an electrical short between leads for resistance measurement, one wouldn't be able to tell from resistance measurement the different between states above and below the H_{c1} curves. Therefore, if one hopes to map out the H_{c1} curves for type-II superconductors, an alternative method other than resistivity measurement has to be used, such as neutron scattering, nuclear magnetic resonance (NMR)

measurement, or magnetization relaxation etc.

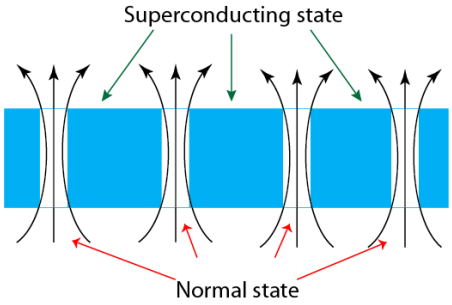

(a) Side view of a schematic drawing of a superconductor sample in Abrikosov state. Arrows in the graph indicates flux lines of magnetic field.

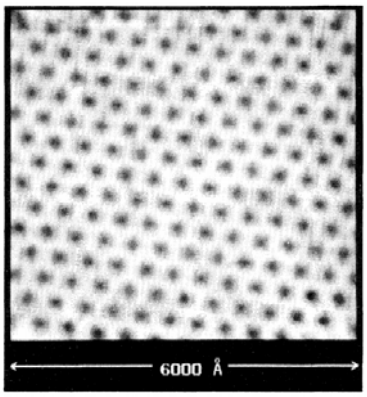

(b) STM image (above view) of vortices in a superconductor. Photo credits to [6].

Figure 1.5: Abrikosov state of type-II superconductor.

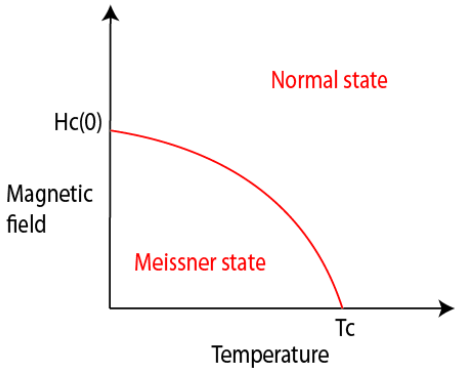

(a) Critical magnetic field of type-I superconductor.

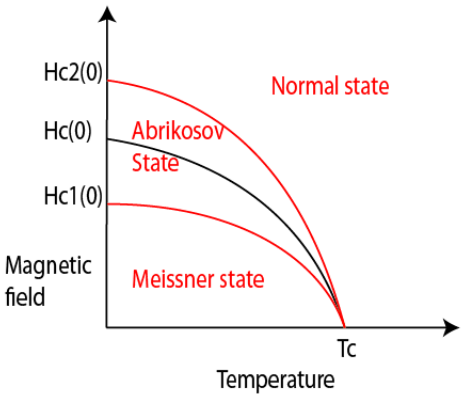

(b) Critical magnetic field of type-II superconductor.

Figure 1.6: Critical fields as functions of temperature for type-I and type-II superconductors.

In understanding why and how superconductors behave in such ways in external magnetic fields, it is very convenient to employ the phenomenological theory of superconductivity developed by Lev Landau and his student Ginzburg

in 1950s [7], which was built on top of Landau's theory of second-order phase transitions.

1.1.2 Overview of Ginzburg-Landau theory

The complete Ginzburg-Landau (GL) theory started in 1937 and was further developed by Landau's student Ginzburg in 1950 specifically for a theory of superconductivity [8]. Later when BCS theory came out [9], which was the first microscopic theory, another student of Landau's, Gor'kov, rigorously derived GL theory from BCS theory, showing that the former is a limiting case of the later [10].

The original theory of second order phase transitions promoted by Landau was based on three fundamental assumptions [11]:

- The system can be described by a complex scalar order parameter, that goes to zero at the transition point.
- The free energy of a system exhibits a second order phase transition, which is continuous. Thus the difference between the free energy (F) of the system before and after the transition, near the transition point, is infinitesimally small and can be expanded in a power series.
- The expansion coefficients of such an expansion are functions of temperature.

Consider a system that undergoes a second order phase transition. We can express the system's free energy density ($f = F/V$) as

$$f = f_n + \Delta f, \tag{1.1}$$

where f and f_n denote free energy density after the transition and that before transition (normal state). At the transition temperature, Δf is exceedingly small, thus we can expand it into a series:

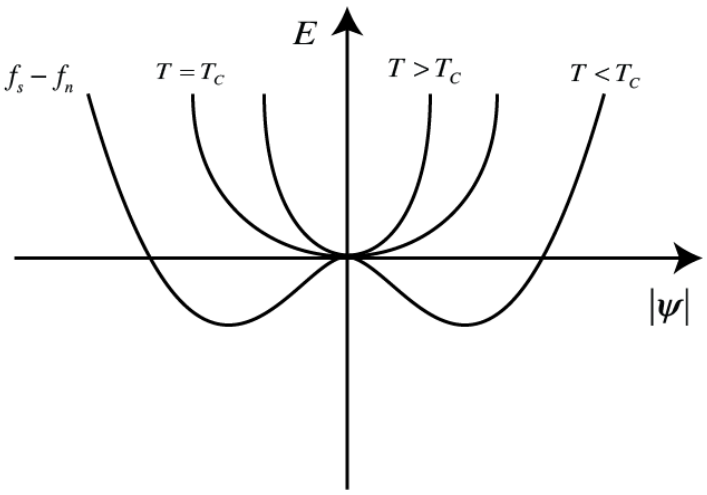

Figure 1.7: Typical diagram of the free energy density of a system as it undergoes a second order phase transition. As temperature goes across and below the transition temperature (T_c), the corresponding free energy curve changes smoothly, shifting the energy minima.

$$f = f_n + \alpha(T)|\psi|^2 + \frac{\beta(T)}{2}|\psi|^4 + ... \tag{1.2}$$

In the equation above, both $\alpha(T)$ and $\beta(T)$ are expansion coefficients that are functions of temperature, and ψ is the order parameter, which, later turned out to be just the macroscopic wavefunction of condensates. Here we abandoned higher order terms as they contribute little to the overall free energy, and only keep terms to the power of an even number because of symmetry considerations.

Now we add the kinetic energy term:

$$f = f_n + \frac{\hbar^2}{2m^*}|\nabla\psi|^2 + \alpha(T)|\psi|^2 + \frac{\beta(T)}{2}|\psi|^4 + ... \tag{1.3}$$

Where $m*$ is effective mass of a Cooper pair of electrons. Mathematically, it is convenient to push the temperature dependence of expansion coefficients solely onto $\alpha(T)$, making $\beta(T) =$ constant. Noting that the free energy is a function of wavefunction, the minimization of free energy using variation principle is then conducted with respect to the wavefunction:

$$\frac{\partial f}{\partial \psi(r)} = 0, \qquad \frac{\partial f}{\partial \psi^*(r)} = 0. \tag{1.4}$$

If the system is immersed in a magnetic field, we will have to do the following transformation:

$$-i\hbar\nabla \rightarrow -i\hbar\nabla - q\vec{A}, \tag{1.5}$$

where q is effective charge, and $\vec{A}$ is the vector potential that is related to the external magnetic field by $\vec{B} = \nabla \times \vec{A}$. For superconductors, $q = -2e$, and $\vec{A}$, of course, depends on the applied field and gauge choice. Then the free energy density would appear as:

$$f = f_n + \alpha|\Psi|^2 + \frac{\beta}{2}|\Psi|^4 + \frac{1}{2m^*}\left|(-i\hbar\nabla - \frac{e^*}{c}\vec{A})\Psi\right|^2 + \frac{h^2}{8\pi}. \tag{1.6}$$

Through algebra manipulation, this eventually leads us to a nonlinear Schrödinger equation:

$$\alpha\Psi + \beta\Psi|\Psi|^2 + \frac{1}{2m^*}\left(i\hbar\nabla + \frac{e^*}{c}\vec{A}\right)^2\Psi = 0, \tag{1.7}$$

and its boundary condition:

$$\left(i\hbar\nabla\Psi + \frac{e^*}{c}\vec{A}\Psi\right)\cdot\vec{n} = 0. \tag{1.8}$$

This is the first Ginzburg-Landau (GL) equation for a superconductor in a magnetic field. Sometimes in a large system, where variables vary slowly and smoothly, a linearized form of this Ginzburg-Landau equation is also used to solve problems, in which we simply drop the third order term from eqn.1.8.
In the first GL equation, the expansion coefficients are given by:

$$\begin{aligned} \alpha &\approx 1 - \frac{T_c}{T}, \\ \beta &\approx \text{Const.} \end{aligned} \tag{1.9}$$

The second Ginzburg-Landau equation is a consequence of the additional parameter: magnetic field ($\vec{B}$) now, which in equivalent determined by $\vec{A}$, therefore, we perform variation principle again with respect to vector potential:

$$\frac{\partial f}{\partial \vec{A}} = 0. \tag{1.10}$$

This will lead us to the second Ginzburg-Landau equation through algebraic

manipulation, during which we use the identity: $\vec{a} \cdot \nabla \times \vec{b} = \vec{b} \cdot \nabla \vec{a} - \nabla(\vec{a} \cdot \vec{b})$ [4], to arrive at

$$\begin{aligned} \vec{j_s} &= \frac{c}{4\pi} \nabla \times \nabla \times \vec{A} = -\frac{i\hbar e^*}{2m^*}(\Psi^* \nabla \Psi - \Psi \nabla \Psi^*) - \frac{e^*}{m^* c}|\Psi|^2 \vec{A} \\ &\Rightarrow \nabla(\nabla \cdot \vec{A}) - \nabla^2 \vec{A} = -\frac{i\hbar e^*}{2m^*}(\Psi^* \nabla \Psi - \Psi \nabla \Psi^*) - \frac{e^*}{m^* c}|\Psi|^2 \vec{A}. \end{aligned} \tag{1.11}$$

This is the second Ginzburg-Landau equation. Together with the previous one we have the whole set of GL equations:

$$\begin{cases} \alpha \Psi + \beta \Psi |\Psi|^2 + \frac{1}{2m^*} \left(i\hbar \nabla + \frac{e^*}{c} \vec{A} \right)^2 \Psi = 0 \\ \vec{j_s} = -\frac{i\hbar e^*}{2m^*}(\Psi^* \nabla \Psi - \Psi \nabla \Psi^*) - \frac{e^*}{m^* c}|\Psi|^2 \vec{A}. \end{cases} \tag{1.12}$$

Since the only unknown variables are Ψ (order parameter/wavefunction) and $\vec{A}$(magnetic field), these two coupled equations should be adequate to solve for solutions to any system that can be described by this theory.

Some important conclusions from Ginzburg-Landau theory

Two excellent predictions from GL theory concern the coherence length and the penetration depth, derivations of which can be found in numerous textbooks and reviews. Presented here is a brief summary from ref. [2, 11, 4].

Consider the surface of a superconductor along the yz-plane so that the x-axis is perpendicular to the surface of the superconductor. The order parameter (wavefunction) would apparently be zero outside of the superconductor, while far inside of it (granted that the size of superconductor is large enough to be considered infinitely large) the normalized order parameter would be unity. Based on our experience with physics, there should be a smooth transition, instead of an abrupt change, between these two values of order parameter near the surface. But how thick is this transition area? It turns out that the Ginzburg-Landau theory can adequately give insight to this question. The GL function in this case is reduced to one dimension, and we can at the same time

manipulate coefficients to simplify our equations:

$$\alpha\Psi + \beta\Psi^3 - \frac{\hbar^2}{4m}\nabla^2\Psi = 0 \Rightarrow \Psi + \frac{\beta}{\alpha}\Psi^3 - \frac{\hbar^2}{4m\alpha}\frac{d^2\Psi}{dx^2} = 0. \tag{1.13}$$

Now if we substitute in a dimensionless wavefunction $\psi = \frac{\Psi}{\sqrt{|\alpha|/\beta}}$, and a parameter $\xi = \frac{\hbar^2}{4m|\alpha|}$, then we have a simpler first GL equation:

$$-\xi^2\frac{d^2\psi}{dx^2} - \psi + \psi^3 = 0. \tag{1.14}$$

Now define $f(x) = \begin{cases} 1 & x = 0 \\ 0 & x = \infty \end{cases}$ as a function to describe the reduction of the order parameter along the x direction ($\psi(x) = 1 - f(x)$). This makes the order parameter vanish at the surface of the superconductor. Plug this definition into eqn. 1.8, we end up having:

$$-\xi^2\frac{d^2\psi}{dx^2} + 2f(x) = 0. \tag{1.15}$$

This gives a solution that satisfies our requirement for the magnitude of the order parameter at the boundaries: $f(x) = f_0 e^{-\frac{\sqrt{2}x}{\xi}}$, and thus $\psi(x) = 1 - f_0 e^{-\frac{\sqrt{2}x}{\xi}}$. From this solution, it follows immediately that the quantity ξ dictates the spatial decay of order parameter. This parameter is called the "coherence length," and is the first important conclusion from GL theory. In the current case, it characterizes the thickness over which the order parameter recovers to unity from zero at the surface of the material.

From the definition of the coherence length, $\xi^2 = \frac{\hbar^2}{4m\alpha}$, we notice that it is temperature dependent as the α is temperature dependent by definition. Then it comes naturally that it diverges at T_c as α vanishes at this temperature, and near T_c, $\xi \propto (T_c - T)^{-1/2}$ or equivalently $\xi^2 \propto (1 - t)^{-1}$ with $t = \frac{T}{T_c}$ as the reduced temperature.

Now we take a look at the second GL equation, which describes the coupling between supercurrents and an externally applied magnetic field. By plugging

in $\psi(x) = \psi_0 e^{i\phi(x)}$ to the second GL equation, we should have:

$$\mathbf{j} = \frac{2e\hbar}{m}\psi_0 \frac{d\phi(x)}{dx} - \frac{4e^2}{mc}\psi_0 \mathbf{A}. \tag{1.16}$$

If we take the curl of the expression for supercurrents, we get:

$$\vec{\nabla} \times \mathbf{j} = -\frac{4e^2}{mc}\psi_0 \vec{\nabla} \times \mathbf{A}. \tag{1.17}$$

By definition, $\vec{\nabla} \times \mathbf{A} = \mathbf{H}$, plus $\vec{\nabla} \times \mathbf{H} = \frac{4\pi}{c}$, thus we have:

$$\begin{aligned} &\frac{4e^2}{mc}\psi_0 \mathbf{H} + \frac{c}{4\pi}\vec{\nabla} \times \vec{\nabla} \times \mathbf{H} = 0 \\ \Rightarrow &\mathbf{H} + \lambda^2 \vec{\nabla} \times \vec{\nabla} \times \mathbf{H} = 0. \end{aligned} \tag{1.18}$$

Where $\lambda = \sqrt{\frac{mc^2}{16\pi^2\psi_0^2}}$, is the second important parameter from GL theory: the penetration depth. In addition to its applications to many other problems, this parameter here, as implied by its name, characterizes how deep a magnetic field can penetrate a superconducting sample (given that it's not too strong to destroy superconductivity).

Now before introducing the last parameter/conclusion from GL theory to be included here, we need to take a step back to look at the free energies again. As early as 1935, Friz London considered the free energy difference of a superconductor between when it is in a magnetic field and when it is not, from which consideration he derived the penetration depth long before Ginzburg and Landau did. The underlying logic is as follows.

In the absence of magnetic field, we denote the free energy of a superconductor as F_{s0}, and from now on, we adopt the following subscript notations: "s" as superconducting state, "n" as normal state, "0" indicates zero-field, and "h" implies the strength of the local magnetic field at a given point. Now if we immerse the sample in an external field, two additional terms will arise, one from the persistent current induced by the field, and one from the field itself.

The total free energy is given as:

$$\begin{aligned} F_{sH} = F_{s0} + F_{kin} + F_{mag} &= F_{s0} + \frac{1}{2}\int_V m_e^* n_s |v|^2 dr + \int_V \frac{\mathbf{h}^2}{8\pi} dr \\ &= F_{s0} + \frac{1}{8\pi}\int_V (\mathbf{h}^2 + \lambda^2 |\vec{\nabla} \times \mathbf{h}|^2) dr. \end{aligned} \tag{1.19}$$

Here except for all the parameters we have already encountered, m_e^* is the effective electron mass, n_s is the density of condensates (ψ), and v is their velocity. Now let's consider this free energy with a small twist. Imagine a type-I superconductor in a magnetic field. If the strength of the field is almost at the value that will destroy superconductivity, an infinitesimal increase of the field would suddenly "turn off" superconductivity for the sample, and allow the external field to enter. The free energy associated with superconductivity itself will have only an infinitesimal change ($F_{sH} \approx F_n$) as it is a second-order phase transition; that is, the supercurrent won't change abruptly, and thus the free energy associated with it also doesn't change. The only sudden change is the magnetization of the sample ($-\int_0^{H_{\rm cm}} \mathbf{M} d\mathbf{h} = \frac{H_{\rm cm}^2}{8\pi}$). Thus we have:

$$F_n - F_s = \frac{H_{\rm cm}^2}{8\pi}. \tag{1.20}$$

here $H_{\rm cm}$ is called thermodynamic critical field, since it is the field that separates the superconducting and normal states from the point view of thermodynamics. Recalling the Ginzburg-Landau expansion of free energy in terms of the order parameter near the transition temperature in the absence of a magnetic field: $F_{s0} = F_n + \alpha|\Psi|^2 + \frac{\beta}{2}|\Psi|^4 + ...$ To be physically sound, only the order parameter that minimized the system's overall free energy is considered realistic. Mathematically this is expressed as $\frac{\partial F_s}{\partial |\Psi|^2} = 0$, and the solution this gives is $\Psi_0^2 = -\frac{\alpha}{\beta}$, and therefore $F_n - F_s = \frac{\alpha^2}{2\beta}$.

Now if we combine these two expressions of free energy difference, we end up having $H_{\rm cm}^2 = \frac{4\pi\alpha^2}{\beta}$, and finally it is time to introduce the third important parameter/conclusion from GL theory: $\kappa = \frac{\lambda}{\xi}$. Plug in the definitions of λ and ξ, recombine terms to include $H_{\rm cm}$, then we have:

$$\kappa = 2\sqrt{2}\frac{e}{\hbar c}\lambda^2 H_{\rm cm} \tag{1.21}$$

What is worth noticing here is that this parameter is temperature independent, and thus an intrinsic property of each superconductor. Moreover, it is this parameter that characterizes superconductors as either type-I and type-II. For materials with $\kappa > \frac{1}{\sqrt{2}}$, it is a type-II superconductor as the surface energy is negative at this point and allows vortices to exist, while when κ is smaller than $\frac{1}{\sqrt{2}}$, it is a type-I superconductor ($H_{c2} < H_{\mathrm{cm}}$). In addition, many other conclusions derived from GL theory are related to this parameter as well as the thermodynamic critical field. For example, the lower and upper critical magnetic fields of type-II superconductors are rigorously given, respectively, as

$$H_{c1} = \frac{\hbar c}{4e\lambda^2}(\ln\kappa + 0.08) \qquad\qquad H_{c2} = \sqrt{2}\kappa H_{\mathrm{cm}} \tag{1.22}$$

Given the temperature dependence of H_{cm} (roots from the temperature dependence of λ^2), the temperature dependence of the lower and upper critical fields of type-II superconductors can be sketched (near T_c)as:

$$H_{c1} \propto (T_c - T)^{-1}, \tag{1.23}$$

$$H_{c2} \propto (T_c - T)^{-1}. \tag{1.24}$$

In addition to the example above, there are still numerous conclusions from GL theory that agree well with experimental results, however due to the focus as well as the limitation of length, the rest are omitted from this thesis.

Despite of the convenience and power that Ginzburg-Landau theory provides for understanding superconductivity, as a phenomenological theory, it doesn't get to the origin of the problem and thus fails to tell the whole story. Due to the nature of physics and inquisitiveness of physicists, a theory that unveils the very naked face of superconductivity is always in request. In 1957, almost a decade later than GL theory, the very first theory that touched the fundamental origin of superconductivity was born. It was the now well celebrated BCS theory, which was named after the initials of its inventors. Due to the importance of the BCS theory as the corner stone in the field of superconductivity, I almost feel obliged to include it in this dissertation, even just with a brief review.

1.1.3 Overview of the microscopic theory of superconductivity

In 1957, a theoretical paper titled "Microscopic theory of superconductivity" was published by J. Bardeen, L.N. Cooper and J.R. Schrieffer. Historically, this was the first theory about the microscopic origin of superconductivity. Soon after this paper, numerous experiments confirmed the validity of this theory, and it since then has become the most effective theory explaining the fundamental mechanism of superconductivity. Here I only attempt to give a brief overview of the theory with an emphasis on the part of the conclusion regarding our experiment.

Electron-electron interactions

An obvious and prominent interaction that exists among electrons (especially bare electrons) is the Coulomb interaction, which is given as

$$V_{e-e}^{\text{Coulomb}}(r_{e-e}) = \frac{e^2}{4\pi\epsilon_0|r_{e-e}|}, \tag{1.25}$$

where $\epsilon_0 = 8.85 \times 10^{-12} F/m$ is the absolute permittivity, and $|r_{e-e}|$ is the distance between two electrons. Because the charge carried by two electrons is always of the same sign (negative), this interaction always results in a repulsive (positive) force. Apart from this, electrons are also restricted by the Pauli exclusion principle, which states that, in our case, no more than one electron can occupy one quantum state. Thus two bare electrons always repel each other.

Now if the two electrons are not presented in vacuum (as being "bare") but instead are place in lattice of a (neutral) solid, things will then have a little twist. Despite the fact that both of the aforementioned interactions (Coulomb interaction and Pauli exclusion principle) are still in effect, the magnitude of the Coulomb interaction between two electrons, or more precisely, two quasiparticles is much weakened by the screening effect from the exchange-correlation holes that surrounds the electrons (dielectric medium). This reduced Coulomb

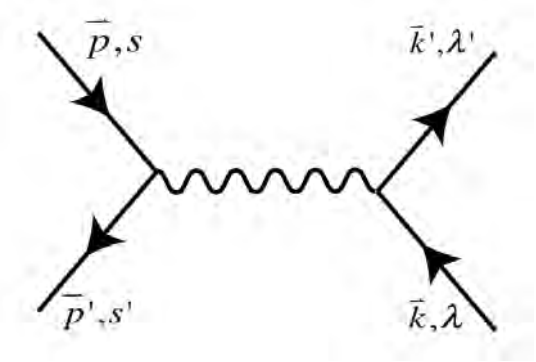

Figure 1.8: Feynman diagram of a first order electron-electron interaction via phonons.

interaction is given, using the Thomas Fermi model [2], as follows:

$$V_{\mathrm{TF}}(r_{e-e}) = \frac{e^2}{4\pi\epsilon_0 |r_{e-e}|} e^{-|r_{e-e}|/r_{\mathrm{TF}}}. \tag{1.26}$$

This potential will die out exponentially once the distance between the two electrons (r_{e-e}) exceeds the Thomas Fermi screening length (r_{TF}). The main effect of this "decoration" of the original Coulomb interaction is that it reduces the interaction to a short range one, which plays an important role in the emergence of superconductivity.

Apart form this reduced Coulomb repulsive interaction, two electrons in solids would also interact with each other via their interactions with phonons. To the first order, this process can be represented with a Feynman diagram (see figure 1.8). If we are going into the details a little bit more, we should then first define a lattice deformation potential [2] (since phonons essentially arise from the vibration or delocalization of atoms in a crystal lattice):

$$\delta V_l(r) = \sum_i \frac{\partial V_l(r)}{\partial R_i} \delta R_i, \tag{1.27}$$

where δR_i is the displacement of atom "i" in the crystal lattice, and can be expressed as in terms of angular frequency ($\omega_{\mathbf{q},\lambda}$), phonon creation and annihi-

lation operators ($a^+_{\mathbf{q},\lambda}, a_{\mathbf{q},\lambda}$), and the atom's mass ($M$):

$$\delta R_i = \sum_{\mathbf{q},\lambda} \hat{e}_{\mathbf{q}\lambda} \left(\frac{\hbar}{2M\omega_{\mathbf{q}\lambda}} \right)^{1/2} (a^+_{\mathbf{q}\lambda} + a_{-\mathbf{q}\lambda}) e^{i\mathbf{q}\cdot\mathbf{R_i}}. \tag{1.28}$$

This potential will be felt by the electrons travelling inside the crystal, and the essential consequence of this potential is a scattering process (electron-phonon interaction) during which an electron can be scattered by a phonon, and move from one quantum state to another under the restriction of conservation of crystal momentum. Another way of seeing this process is that an electron can emit or absorb a phonon and correspondingly change its momentum by the law of conservation of (crystal) momentum. Thus when this process involves two electrons for example (as seen in figure 1.8), one can describe, to first order, the electron-electron interaction via a phonon as a process where an electron emits a phonon of certain momentum, which propagates inside the crystal and then later is absorbed by another electron. In the end, it is as if momentum has been transferred between two electrons with a time delay via some medium. Mathematically, this interaction can be written as [2]:

$$V(\mathbf{q},\omega) = |g_{\mathbf{q},\lambda}|^2 \frac{\omega^2_{\mathbf{q},\lambda}}{\omega^2 - \omega^2_{\mathbf{q},\lambda}} \tag{1.29}$$

Here $\omega_{\mathbf{q},\lambda}$ is the frequency of a phonon with a wavevector of $\mathbf{q}$, and the coupling coefficient $g_{\mathbf{q},\lambda}$ is of the order of $\sqrt{\frac{m}{M}}$, where m is the mass effective mass of electrons near Fermi surface, and M is the mass of atoms in the lattice. The physical meaning of $g_{\mathbf{q},\lambda}$ is related to the scattering cross section of an electron between two states differing by momentum $\mathbf{q}$. If we plug in numbers, we will discover that the interaction between electrons and phonons is fairly weak, thus an approximation to the second order is sufficient in most of our analysis.

It is apparent from the equation of this potential that it is attractive when $\omega < \omega_{\mathbf{q},\lambda}$, and is repulsive when the other way around, and BCS ignored the repulsive part as it is unimportant to the problem under inspection here. In order to reduce the complexity of calculation, the threshold of this frequency ($\omega_{\mathbf{q},\lambda}$) was replaced with a constant (ω_D) that represents a frequency averaged over the entire range of wavevector ($\mathbf{q}$). In addition, the coupling coefficient is

also replaced with an effective constant to remove its dependence on wavevectors. Now, the potential then becomes:

$$V_{\text{eff}} = |g_{\text{eff}}|^2 \frac{\omega_D^2}{\omega^2 - \omega_D^2}. \tag{1.30}$$

the BCS theory further simplifies this equation to

$$V_{\text{eff}} = -|g_{\text{eff}}|^2, \quad |\omega| < \omega_D. \tag{1.31}$$

The argument here is that, at low temperature where superconductivity occurs, only electrons near the Fermi surface within a range of $\pm k_B T$ contributes to the conduction, and $\hbar\omega_D \gg k_B T$, so any thermal excited electrons near Fermi surface falls into the range of $E_f \pm \hbar\omega_D$, and are considered interacting with each other by this negative potential.

Therefore, an additional term in the total Hamiltonian appears as an effective electron-electron interaction, and is given in second-quantization language as:

$$\hat{H}_{e-e} = -|g_{\text{eff}}|^2 \sum_{\mathbf{k},\mathbf{p},\lambda,s} \hat{c}^+_{\mathbf{k}',\lambda'} \hat{c}^+_{\mathbf{p}',s'} \hat{c}_{\mathbf{k},\lambda} \hat{c}_{\mathbf{p},s}. \tag{1.32}$$

Single electron pair (Cooper problem)

In free space, no bound electron pairs would be found due to the strong Coulomb interaction [2], but BCS examined what would happen to two electrons in a Fermi sea, and the unexpected result is that, unlike in the free space, they would form a bound state no matter how weak the attractive interaction between them is. This idea eventually became the cornerstone of the microscopic theory of superconductivity.

Imagine a perfect Fermi sphere, with two extra electrons are placed near its surface as indicated in figure 1.9. The wavefunction of this pair of electrons can be written as [12]:

$$\psi(r_1, \lambda, r_2, -\lambda) = e^{i\mathbf{k}_{\text{cm}} \cdot \mathbf{R}_{\text{cm}}} \phi(r_1 - r_2) \phi_{\lambda,-\lambda}, \tag{1.33}$$

where "cm" indicates "centre of mass," thus $R_{\text{cm}} = (r_1 + r_2)/2$, and $\hbar k_{\text{cm}} = 0$.

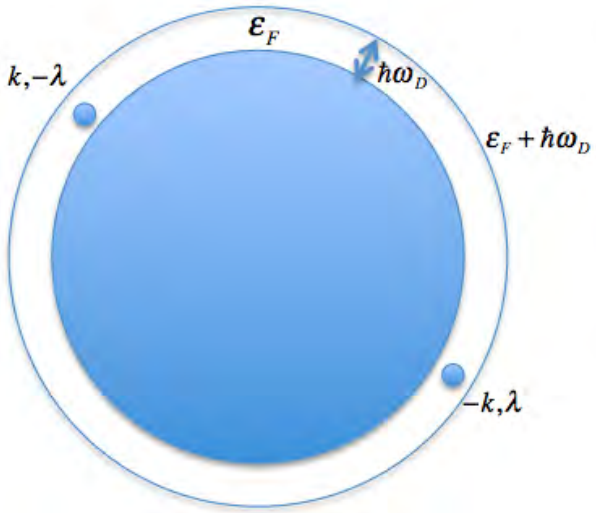

Figure 1.9: A scheme to demonstrate a pair of electrons of opposite wavevectors and polarizations near the surface of a perfectly filled Fermi sphere.

The spatial part of this function can be expanded in terms of Bloch wavefunctions since it is in a periodic structure:

$$\phi(r_1 - r_2) = \sum_{\mathbf{k}} \phi_{\mathbf{k}} e^{i\mathbf{k}\cdot(\mathbf{r_1}-\mathbf{r_2})}. \tag{1.34}$$

For a bound state of two electrons, it can be either a singlet state or a triplet one. A singlet state $[\phi_{\lambda,-\lambda} = \frac{1}{\sqrt{2}}(|\uparrow\downarrow\rangle - |\downarrow\uparrow\rangle)]$, which is an odd function of spin polarization, is used here (as indicated in figure 1.9) since it is both simpler and more common. If we plug this function into Schrödinger's equation, a self-consistent solution is [2, 12]:

$$1 = -|g_{\text{eff}}|^2 \sum_{\mathbf{k}} \frac{1}{E - 2\epsilon_{\mathbf{k}}}. \tag{1.35}$$

Summing (integrating) over all available $\mathbf{k}$ states (within the thin shell between ϵ_F and $\epsilon_F + \hbar\omega_D$) eventually provides an approximate solution in the weak coupling limit ($N(\epsilon_F)|g_{\text{eff}}|^2 << 1$) to the eigenvalue for the Schrödinger equation [2]:

$$E = -2\hbar\omega_D e^{-\frac{2}{|g_{\text{eff}}|^2 N(\epsilon_f)}}, \tag{1.36}$$

where $N(\epsilon_f)$ is the density of states at Fermi surface, and is used here to replace the actual density of states, $N(\epsilon_k)$, for it is a slowly varying function of energy

within the thin shell of $\epsilon_F \pm \hbar\omega_D$. An approximate solution in the strong limit ($N(\epsilon_F)|g_{\text{eff}}|^2 >> 1$) can also be derived [12],

$$E \sim -\hbar\omega_D |g_{\text{eff}}|^2 N(\epsilon_F). \tag{1.37}$$

Here is where we see how critical a filled Fermi sea is in this theory, which provided, no matter how small, a non-vanishing density of states $N(\epsilon_F)$ at the surface of Fermi sphere, without which, no bound state would exist.

Macroscopic wavefunction

From the Cooper problem, it is already demonstrated that two electrons near the Fermi surface can form a bound state. Thus the next is to prove that all electrons at the Fermi surface will bind into pairs. In order to do so, a trial many-body wavefunction ($|\Psi_{\text{BCS}}\rangle$) is constructed using "pair creation and annihilation operators," which are defined in terms of electron creation and annihilation operators as: $\hat{P}^+_{\mathbf{k}} = \hat{c}^+_{\mathbf{k},\lambda}\hat{c}^+_{-\mathbf{k},-\lambda}, \hat{P}_k = \hat{c}_{\mathbf{k},\lambda}\hat{c}_{-\mathbf{k},-\lambda}$. The many-body wavefunction is written as [2]:

$$|\Psi_{\text{BCS}}\rangle = \text{Const.} \cdot e^{\sum_{\mathbf{k}} \alpha_{\mathbf{k}} \hat{P}^+_{\mathbf{k}}} |0\rangle, \tag{1.38}$$

and $\alpha_{\mathbf{k}}$ is a coefficient determined through minimization of energy. This function can be further written in a Hartree-like function by using the commutation rules of pair creation and annihilation operators and with the assumption that the total number of quasiparticles are conserved. The process is omitted here, but the result is given below [9]:

$$|\Psi_{\text{BCS}}\rangle = \prod_{\mathbf{k}} \left(u^*_{\mathbf{k}} + v^*_{\mathbf{k}} \hat{P}^+_{\mathbf{k}}\right) |0\rangle, \tag{1.39}$$

where $u^*_{\mathbf{k}} = \frac{1}{1+|\alpha_{\mathbf{k}}|^2}$ and $v^*_{\mathbf{k}} = \frac{\alpha_{\mathbf{k}}}{1+|\alpha_{\mathbf{k}}|^2}$. Therefore the entire eigenstate now only depends on $\alpha_{\mathbf{k}}$, which is determined by minimization of total energy. It is only natural now to find a solutions to the minimized total energy. With the Hamiltonian ($\hat{H} = \hat{H}_0 + \hat{H}_{e-e}$), one will find by plugging the trial wavefunction

in $E = \langle \Psi_{\rm BCS}|\hat{H}|\Psi_{\rm BCS}\rangle$ that [2]:

$$E = 2\sum_{\mathbf{k}} \epsilon_{\mathbf{k}} |v_{\mathbf{k}}|^2 - |g_{\rm eff}|^2 \sum_{\mathbf{k},\mathbf{p}} v_{\mathbf{k}} v_{\mathbf{p}}^* u_{\mathbf{p}} u_{\mathbf{k}}^*. \tag{1.40}$$

Here the total number of quasiparticles is still assumed to be conserved and can be shown to be $N_e = 2\sum_{\mathbf{k}} |v_{\mathbf{k}}|^2$, and the wavefunction is normalized. the next is to apply the variational principle to minimize the total energy with respect to both $v_{\mathbf{k}}$ and $u_{\mathbf{k}}$, and the final results are [2, 5, 9]:

$$|v_{\mathbf{k}}|^2 = \frac{1}{2}\left(1 - \frac{\epsilon_{\mathbf{k}} - \mu}{E_{\mathbf{k}}}\right)$$
$$|u_{\mathbf{k}}|^2 = \frac{1}{2}\left(1 + \frac{\epsilon_{\mathbf{k}} - \mu}{E_{\mathbf{k}}}\right).$$

Here μ was introduced as the Lagrange multiplier during the steps omitted and is essentially the chemical potential. In addition, an important parameter (Δ) was defined and included in $E_{\mathbf{k}} = \sqrt{(\epsilon_{\mathbf{k}} - \mu)^2 + |\Delta|^2}$. It is the famous BCS energy gap at zero temperature, given as

$$\Delta = |g_{\rm eff}|^2 \sum_{\mathbf{k}} u_{\mathbf{k}} v_{\mathbf{k}}^*. \tag{1.41}$$

Or if we substitute in the expression for $u_{\mathbf{k}}$ and $v_{\mathbf{k}}^*$, eventually we will have [2]:

$$1 = \frac{|g_{\rm eff}|^2}{2} \sum_{\mathbf{k}} \frac{1}{\sqrt{(\epsilon_{\mathbf{k}} - \mu)^2 + |\Delta|^2}}, \tag{1.42}$$

which give the gap equation, in explicit form, at zero temperature as:

$$\Delta = \frac{\hbar\omega_D}{\sinh[1/|g_{\rm eff}|^2 N(\epsilon_F)]}, \tag{1.43}$$

and in the weak coupling limit, this becomes:

$$\Delta \sim 2\hbar\omega_D e^{\frac{1}{|g_{\rm eff}|^2 N(\epsilon_F)}}. \tag{1.44}$$

The idea of BCS energy gap is also the main idea of the whole BCS theory, and we shall see below its physical significance. If one takes few more approximations and careful derivation, the following gap equation at finite temperature

should be obtained, just as BCS originally did [9],

$$\Delta = |g_{\text{eff}}|^2 \sum_{\mathbf{k}} \frac{\Delta}{2E_{\mathbf{k}}} \tanh\left(\frac{E_{\mathbf{k}}}{2k_B T}\right). \tag{1.45}$$

This equation, when $\Delta \to 0$, gives the transition temperature of superconductivity (T_C): $k_B T_C = 1.13\hbar\omega_D e^{-\frac{1}{|g_{\text{eff}}|^2 N(\epsilon_F)}}$. Another famous result was the energy gap at zero temperature given as $2\Delta(0) = 3.52 k_B T_C$, and this is the minimum energy cost it takes to excite a single quasiparticle, or in other words, to break a pair of electrons [12].

A further derivation, which can be found in numerous textbooks [2, 4, 12, 5] and is not going to be presented here, will lead us to the ground state energy and the energy difference between superconducting state and normal state, the results are given here to conclude this section and save it for further discussions in latter chapters [4]:

$$E_s - E_n = -\frac{1}{2} N(\epsilon_F) \Delta^2(0). \tag{1.46}$$

1.2 Granular superconductors

A chronological review

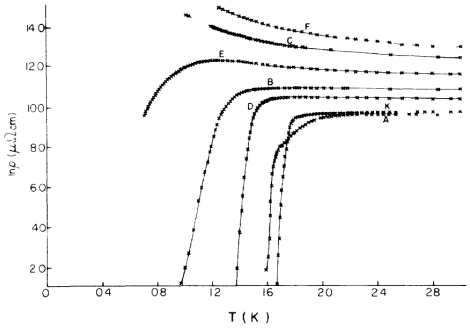

(a) Zero-field resistivity measurements of Al-Ge films in ref. [13].

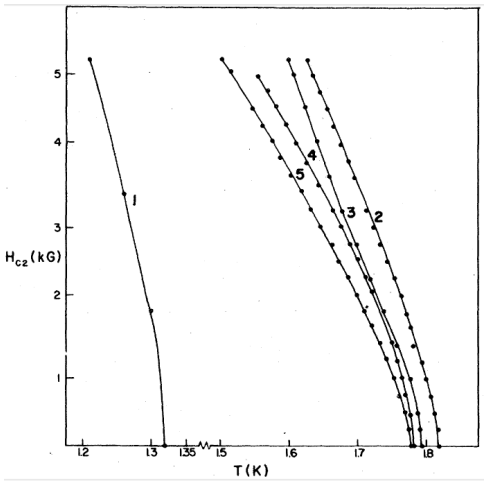

(b) Upper critical field measurement of Al-Ge films in ref. [14].

Figure 1.10: Enhancement of superconductivity in Al-Ge films observed by Shapira *et al.* in 1980s. Figures were taken from the original publications with permission.

In 1980 and 1983, Y. Shapira and G. Deutscher published two papers [13, 14], respectively, reporting observations of enhancements of superconducting transition temperatures in a compound superconducting system of aluminum and germanium. In these two papers, this system's superconducting transition temperature and upper critical fields' behaviour as functions of temperature were studied at different ratios of the two elements. This compound superconducting material, described as a granular superconductor, is essentially a simple mixture of a semiconductor element (Ge) and a metallic element (Al). A Transmission Electron Microscope (TEM) image of such a system is presented in figure 1.11), from which we can clearly see the grain boundaries between the two elements, and the mixture can be aptly summed up as pure aluminum grains embedded in germanium matrix since the two are immiscible to each other.

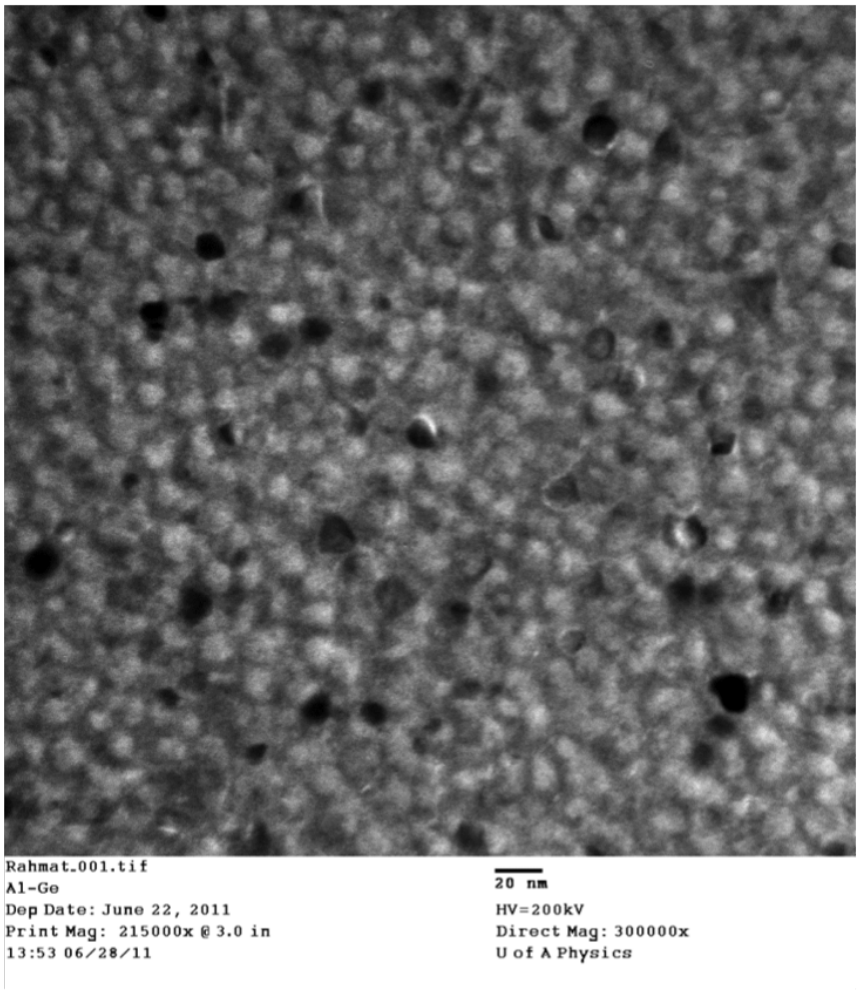

Figure 1.11: A Transmission Electron Microscope (TEM) image of an Al-Ge granular superconductor sample from our experiment. Image credit to our former summer student Rahmat Saeedi.

The surprising discovery of the enhanced superconducting transition temperature in this system arises from the fact that, one of the elements, germanium, as a semiconductor, has never been observed as a superconductor at any given temperature, while the other element, aluminum has been known since 1958 to have a superconducting transition temperature of 1.2 K [16]. Yet somehow, within a narrow range of volume ratios between the two, higher superconducting transition temperatures emerge in such a mixture, with the highest transition being observed to take place near 1.8 K (see figure 1.10(a)), which is 1.5 times higher than that of pure aluminum.

However, as a matter of fact, this wasn't the first time an enhancement

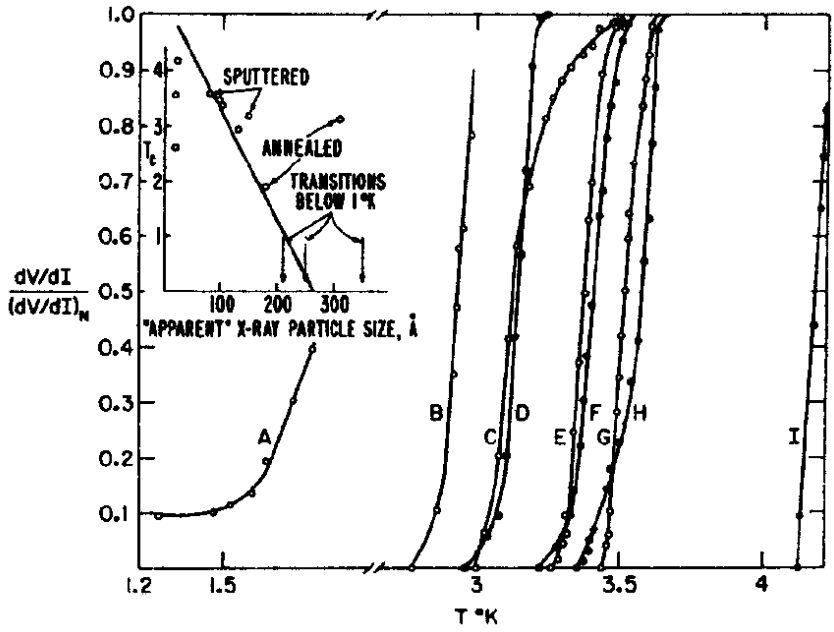

Figure 1.12: Zero-field resistivity measurement of tungsten films from ref. [15]. Figure taken with permission.

Metal	T_c (K)	T_c/T_{c0}
Al	3.0	2.6
Ga	7.2	6.5
Sn	4.1	1.1
In	3.7	1.1
Pb	7.2	1.0

Table 1.1: Table of superconductivity enhancement in metal films provided by B. Abeles *et al.* in ref. [17]. T_{c0} is the superconducting transition temperature of the corresponding pure bulk material, and T_c is that of the granular superconductors made from the corresponding material and its oxide.

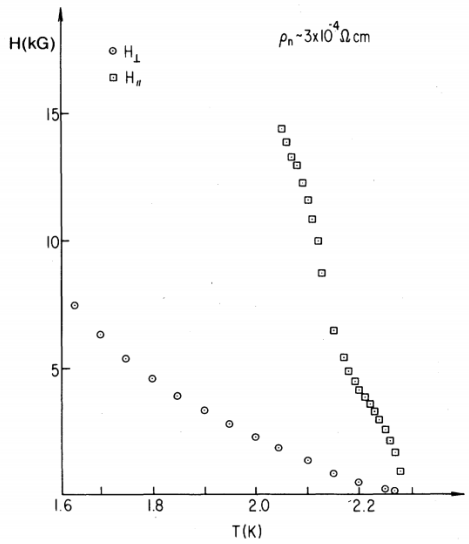

(a) The upturn in critical field curves (in plane and out of plane) of granular Al-Al_2O_3 films observed by G. Deutscher. Figure taken from ref. [18].

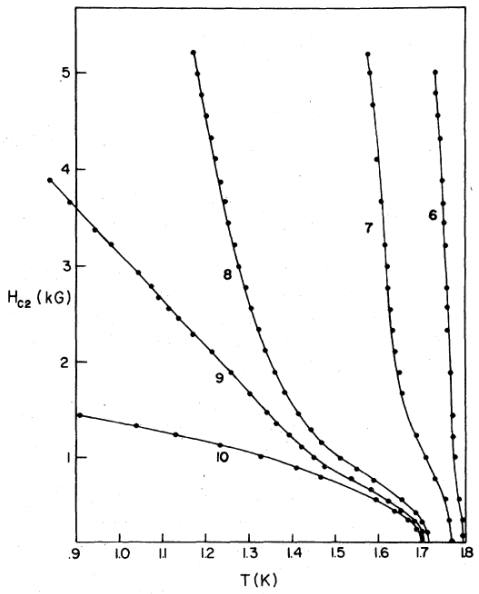

(b) The experimental data of upper critical fields as functions of temperature for high metal concentration (80 $\sim$ 88%) Al-Ge films. Figure taken from ref. [14].

of superconducting transition temperature being observed in experiments. In 1965, O.F. Kammerer and M. Strongin published a paper (ref. [15]), reporting an observation of enhancement of transition temperature of tungsten films from the bulk value < 0.01 K up to 4.1 K (see figure 1.12). A year later, B. Abeles, R.W. Cohen and G.W. Gullen from Princeton published a brief summary [17] of such granular superconductor systems (see table 1.1).

Not only did this enhancement in the transition temperature puzzle physicists, the reported observations of the upper critical field of such systems were also perplexing as they all appreciably differed from the generic look of upper critical field curve (see figure 1.6(b)) as described in chapter 1. As early as late 1977, G. Deutscher reported in ref. [18] observations of "upturns" in the upper critical field curves as functions of temperature in Al-Al_2O_3 granular superconducting films (see figure 1.13(a)), which was a system believed to be similar to the Al-Ge granular system in ref. [14].

What came with all the interesting phenomena in experiments was one sole question of why as all these observations seemed to contradict the empirical

understanding superconductivity at the time. Naturally people sought solutions first in existing models and theories. As early as 1964, Ginzburg already suggested in a short paper [19] that, in the presence of a dielectric material on the surface of a superconductor, due to the mutual attraction between electrons in the superconductor and neutral atoms in the dielectric material, an additional attraction between electrons will arise and thus give possible enhancement of the transition temperature. This is somewhat similar to the idea of $H_{c3} \sim 1.66 H_{c2}$ brought up by Saint-James and de-Gennes [20] a year prior, which in the end is a surface effect being magnified in such a system because of its large surface to volume ratio. This idea of Ginzburg's was somewhat reinforced in Kammerer and Strongin's 1965 paper [15], as the authors postulated with evidence that the oxide-metal interfaces may have contributed to the enhancement of the superconducting transition temperature. However, the authors also added on another possibility that this enhancement may arise from disorder and size effects without going into details of the mechanism. Then in Abeles, *et al.* 's 1966 paper [17], the authors discussed this size effect. They admitted that the enhancement of the superconducting transition temperature seemed to be related to the size of the metal grains in many samples as the smaller the grains, the stronger the electron-phonon interaction at the metal-insulator interfaces. But at the same time, they also realized that it failed to apply to all the superconducting metals. In the end, the authors concluded that there must be more, if not completely different, factors caused the enhancement in granular superconductors. Furthermore, in a later publication of Abeles *et al.* 's [21], they completely ruled out size effect on granular superconductivity due to strong couplings among superconducting grains. However, R.H. Parmenter from the same lab (RCA laboratories, Princeton) of Abeles' disagreed with him explicitly in his publication in 1968 [22], in which, he discussed in detail how size effects could lead to an enhancement of superconductivity, and concluded that, specifically for aluminum, when the metal grain volume becomes comparable to ~ 240 nm^3, the size effect is the strongest. Apparently, opinions over the cause of enhancement of the superconducting transition temperature in granular superconductors varied, and hardly anyone appeared to have evidence that is compelling enough to convince others.

In addition to the need to explain the enhancement of superconductiv-

ity in granular systems, the upturn in upper critical field observed also needs clarification. One year later after Deutscher's 1977 paper, he co-authored with O. Entin-Wohlman another paper [23], documenting similar "upturns" in critical field curves of layered superconductors, and with consideration of the anisotropy of the system, he attempted in this paper to attribute such an "upturn" to the competition between coupling strength among layers of superconductors in terms of the strength of external field. Furthermore, he compared this "upturn" to that observed in granular systems, proposing that it could be the coupling among grains of superconductors in the later system that led to this phenomenon. However, as sound as it appeared, Deutscher, in this paper, failed to deliver a quantitative comparison or fitting to the experimental data. Finally, in 1980, a paper Deutscher first authored with O. Entin-Wohlman and Y. Shapira [14], not only did they show experimental measurements of upper critical fields of Al-Ge granular systems with "upturns" in them (see figure 1.13(b)), they also claimed that they were able to fit the experimental data fairly well for samples of high metal concentrations. Yet, for those of low metal concentrations, the question seemed to persist. Of course, by far, there is still no effective theory at could pinpoint the origin of enhancement of transition temperature. Therefore, in order to help elucidate these effects, we reproduced some of the results of the enhancement of the transition temperature as well as the "upturns" in the upper critical field curves in Al-Ge granular films as our first step in tackling this intriguing problem of superconductivity.

Chapter 2

Experimental Methods

It goes without saying that, for experimental physicists, hands-on work on a lab bench is as, if not more, important as theoretical studies in front of a desk. Therefore, as an experimental physicist, I will dedicate this whole chapter to the experimental methods employed in my research.

2.1 Deposition

2.1.1 Deposition chamber

(c) A photo of the vacuum chamber used for both e-gun and thermal depositions.

(d) The control panel for the e-gun deposition system.

Figure 2.1: E-gun deposition system

For any experiment to work, the very first thing that needs to be done is to have a sample to study, and so is this how I will begin this chapter: by documenting the process of sample fabrication in our experiments.

All of our superconducting films were made through either electron or thermal deposition, or both, inside a chamber (see figure 2.1(c)) under vacuum condition ($\sim 10^{-6}$ Torr). The whole deposition system roughly comprises two separate parts: the bell jar and the base unit.

The base unit of the system accommodates an e-gun deposition system (see figure 2.5), three feedthroughs for the circuits used in thermal deposition (see figure 2.8(c)), a gas inlet (see figure 2.5(d)) in case gaseous background is needed, a feedthrough for substrate cooling (water or liquid nitrogen), and a

frame holding up a thermocouple for temperature sensing, a substrate shutter to block the substrate off sources, and a heater for the substrate when needed.

The other part of the vacuum chamber: bell jar is made from aluminium and stainless steel, has two observation windows installed on its wall (see figure 2.1(c)), one of them is directed to the substrate that is located near the roof of the bell jar, the other one has a movable shutter, and is for view of the entire chamber (see figure 2.3(a)). At the very top of the bell jar, a stabbing heater is installed and used for both heating and illuminating purposes. The bell jar and base unit are sealed together with a half-inch thick and one-inch wide rubber o-ring, and by the bell jar's own weight. As can be seen in figure 2.3(b), a lifting system is installed behind the vacuum chamber that is capable of lifting the bell jar with a motor when needed, for example, changing targets/substrate, maintenance *etc.* A simplified scheme of the whole deposition system can be found in figure 2.2.

It goes without saying that a pump is necessary in order to create a vacuum environment inside the chamber. For the system we used, a cryo-pump by CTI Cryogenic®that operates at ~ 11.5 K was used to pump the chamber to its operating pressure. The pressure was constantly monitored by a Kurt J. Lesker 4500 ion gauge installed on the top shelf of an electronic rack, on which all system control related apparatus are installed (see figure 2.1(d)).

2.1.2 E-vap 4000 e-gun deposition

Now after a crude introduction to the deposition system, we can move on to the actual process of making samples with this system, and we shall start with the electron gun deposition system.

The very first step is to place evaporant material in place, which is in a crucible liner, water cooled and held by the copper hearth of the e-gun system in the centre, at the bottom, of the vacuum chamber (see figure 2.5(c)). The e-gun system used in the current experiment was the e-vap®4000, which has six of such pockets crucibles, and each pocket can hold one liner with evaporant

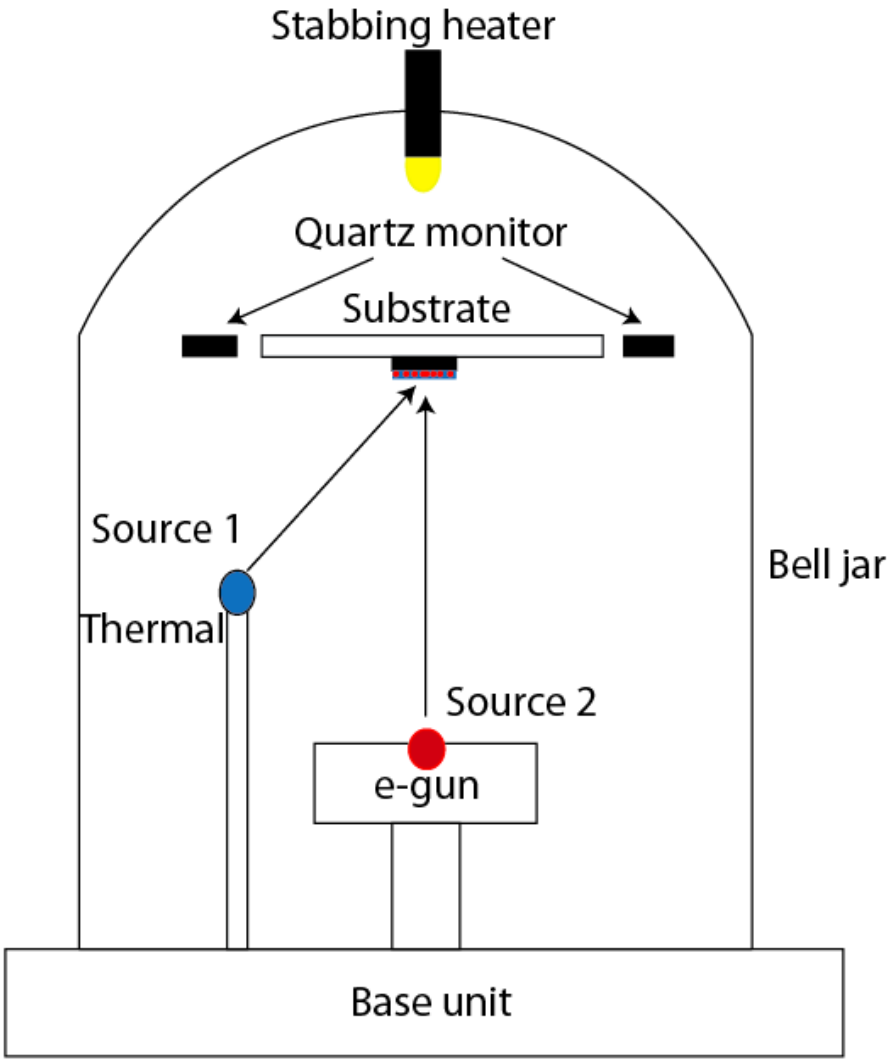

Figure 2.2: A schematic drawing of the thermal/electron-gun deposition system used in our experiments.

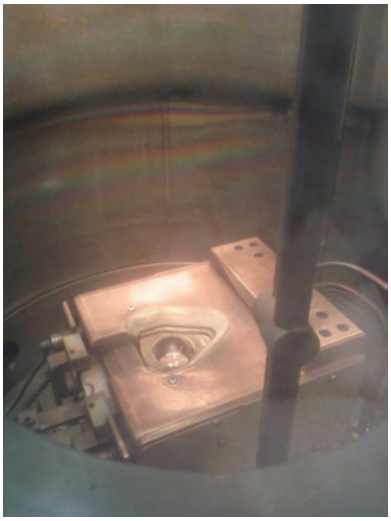

(a) One of the observation window on the wall of bell jar, the light comes from the stabbing heater on the top of the bell jar.

(b) The lifting system for the bell jar.

Figure 2.3: The bell jar and its lifting system.

Figure 2.4: The CTI cryo pump used to pump on the vacuum chamber used in depositions.

material in it. This allows the operator to switch from one material to another without venting and opening up the vacuum chamber by simply rotating the pockets with a handle outside of the chamber.

The way that the e-vap 4000 electron-gun deposition system evaporates the target materials is by using a filament at a negative electrical potential (~ -7 kV in the current experiment) to emit electrons in all directions. Then, with a beam former and deflection plate that works together with a cathode, a beam of electrons in a defined direction that points away from the e-gun is selected, and accelerated by a steep potential gradient. This highly energetic electron beam is deflected by 270 degrees using a transverse permanent magnetic field and hits the surface of evaporant material in the crucible liner. Upon its impact onto the evaporant material, the electrons transform their kinetic energy into thermal energy, which melts the surface layer of material. This process allows a consistent vapour emitting area, as it forbids subsurface boiling of the material. Using the current control of the system (installed on the system's control panel, see figure 2.1(d)), one can essentially adjust the number of electrons in the beam impinging on the surface of the material per unit time, and control the evaporating rate of the material.

An optional continuous sweeping movement of the electron beam's impact point over the source material can help control the evaporation rate, as well as ensure a uniform evaporation area in many cases. Such a sweep is achieved by applying a time varying magnetic field through an electro-magnetic coil to bend the electron beam's trajectory. The sweeping patterns are pre-programmed and stored in the e-cap®programmable sweep controller (model EV-XYS2-CE), which is also installed on the control panel.

(a) The two electrodes of the e-gun.

(b) The pressure gauge for the cooling water of e-gun/thermal deposition system.

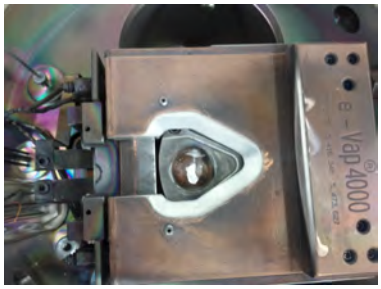

(c) Water cooled target holder (hearth).

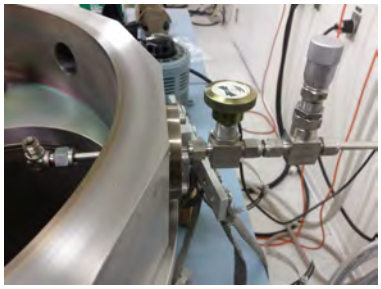

(d) Gas inlet for creating a gaseous background.

Figure 2.5: Electron gun deposition system.

Figure 2.6: The control for the current used in thermal deposition.

2.1.3 Thermal deposition

Since the granular superconducting films required for our experiments are comprised of two elements in each of them, and the e-gun deposition system is only capable of depositing one material at a time, we also had to simultaneously employ a thermal deposition system that was installed inside the same vacuum chamber. This allows us to co-evaporate the two elements onto the one substrate each time we make a sample (see figure 2.2). The thermal deposition system uses a source boat, in which lies the evaporant material, as part of a closed electrical circuit. When an AC current runs through this circuit, it will generate ohmic heating locally at the boat, and melt the material inside (see figure 2.8(a)). It was pointed out by Prof. J. Beamish that because of the position of the thermal deposition source is not directly under the substrate but rather on the side below it, a concentration variation was introduced into the final product. A detailed estimate of this variation related to the location of the thermal source is provided in appendix A.3, while here we only quote the result that the concentration variation of the germanium in the final product is of 2.6%, and this may partly contribute to the inhomogeneity in some samples.

The current circuit starts from one of the two electrodes outside the vacuum

chamber (see figure 2.8(d)), goes through the feedthrough into the chamber, runs up along one of the two posts that holds the copper clamps, then through the source boat that is tightly clamped between the two copper bridges (see figure 2.8(a)), and eventually comes back down on the other end. The current applied is controlled outside of the vacuum chamber, and there are four current ranges available to choose from, as in figure 2.6. The amplitude of the current can be monitored by a digital current clamp on one of the two external electrodes.

In practice, based on different needs, there is a large variety of materials from which the source boat can be made. Different boats have different tolerances for maximum current amplitudes. Overloading the current can cause a boat to melt or be permanently damaged. In our experiment, all the boats were made from tungsten and coated with Al_2O_3 for germanium deposition. The maximum current they can tolerate is 209 A. The most frequently used three models of boats were: S35-AO-W, S21-AO-W, and S9b-AO-W.

(a) The quartz crystal monitor installed at the same level of the substrate holder to monitor e-gun deposition.

(b) The stainless steel tube used to guide the vapour to the quartz monitor for thermal deposition system.

Figure 2.7: The two quartzes used to monitor e-gun and thermal deposition respectively.

What else is worth noticing is that the cooling water for this system only cools the feedthrough instead of the entire circuit, yet a failure of the cooling water may cause catastrophic result of melting down parts of the feedthrough assemblies. This would lead to a gross leak to the vacuum chamber. In additional, the current control runs in different ranges, as shown in figure 2.6. A current out of the range will blow the fuse and cut the circuit abruptly, which, more often than not, induces a thermal shock, and results in severe damages to the source boat in use.

Apart from the complete circuit for thermal deposition, certain accessaries have to be installed when conducting a co-evaporation with the thermal deposition and e-gun. They all serve the purpose of avoiding interference between the two depositions. The first additional part is a stainless steel tube, whose diameter is roughly the same as that of the quartz for monitoring thermal deposition. It must be installed onto the post which also hosts the substrate holder and its shutter (see figure 2.7(b)). The upper brim of the tube has to be adjusted so that it closely fit the quartz monitor (see figure 2.8(b)). The tube also have to be at a specific angle that, on the one hand, it guarantees a clear view of the quartz to the source boat, while, on the other hand, it should completely block the quartz from the e-gun source. The second item is a shutter that is to be installed at the back of the substrate holder for the other quartz (see figure 2.7(a)), which, again, blocks the unwanted source from being seen by the monitor.

(a) Target (germanium in figure) in a boat (S35-AO-W) clamped on posts inside the vacuum chamber for thermal deposition.

(b) Guide tube to the quartz crystal monitor used to monitor thermal deposition.

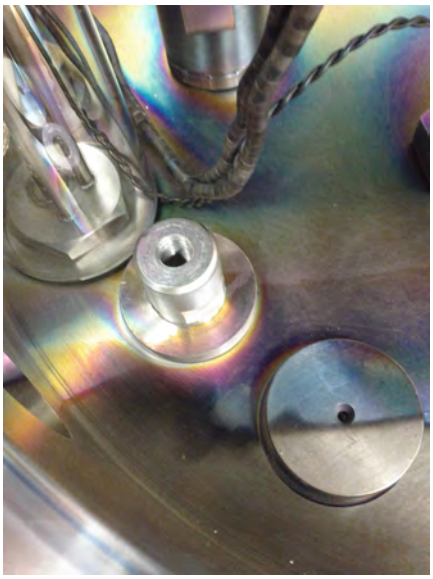

(c) The feedthrough at the bottom of the vacuum chamber for the thermal boat hosts.

(d) The two electrodes outside the vacuum chamber for thermal deposition.

Figure 2.8: Photos of the thermal deposition system used in the current experiment.

2.2 Cryogenic system

2.2.1 ^{4}He dipper fridge

(a) Front view of the dewar of the ^{4}He dipper fridge.

(b) ^{4}He condenser located on top of the dewar of the ^{4}He dipper fridge.

(c) Front view of the compressor for the ^{4}He dipper fridge.

(d) Front view of the helium level monitor (top) and pressure monitor (bottom) for the ^{4}He dipper fridge.

Figure 2.9: Photos of the ^{4}He dipper fridge used in the current experiment.

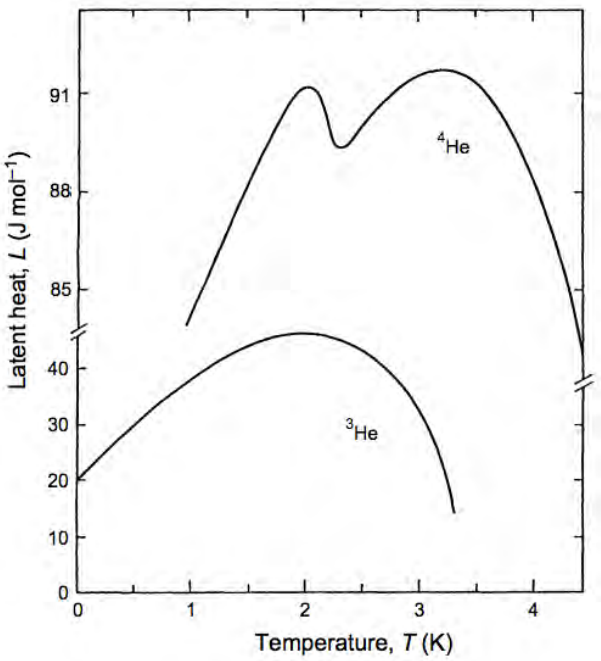

Figure 2.10: The latent heat of evaporation as a function of temperature for helium-3 and helium-4. Figure was taken with permission from ref. [24].

Some of our experiments were conducted in ^{4}ICE$^{\text{DIPPER}}$ Variable Temperature Insert (VTI) inside a liquid helium plant (Cryomech®LHeP), which can be briefly summarized as a cryogenic dewar with a helium reliquefier. Thus I will take a short section below to describe how this system works part by part.

Variable Temperature Insert (VTI) system

Cooling mechanism The ^{4}ICE$^{\text{DIPPER}}$ VTI employs a helium-4 pot (1 K pot) to provide cooling power for experiments, which can be directly conducted on the tip of the probe or on a customized stage attached to the helium pot. The entire experiment is always under vacuum when in operation and sealed in a brass vacuum can. An external turbo pump is used to create the vacuum prior to any measurement. A valve is installed on the top of the probe in order to seal the vacuum can once the pressure drops to operational value.

The way the helium-4 dipper fridge cools down an experiment can be divided into two parts and described below, the first part is directly by the liquid helium inside of the dewar, and the second part is by using VTI's ^{4}He pot.

- When the experiment is set up and sealed in sample space (vacuum can) in vacuum, the probe will be inserted into the helium plant and directly immersed in liquid ^{4}He. Then introduce "exchange gas" to the experimental setup by letting a very small amount of ^{4}He gas into the sample space. Because of the comparatively low pressure and high temperature inside of the vacuum can, the exchange gas (^{4}He) will stay as gas instead of becoming liquid as that outside. It will transport heat back and forth between the experimental setup and the wall of vacuum can, which is in direct contact with liquid helium-4 at $\sim$ 4.2 K. This is the first stage of cooling, it only goes down to about 20 K because the exchange gas has to be extracted before it condenses in sample space at lower temperature. In addition to that, the cold vacuum environment in sample space behaves as a cryo-pump and tries to pull gas into it, causing a competition between it and external pump. In a word, the colder the sample space gets, the harder it is to extract exchange gas, thus it has to be done, and therefore terminating the first stage of cooling, before it goes below 20 K.

- The second stage of cooling depends on the way the VTI's helium pot works. That is, it makes use of the latent heat of helium during a liquid-to-gas phase transition (see figure 2.10). When the helium pot on the probe is filled with liquid ^{4}He coming from the inside of the dewar through a capillary, pumping on the helium pot with an external pump (in our case, it was an Adixen®dry pump) will "force" the liquid helium to evaporate by reducing the pressure in the pot. This "forced" evaporation will take heat from its environment due to latent heat during liquid-to-gas phase transition. The needle valve that controls the capillary from the inside of the dewar to the helium pot can be used to control this pumping rate, and ultimately to control the cooling rate. This completes the second step of cooling, and experimentally the lowest temperature we achieved at this stage of cooling was 1.26 K.

System wiring At the top of the ^{4}ICE$^{\text{DIPPER}}$ VTI, there is a 24-way-Fischer-connector. Apart from 8 wires that are unused, this 24-way-Fischer-connector was divided into two separate connectors (one 6-way-connector, one 10-way-connector) that are wired to a thermometer (generic Allen-Bradley carbon re-

sistor) on the 1 K pot through two Constantan twisted pairs, a heater on the 1 K pot though a pair of 36 standard wire gauge (SWG) copper wires, and 5 twisted pairs of Constantan wires open for experimental design.

Besides the 24-way-Fischer-connector, 9 SMA connectors are installed on a non-grounded plate on top the probe as well. The 9 SMA connectors comprise 4 co-axial cables and 5 SWG copper wires, all open or experimental design.

Helium recovery system

The ^{4}He gas being pumped out of the 1 K pot is recollected from the outlet of the pump into a leak-tight and pressurized gas line system installed in the lab. Then the gas is sent to a helium condenser to be liquified and stored in the dewar again.
The helium liquefier is mainly made up by two parts: the compressor, and the cold head. The compressor supplies high and low pressure ^{4}He gas for the cold head, when the helium gas expands suddenly because of a change from high pressure to low pressure in the cold head, it takes heat and thus cools the cold head to below $\sim$ 4 K. The gas is then returned to the compressor and water cooled to remove the heat it carries and get ready for next cycle of cooling. Now when the helium gas pumped out of 1 K pot returns to the dewar through the recovery system, it reaches the cold head mounted on top of the dewar (see figure 2.9(b)), exchanges heat with it, and condenses before it completes it cycle by once again going to the dewar.

Apart from the above major parts, the Cryomech®helium plant also came with a liquid helium level monitor and a pressure monitor/control (see figure 2.9(d)).

2.2.2 ^{3}He-^{4}He dipper fridge (Lemon fridge)

The $^{\mathrm{DRY}}$ICE$^{\mathrm{4TL}}$ System is a dry helium fridge system that uses a closed loop of continuous ^{4}He flow, plus a separately enclosed ^{3}He in the probe to cool down an experiment. The low temperature limit in theory is 300 mK, and 375 mK in practice. The system is mainly composed of the following parts: the main body

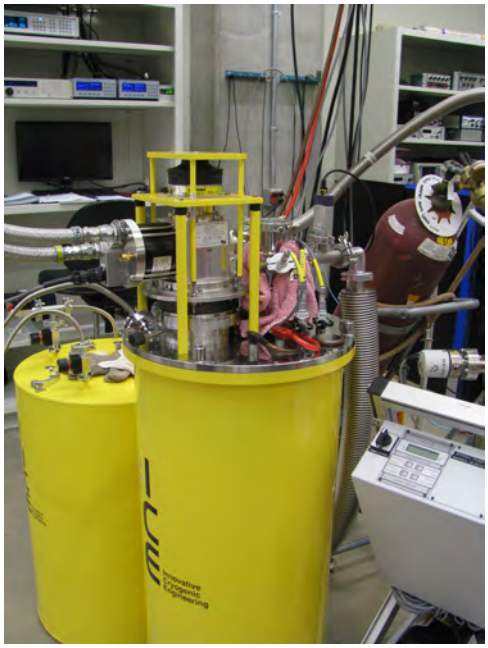

(a) Front view of the ^{3}He/^{4}He fridge.

(b) ^{4}He condenser located on top of the OVC of ^{3}He/^{4}He fridge.

(c) Front view of the compressor for ^{3}He/^{4}He fridge.

(d) ^{3}He probe in the VTI sample space of the ^{3}He/^{4}He fridge.

Figure 2.11: Photos of the ^{3}He/^{4}He fridge used in the current experiments.

of the fridge, a probe, a dump, and a dry mechanical pump (manufactured by Adixen®).
The main body of the fridge is where the first stage of cooling takes place, and it can be further broken down in a 50 K plate, a 4 K plate, and a variable temperature insert (VTI). All these three parts are linked together by the continuous ^{4}He flow path. Furthermore, a superconducting coil is also installed inside the main body of the system around the VTI sample space to generate a uniform magnetic field along z-axis to accommodate experimental design.

The probe used on this system is similar but more complex than that on ^{4}ICE$^{\text{DIPPER}}$ fridge. It does not have a ^{4}He pot as the ^{4}He dipper fridge but instead a ^{3}He pot, that is part of an enclosed two-way path for helium-3. The entire path also includes a sorb, which when cold behaves as a mini cryo-pump on ^{3}He, and a gas chamber at the very top of the probe to store all the ^{3}He gas at room temperature. In addition, the probe has a 1 K stage that is essentially a heat exchanger, on which an aluminum vacuum can is mounted.

The dump here is merely a buffer used to store extra ^{4}He gas outside of the main body of the fridge. It works only below atmospheric pressure and has a pressure gauge on top for real-time monitoring, and a safety valve to release gas when over-pressured.

The dry rotary pump used here is accompanied by a home-made concrete block (see figure 2.12(a)) on one side of the pumping line to eliminate some of the vibration from the pump. It also has a gas filter attached to its inlet to constantly clean the incoming ^{4}He gas.

Cooling mechanism

The first stage of cooling of the $^{\text{DRY}}$ICE$^{\text{4TL}}$ system is similar to that of ^{4}ICE$^{\text{DIPPER}}$ system describe above, except for that here the VTI, playing the role of ^{4}He pot, is permanently fixed to the main body of the system. Starting with the cold head on top of the main body of the fridge, helium-4 gas is cooled and condensed in the cold head before it enters VTI in liquid form as is expected through a needle valve. The external pump (see figure 2.12(a)) on the VTI

pumps (force to evaporate) the ^{4}He from the VTI, which is thus cooled to $\sim$ 1.3 K, and pushes it into the dump (see figure 2.12(b)) before it is re-liquefied by the cold head again.

(a) The external pump used on VTI.

(b) The dump used as buffer to store ^{4}He gas outside of the main body of $^{\mathrm{DRY}}$ICE$^{\mathrm{4TL}}$ System.

Figure 2.12: External parts of $^{\mathrm{DRY}}$ICE$^{\mathrm{4TL}}$ System.

If the probe is already inserted into the VTI sample space, which is enclosed by the VTI at $\sim$ 1.3 K and filled up with helium-4 as an exchange gas, then every part of the probe except for those inside the vacuum can under vacuum will be cooled to a temperature below 2 K. At this temperature, the sorb absorbs all the helium-3. By heating it up, one is able to release the ^{3}He gas and pass it down into ^{3}He pot, which may be hotter than 2 K due to it is isolated from the VTI. When this ^{3}He gas passes through the 1 K stage in either direction, which is cooled by VTI at $<$ 2 K, it may transfer its heat to the stage and condense into liquid. Due to gravity, it will drip down to ^{3}He pot. If the pot is hot enough to boil it off, then it becomes gas and goes up toward 1 K stage again. This way, the released ^{3}He gas behaves as exchange gas between 1 K stage and ^{3}He pot (and therefore the rest parts inside the vacuum can). In the end, when thermal equilibrium is struck, all parts inside the vacuum can are cooled to below 2 K and the ^{3}He will start to condense into helium-3 pot. If it is intended to further cool down the experiment, one

now must heat up the sorb to release ^{3}He gas and wait for a few hours to let enough ^{3}He condense in helium pot before starting the third stage of cooling.

In the third stage of cooling, as the sorb cools down, it starts to absorb ^{3}He gas. This makes it behave as a pump on ^{3}He pot, causing liquid ^{3}He in pot to go through a first order phase transition from liquid to gas, which takes heat (see figure 2.10) from its environment and further cools the helium pot as well as the experimental setup attached to it. The cooling power is directly correlated to the pumping rate of ^{3}He, which depends on the temperature of the sorb. In practice, when sorb is maintained at ~ 2 K, the helium pot reaches its base temperature at ~ 375 mK.

Wiring

The wiring for $^{\mathrm{DRY}}$ICE$^{\mathrm{4TL}}$ system has been designed almost the same as that for ^{4}ICE$^{\mathrm{DIPPER}}$ except for one change: there is one additional thermometer and one additional heater installed to monitor and control the temperature of the sorb, they are wired to four pairs of twisted pairs from the 24-way-Fischer connector. Because of this nearly identical design, the cable and sample stage are interchangeable between the two systems. In the current experiment, we used the same cable as we used on ^{4}ICE$^{\mathrm{DIPPER}}$ system while we made a new sample stage, which will be described in a later section.

Thus, we conclude the introduction to the experimental equipment. We can now go on and take a look at how the measurements on our samples are done.

Magnet

One of the major additional features of $^{\mathrm{DRY}}$ICE$^{\mathrm{4TL}}$ System as compared to the ^{4}ICE$^{\mathrm{DIPPER}}$ system is that it has a built-in superconducting coil inside the OVC which allows us to apply a magnetic field parallel to the longitudinal direction of the probe. The superconducting coil is powered by Model 4Q06125PS four quadrant power supply, controlled by a model 430 power supply programmer (both made by American Magnetics, Inc.). A persistent switch, which is essentially a piece of superconductor that is integrated into the circuit, is used to cut the coil off from the power supply when its cold (superconducting), or to

Max current	Current range
0.180 A/s	0–25 A
0.009 A/s	25–35 A
0.0045 A/s	35–47.07 A

Table 2.1: The maximum ramping rates of current can be applied to the superconducting coil at different current range.

connect it to the power supply when its warm (at normal state). This allows us to connect the superconducting coil to the power supply by applying heat to the persistent switch, then ramp up the magnetic field by increasing the current in the coil with the power supply, and let the superconducting coil to either hold up a target current, thus a magnetic field, with the power supply, or do so on its own should we cut it off from the power supply by cooling down the persistent switch back to below its superconducting transition temperature.

This superconducting coil is theoretically capable of applying a magnetic field up to 9 T, which, by the conversion ratio of 1.912 kG/A gives the maximum current allowance of the persistent switch as 47.07 A. Furthermore, the ramping rate of current are also limited due to the high risk of magnet quenching when the maximum rate is exceeded, which in the end limits how fast we ramp up the magnetic field. The maximum ramping rate of current differs at different current range, and in practice we found the following values:

2.3 Four-probe-measurement of resistivity

2.3.1 Collinear four-probe-measurement

The collinear four-probe-measurement uses an aligned and equally spaced set of four probes to measure the resistance of a sample, the outermost two probes are current source, and the voltage across the inner two probes are measured to determine the resistance between them. A further calibration and calculation based on the shape of the sample, the thickness, and the distance between probes can eventually give the resistivity of a sample of a large variety of shapes. Despite its merit, collinear four-probe-measurement bears the following constraints:

- The sample is assumed to be isotropic and uniform in terms of electrical conductivity so that there is no preference in the direction of aligning the probes along the surface of the sample. It is also assumed that the current lines have radial symmetry.
- The four probes have to be far from the edges of the sample so that the effective area of the sample can be considered as infinitely large.
- The diameter of the probes (contact face) must be smaller then the distance between probes.
- A high carrier density of the sample is assumed in order to neglect the effect from electron and hole injections from the probes.

Resistivity calculation

Assume that the contact area between the probes and the surface of the sample is small, and that the distance between nearest probes is much smaller than the thickness of the sample. Then for the electrical potential, V_f, on the surface of the sample at a spot that is at a distance of r_1 from one of the current probes, and of r_4 from the other, we have:

$$V_f = (\frac{\rho I}{2\pi r})(\frac{1}{r_1} - \frac{1}{r_4}) \tag{2.1}$$

Here we have defined r_i $(i = 1, 2, 3, 4)$ to be the distance from the local area under inspection to each of the four probes, among which probe 1 and 4 carry current. Given this equation, then by measuring the potential difference (voltage) between probe 2 and 3, then we will have an expression for the resistivity of the sample:

$$\rho = 2\pi s \cdot (V/I) \tag{2.2}$$

Where "s" is the distance between nearest probes along the surface of the sample.

Now, if however the thickness (δ) of the sample doesn't satisfy the constraint that $\delta >> s$, but instead the opposite limit, where $\delta << s$ (as in the current experiment), then the sample can be regarded as an effectively two dimensional

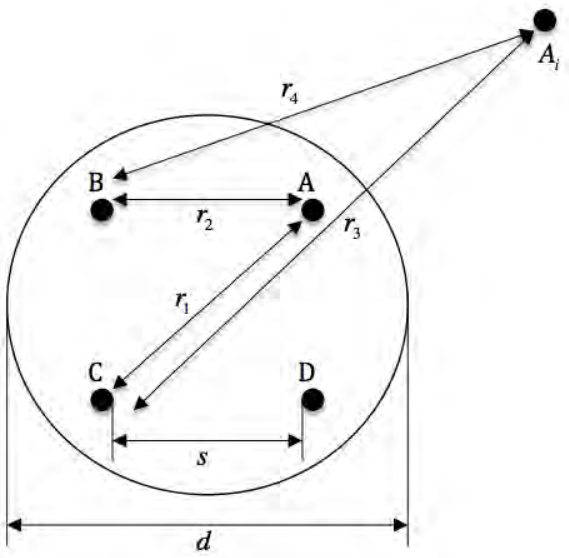

Figure 2.13: A scheme of square four-probe-measurement of resistivity on a circular shaped sample.

and infinitely large sheet, whose resistivity is:

$$\rho = \frac{V}{I} \cdot \frac{\pi\delta}{\ln 2}. \tag{2.3}$$

2.3.2 Square four-probe-measurement

While the collinear four-probe-measurement can be applied with fair accuracy on large samples, which can be regarded as infinite in area, a square four-probe-measurement has an advantage in measuring small samples. The arrangement of the probes in a square four-probe-measurement is such that each probe is at a corner of a square of side length (denoted by "s"). The current is applied to a pair of nearest neighbour probes, and the voltage across the other pair is measured to determine the resistivity of the sample. In order to acquire an accurate value of the resistivity of the sample, a correction factor is needed, which is based on the shape and size of the sample. Here the factor is derived for the same geometry as samples in the current experiment.

Resistivity calculation

Similar to the previous calculation method for a collinear four-probe-measurement, we have the following equation:

$$\rho = 2\frac{V}{I} \cdot \frac{\pi\delta}{\ln 2} \tag{2.4}$$

As for the correction factor, consider a circular shaped sample of diameter "d" and thickness "δ," and the square formed by the four probes and the circular sample are concentric. By investigating the image current in z-plane after a bilinear transformation of the configuration from real space to z-plane and then transforming it back to real space, we have a local electrical potential expressed as:

$$V = \frac{\rho I}{2\pi} \cdot (\frac{2}{Q} + \frac{M}{\delta}). \tag{2.5}$$

Here Q and M are two parameters given by:

$$\frac{1}{Q} = -\frac{1}{r_1} + \frac{1}{r_2} - \frac{1}{r_3} + \frac{1}{r_4} \tag{2.6}$$

$$M = M(\frac{r_1}{2\delta}) - M(\frac{r_2}{2\delta}) + M(\frac{r_3}{2\delta}) - M(\frac{r_4}{2\delta}) \tag{2.7}$$

Where r_i (i=1,2,3,4) is labelled as in figure 2.13, and the function M is tabulated by A. Uhlir [25]. In the end, for $\delta/s << 0.5$, it can be expressed as:

$$\rho = \frac{\pi\delta R}{\ln 2} \cdot F(d, s) \tag{2.8}$$

Where the correction factor $F(d, s)$ is tabulated by A. Uhlir [25].

2.4 sample stage design and probe wiring

2.4.1 ^{4}He dipper fridge

sample stage design

The sample stage designed for ^{4}He dipper fridge was meant for collinear measurements on rectangular shaped samples. The cell was machined from a high

purity oxygen-free copper rod. The advantages of using copper as the material of sample stage is as follow:

- Copper is a very good thermal conductor (yet never demonstrated any superconducting effects at any temperature), so it guarantees a uniform temperature across the sample stage even at a very low temperature. This contributes to the accuracy of the temperature measured by the thermometer located a certain distance from the actual sample.
- Copper has a relatively small thermal expansion coefficient (see figure 2.16), therefore it won't cause too much stress on the glass substrate when cooled to low temperatures.

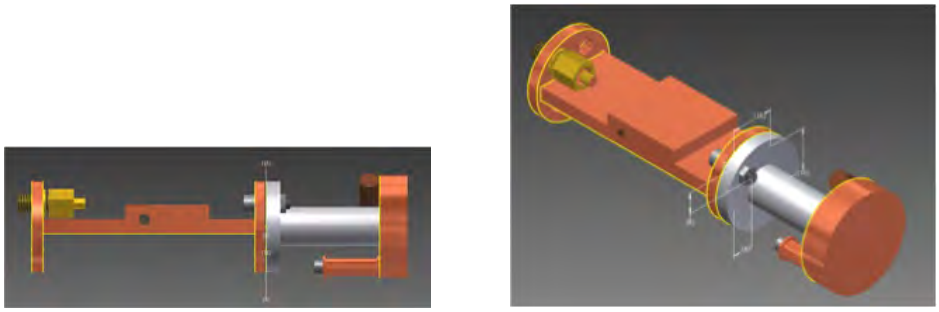

(a) Corner view of the sample stage design for ^{4}He dipper fridge.

(b) Side view of the sample stage design for ^{4}He dipper fridge.

Figure 2.14: Design of the sample stage for the ^{4}He dipper fridge.

The design of the cell is as illustrated in 2.14(a) The design of the cell incorporated the needs of hosting a sample/substrate, four SMA connectors for the four-probe-measurement, a thermometer, and a heater to control the temperature. The position of the bobbin holding the thermometer is chosen to be as close to the sample as possible to optimize the temperature measurement. An additional thermometer is placed at one side of the sample stage in case of need of a second calibrated thermometer (see figure 2.14(b)).

Substrate

The substrate chosen for the aforementioned sample stage is amorphous glass (26×15 mm), cut from a microscope slide ($26 \times 76 \times 1$ mm, by Technologist Choice^{TM}).

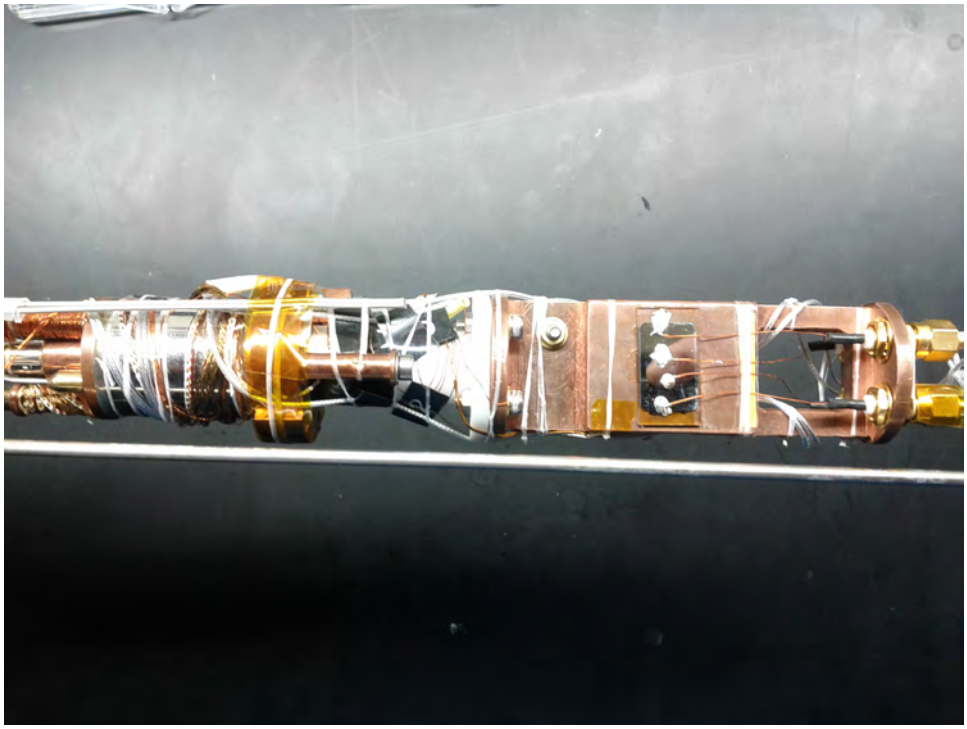

(a) Top view of the sample stage for ^{4}He dipper fridge.

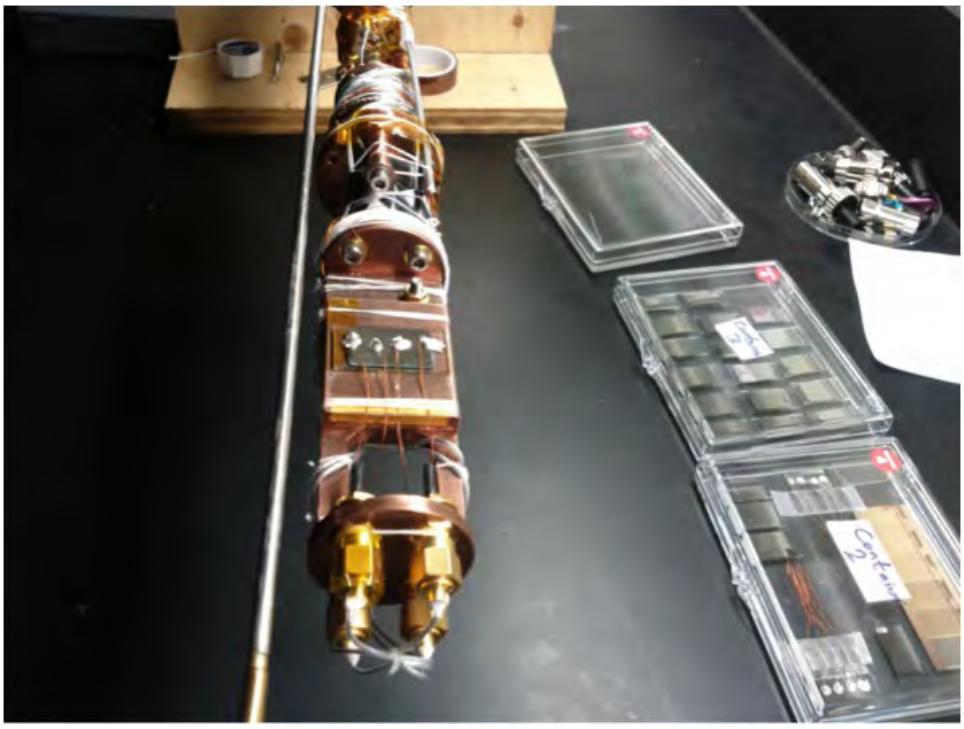

(b) Front view of the sample stage for ^{4}He dipper fridge.

Figure 2.15: Photos of the sample stage for ^{4}He dipper fridge.

Thermalizing

The whole sample stage was designed to stand off from the ^{4}He pot on the fridge, which is the major source of cooling power. This is achieved by connecting the sample stage to the fridge with a teflon piece. Given the low thermal conductivity of teflon (see figure 2.16), the sample stage is in nearly total thermal isolation from the helium pot. Then a strand of thin copper wire, or a thin copper sheet, is attached to both the helium pot and sample stage to conduct heat between them. The merit of such a design is that, while the teflon piece creates a nearly complete insulation between the sample stage and helium pot, by connecting the copper wire of a controlled size (diameter and length) to both, a well controlled thermal conductivity between the two is achieved.

The ultimate purpose of a controlled thermal conductivity between the sample stage and helium pot is in the fact that different values of thermal conductivity allows for different maximum temperature gradient between the two. This temperature gradient is essential to the controlling of the cooling or warming rates of the sample stage. If the sample stage is warmed up or cooled down too fast, the sample stage itself may not be able to reach a thermal equilibrium as a whole during the process, which leads to inaccurate measurement. Therefore, better control over the thermal conductivity eventually results in a better accuracy of measurement.

In addition to the above, when the helium in helium pot reaches its boiling point at the pressure inside the pot, all the helium will suddenly be boiled off, and the cooling power will abruptly drop to zero once the pot is empty. Therefore making it difficult for the pot, or the sample stage if directly attached to the pot, to dwell at this temperature for long enough to take measurement. Thus if a big enough temperature gradient is created between the sample stage and helium pot, on one hand, the sample stage may cross this temperature point while the pot hasn't, or on the other hand, when the temperature of helium pot reaches the boiling point, a sudden loss of cooling power wouldn't result in a sudden warm up of the sample stage.

The substrate is attached to the sample stage by gluing them together with General Electric varnish (GE varnish). The advantages of using GE varnish

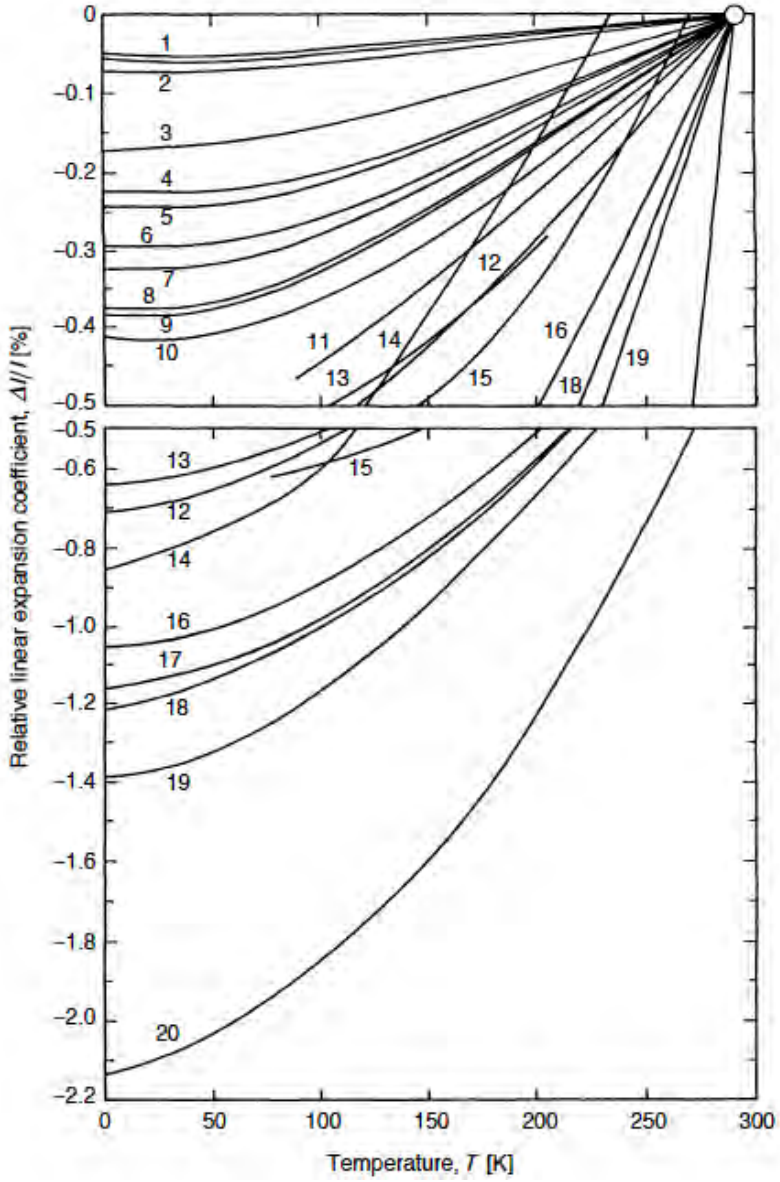

Figure 2.16: The expansion coefficients for some of the most common solids. (1) Invar (upper), Pyrex (lower), (2) W, (3) nonalloyed steel, (4) Ni, (5) Cu0.7Ni0.3, (6) stainless steel, (7) Cu, (8) German silver, (9) brass, (10) Al, (11) soft solder, (12) In, (13) Vespel SP22, (14) Hg, (15) ice, (16) Araldite, (17) Stycast 1266, (18) PMMA, (19) Nylon, (20) Teflon. Figure credit to ref. [24].

are that

- its thermal conductivity is better than most of the glues or epoxies.
- it is easy to solve and remove it by applying ethanol solution.

The four stripped copper wires (diameter$\sim$ 0.009 in) used in the measurement are soldered to the same sides of the four SMA connectors held on sample stage. Then, in order to thermalize the sample, they are wound around two "legs" of the sample stage with ultra-thin cigarette paper underneath (for electrical insulation) before contacting the surface of the sample.

Wiring

Once the sample is attached to the sample stage, the four copper wires, extended from the SMA connectors, are placed in contact with the surface of the sample with equal space between nearest neighbours, silver paint (Pelco®Colloidal Silver Liquid, product No. 16034) is then applied to them for better electrical contact. Silver epoxy (AiT®Silver Epoxy, product No. EG8020) is also applied afterwards to hold down and stress release the wires to ensure steady contacts between all leads and the surface of the sample throughout the entire preparation and measurement.

The four coated wires needed by the thermometer (Carbon Glass Resistor, model: CGR-1-500) go directly from it, through quick connectors, to two twisted pairs of constantan wires that came with the fridge's probe, and they are colour coded the following way:

Green $\rightarrow V^-$	Black $\rightarrow I^-$
Yellow $\rightarrow V^+$	White $\rightarrow I^+$

The twisted pairs of wires are soldered to four terminals (E,F,H,J) of a 24-way-Fischer connector on top of the probe (see figure 2.17). A Belden 8723 cable was then configured to connect the 24-way-Fischer connector to the Crycon®32B for temperature measurement.

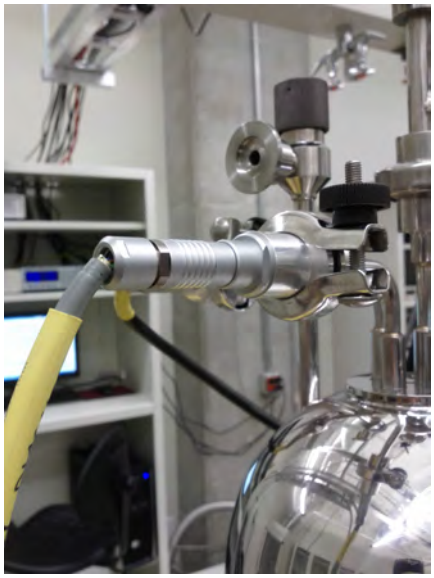

Figure 2.17: Fisher connectors on top of a ^{3}He dipper fridge probe.

Test result

Once the fridge is set up, a test run on a thermal deposited tin film on glass substrate was put on and a resistance measurement was conducted. The results are as follows:

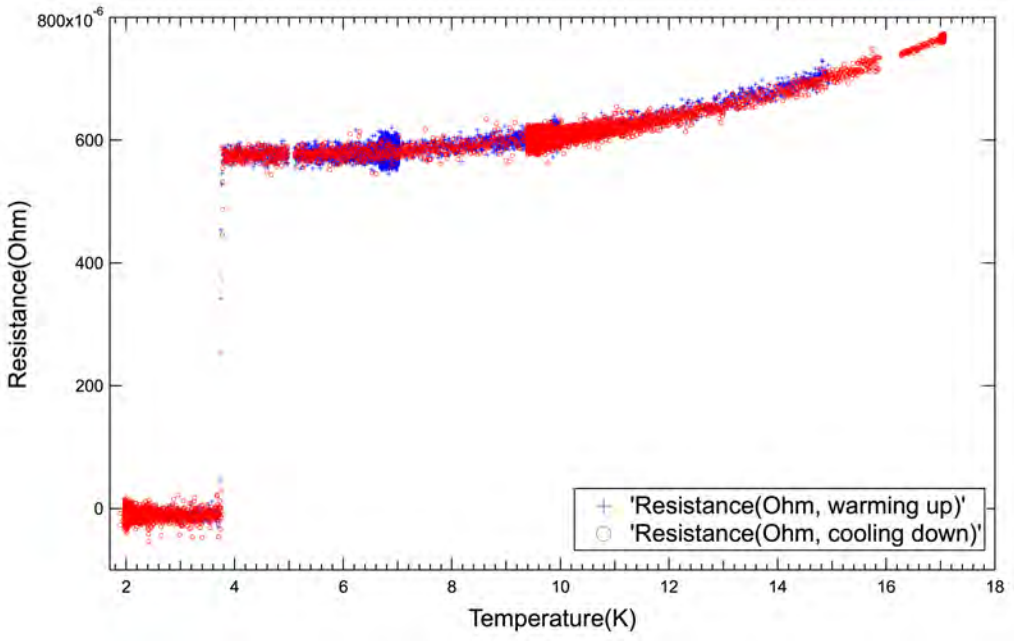

Figure 2.18: Zero-field measurement of resistance of Sn film on glass substrate.

From figure 2.18, we can see the two measurements of resistance (one taken while the sample was warming up, the other taken while the sample was cooling down) agree with each other very well. A lack of hysteresis in this case indicates good thermalization of the sample film. A closer look at the sudden drop of resistance (transition to superconducting state) reveals a transition temperature $\sim$ 3.76 K, which agrees with previous reports (3.72 K [26]), and also proves this point.

2.4.2 ^{3}He/^{4}He dipper fridge

Sample holder design

Because the sample stage of ^{3}He/^{4}He dipper fridge was of identical design to that of ^{4}He dipper fridge, the two fridges can share each other's sample stage. However, in order to improve the accuracy of resistivity measurement, a new sample stage meant for square four-probe-measurements was designed for ^{3}He/^{4}He dipper fridge. In this new sample stage, if the z-axis is directed along the length of the probe, the plane of sample film is then in x-y plane. Furthermore, the new sample stage design, instead of using silver paint and silver epoxy to make contacts between leads and the sample, if uses four spring-loaded (pogo) pins to make pressure contact with the sample to take measurement.

The new sample stage (see figure 2.19(a)) was again machined from a high purity oxygen-free copper rod, and has cylindrical symmetry, it can be regards of an assembly of three pieces: a pin unit (see figure 2.19(c)), a sample stage, and a holding piece (see figure 2.20(b)).

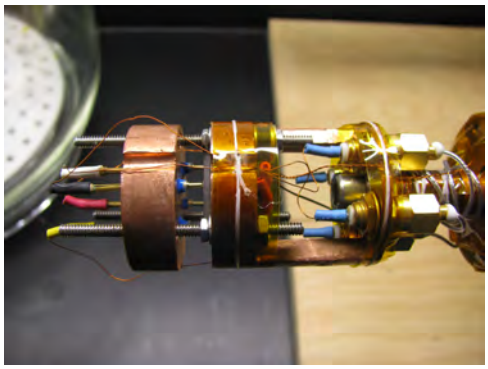

(a) Top view of the sample stage for the ^{3}He/^{4}He dipper fridge.

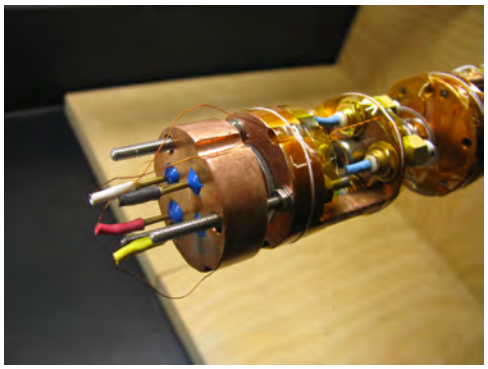

(b) Front view of the sample stage for the ^{3}He/^{4}He dipper fridge.

(c) Side view of the pogo pin unit of the sample stage for the ^{3}He/^{4}He dipper fridge.

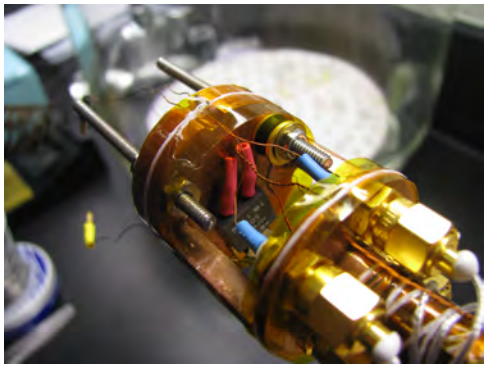

(d) Backside view of the pogo pin unit of the sample stage for the ^{3}He/^{4}He dipper fridge.

Figure 2.19: Photos of the sample stage for the ^{3}He/^{4}He dipper fridge.

In addition, the sample stage accommodates a heater and a thermometer bobbin at the back of the sample stage (see figure 2.19(d)), which guarantees the shortest distance from them to the sample and thus a more accurate reading of temperature. Four SMA connectors are also held on the sample stage at its tail right before the copper piece that bridges the sample stage to the ^{3}He pot.

Substrate

Apart from all the experimental samples tested, which will be described in a later chapter, the substrate that eventually won over the rest is a circular silicon dioxide quartz disc. It is 3/4 inches in diameter and 1/16 inches in thickness. 99.995% purity, manufactured by GM associates Inc. (see figure 2.20(a)). Such

(a) The SiO_2 quartz disc used as substrate on ^{3}He dipper fridge.

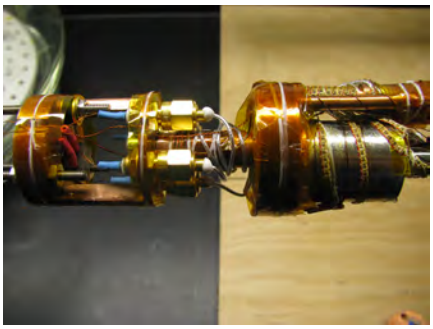

(b) The sample stage is directly connected to ^{3}He pot on the probe through a copper support piece.

Figure 2.20: Some details regarding to the thermalization of samples.

a substrate can withstand extreme temperatures and pressures, and can be recycled for multiple times after uses. Moreover, the thermal conductivity of silicon dioxide quartz is slightly better than that of amorphous glass, which helps the thermalization of the sample.

Sample thermalizing and wiring

As shown in figure 2.19(c), each of the pogo pins (ED90392 ND, manufactured by Mill-Max®) is soldered to a quick connector that is glued to a copper unit (pin stage) with epoxy (Tra-bond®2151). From the quick connector, a copper wire ($\phi = 0.009$ in) is soldered to a SMA connector held on the sample stage behind the sample (see figure 2.19(d)), and a co-axial line that extends to the outside of the fridge is attached to the other side of the sample stage. The co-axial line is connected to a cable that leads to a Lakeshore®model 370 AC resistance bridge through another set of SMA connecters on the top of the fridge (see figure 2.21).

Thermalizing

Unlike the ^{4}He dipper fridge, the sample stage is directly mounted to the helium-3 pot on probe with a copper piece (see figure 2.20(b)). This is due to the limited cooling power of the ^{3}He pot as compared to that of ^{4}He pot on the ^{4}He dipper fridge. Therefore good thermal contact is required in this case. Because of the poor thermal conductivity of silicon dioxide at low tem-

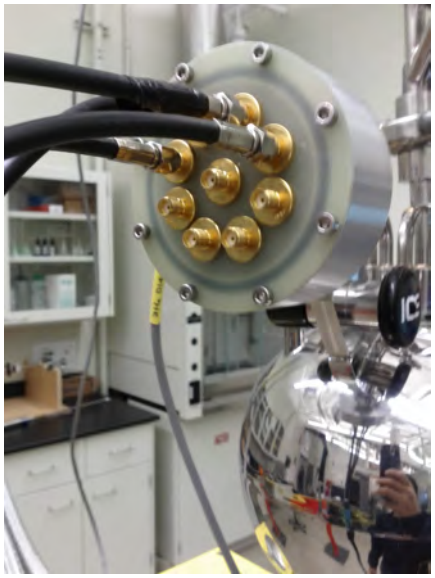

Figure 2.21: The SMA connectors on top of the probe for ^{3}He/^{4}He dipper fridge.

perature, the sample film deposited on the 1/16-inch-thick quartz substrate is almost entirely thermalized just through the four leads pressed against it. The heat goes from the film to one side of the four leads, then to the other side into the copper wire, which is wound on the copper sample stage, and eventually taken away by the ^{3}He pot. As mentioned before, a heater and a thermometer (Lakeshore®CX-1010-CU-HT) is mounted on the sample stage right at the back of the substrate bed (see figure 2.19(d)). The wires come out of the substrate are wound around the connecting piece between the ^{3}He pot and the sample stage before going into four quick connecters to two pairs of constantan wires.

Wiring

The wiring of the sample stage on ^{3}He dipper fridge is similar to that on ^{4}He dipper fridge. The four leads used for resistance measurements are wired through copper wires ($\phi \sim 0.009$ in) and quick connectors to four SMA connectors mounted on the sample stage. Then from SMAs, four co-axial lines go directly to the top of the probe to another four, out of nine, SMA connectors. The cable used on the ^{4}He dipper fridge is at this point moved to the ^{3}He dipper fridge for resistance measurements with Lakeshore®model 370 AC resistance bridge.

The thermometers on the 1 K pot, ^{3}He pot, and sample stage are all wired through six pairs of constantan twisted pairs wires to a 24-way-Fischer connector (pins 1-8). Eventually they are connected to a Cryocon®44C cryogenic temperature controller, to which the heater on the ^{3}He pot is also connected with two 36 SWG copper/superconductor wire through a 24-way-Fischer connector (pins 23 & 24). The thermometer and heater on the sorb are wired through two pairs of 42 SWG constantan twisted pairs and one pair of 36 SWG copper twisted pairs, respectively, to a 10-way-Fischer connector (pins 1-6), then go to the same Cryocon®44C control. In addition, an optional heater is mounted on sample and wired through a 36 SWG copper twisted pair to the 10-way-Fischer connector (pins 7 & 8). But in the current experiment, this heater is unnecessary and therefore not used.

Test result

In the first run of the ^{4}He dipper fridge, we had a calibrated thermometer installed. But on the ^{3}He fridge, we did not. Therefore the first thing to do before actually running this fridge for experiments was to calibrate the uncalibrated thermometer (CX-1010-CU-HT) on sample stage by mounting it next to a calibrated thermometer (Ge17035). The result is present as follows:

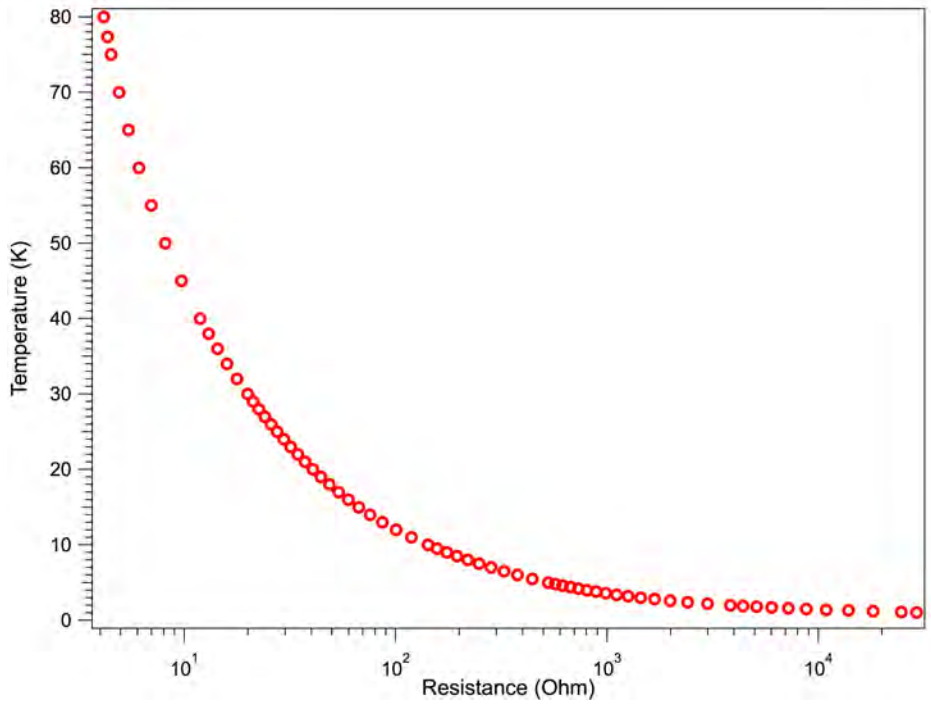

Figure 2.22: Calibration curve of thermometer (CX-1010-CU-HT) using Ge17035 thermometer. The vertical coordinates are temperatures read by the calibrated thermometer, and the horizontal coordinates are the resistance of the uncalibrated thermometer read by Lakeshore®model 370 AC resistance bridge.

From figure 2.22, we were able to upload a set of two hundred data points, which correlated the thermometer's temperatures to its resistances, into a temperature controller so that it displays an accurate temperature with an error ~ 3 mK.

2.5 Labview®program

In order to collect data effectively and efficiently, two Labview®programs were written for zero-field resistance measurements, and 3D mapping in a phase space of temperature, magnetic field, and resistance. While the detailed program scripts are spared from this section, the flow charts of the two programs are presented below:

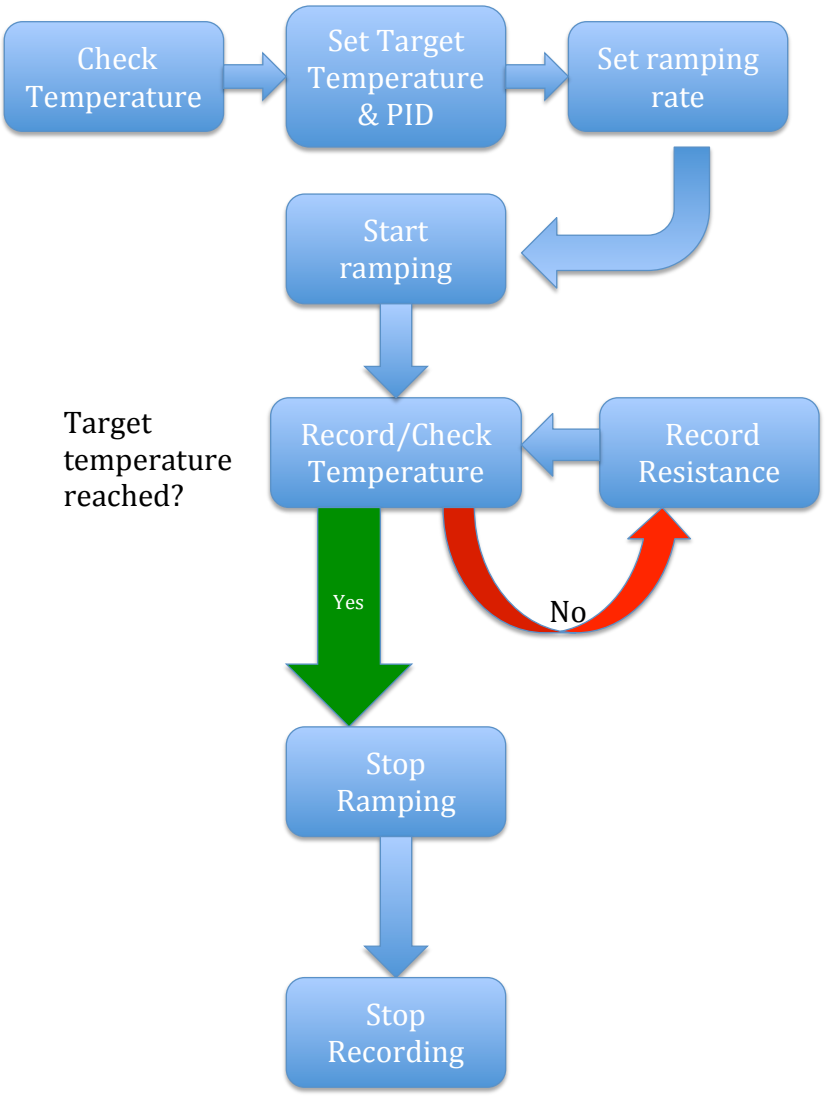

Figure 2.23: The flow chart for the program used in zero-field resistance measurement.

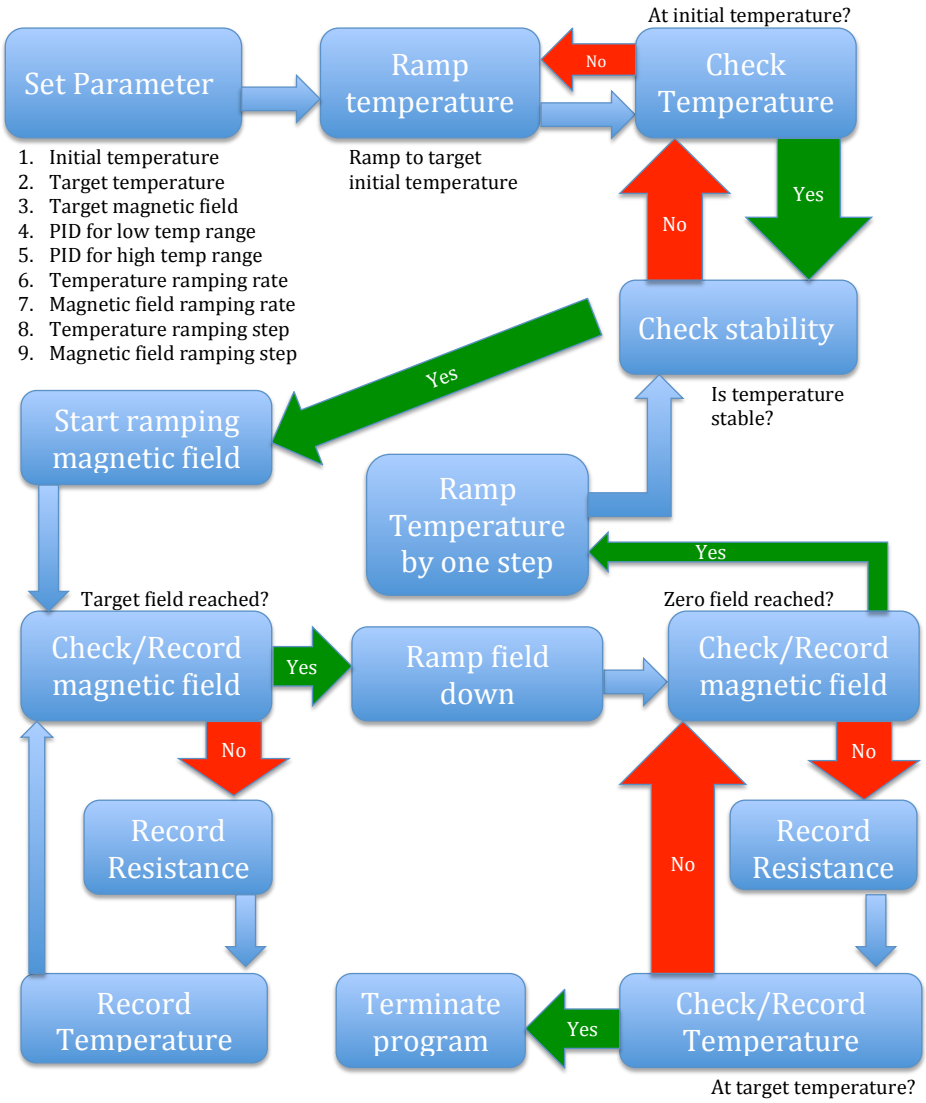

Figure 2.24: The flow chart for the program used in 3D mapping of phase diagrams.

Chapter 3

Experimental results

3.1 Thermometer calibration

For any temperature-related measurement to be accurate, it is necessary to have accurate reading of the temperature of the sample. Thus, before we could take any measurement on either ^{4}He or ^{3}He dipper fridges, careful calibrations of thermometers were conducted on both fridges. This section is dedicated to a description of how these calibrations are done.

3.1.1 Calibration on ^{4}He fridge

The ^{4}He came with an uncalibrated carbon-glass-thermometer on 1 K stage and, as mentioned earlier, there is an additional thermometer on the sample cell. Our calibration for the thermometer on the 1 K pot was fairly simple, as it was mostly used as just an indicator of the temperature. The most credit of this calibration work was due to our post-doc, Dr. X. Rojas. We measured and recorded its resistance at various temperatures, then plotted them against each other and applied interpolation on the curve. After that, 200 evenly spaced data points were extracted from the dataset of the interpolation (see figure 3.1) and uploaded to a Cryocon®32B, which will internally fit to these data points using preset functions.

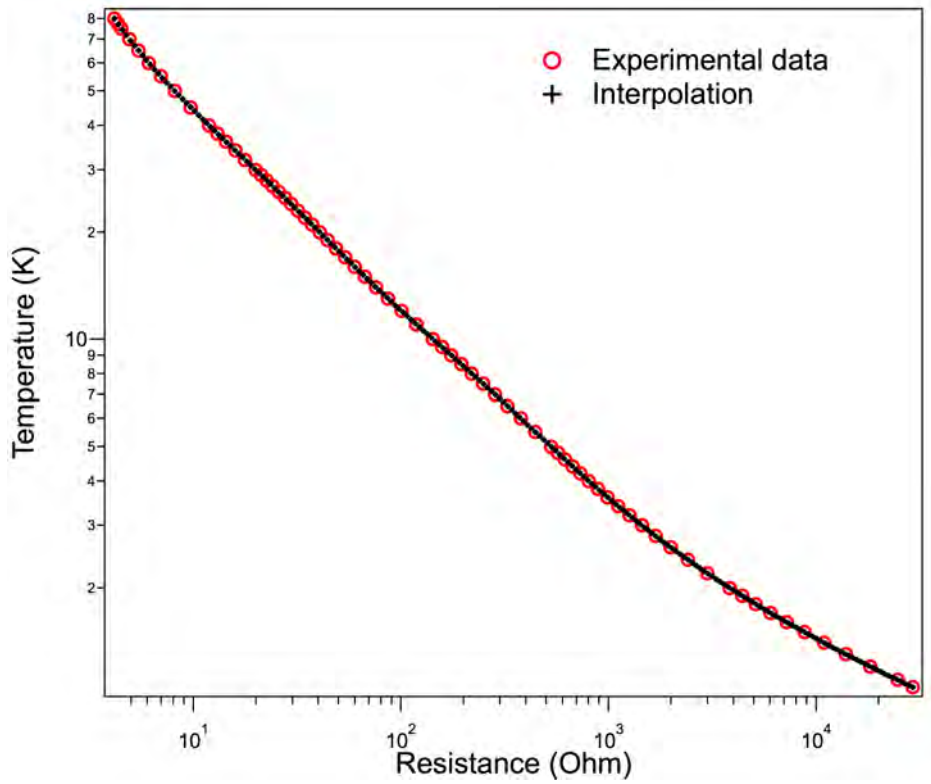

Figure 3.1: Calibration data and its interpolation for the thermometer on 1 K stage of ^{4}He dipper fridge.

Now considering the thermometer on the sample cell. Since we need the temperature readings to be as accurate as possible, we first repeated the measurement of resistance versus temperature on this thermometer (see figure 3.2), then fitted the data part by part for five different temperature ranges using a power law form, which is given:

$$T = A + B \cdot R^C \tag{3.1}$$

where T stands for temperature, R stands for resistance, and A, B, C, are fitting parameters. For the five different temperature ranges, the coefficients are tabulated in table 3.1.

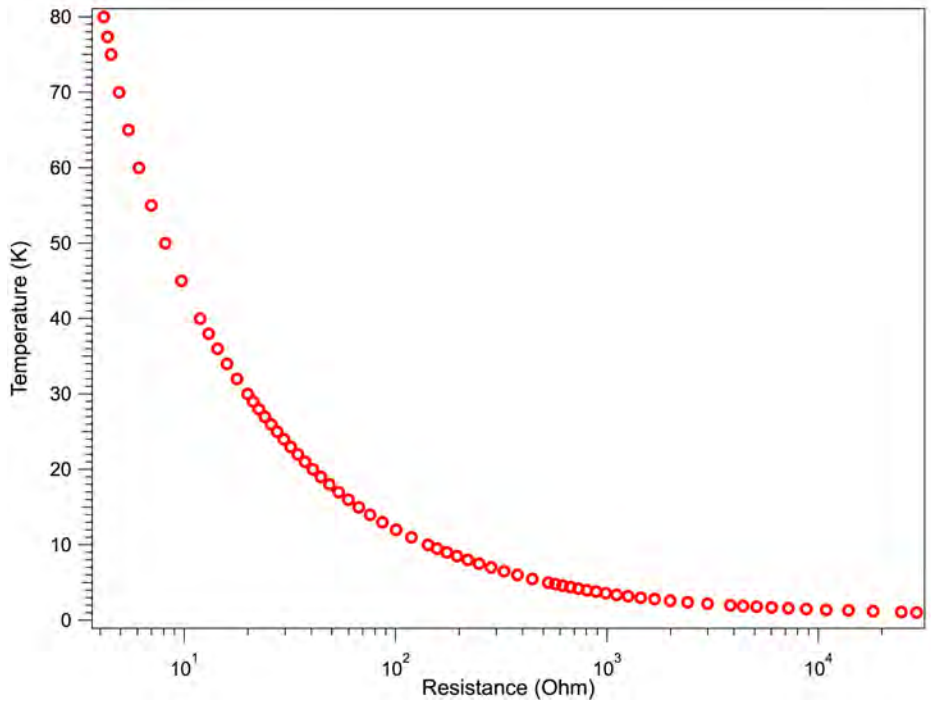

Figure 3.2: Measured data of resistance versus temperature for the thermometer on the sample cell in ^{4}He dipper fridge.

T	1–3 K	3–20 K	20–50 K	50–120 K	120–300 K
A	0.838548	2.95145	13.3926	31.609	80.2589
B	206.812	168790	1.80937×10^{11}	2.85951×10^{18}	1.09174×10^{37}
C	−0.597438	−1.70589	−4.44136	−7.87523	−16.9042

Table 3.1: Coefficients for the power fitting of the calibration curve for the thermometer on the sample cell in ^{4}He dipper fridge.

Thus, in practice, when doing experiments, we measure the resistance of the thermometer, and then convert it to the corresponding value of temperature by directly implementing these fitting functions of the calibration curve in our softwares that are used to take measurements.

3.1.2 Calibration on ^{3}He fridge

As mentioned earlier in chapter 2 that, the $^{\text{DRY}}$ICE$^{\text{4TL}}$ system came with a Ruthenium Oxide thermometer that was only generically calibrated, and there

is an additional thermometer (Lakeshore®Cernox) located at the back of our sample. Therefore, there were two thermometers needed to be calibrated at the same time. In order to achieve a good thermal contact among these two thermometer and the calibrated one, the sample cell was detached from ^{3}He pot on the probe, and the three thermometers, two of which were in bobbins whose contact faces were cleaned with ultra-fine sand paper and isopropanol to ensure a good thermal contact, were all tightly screwed onto the same copper base of the helium pot.

After the room temperature resistances of uncalibrated thermometers were recorded, the probe was inserted into VTI sample space to cool down. The probe, and thus the thermometers, were first cooled down to, and stayed for sufficient time at, the base temperature to allow a thermal equilibrium be reached. Then, as their resistances and temperatures being recorded, they were warmed up slowly to 54 K by applying heat to both the sorb and ^{3}He pot accordingly. The recorded data is here presented in figure 3.3.

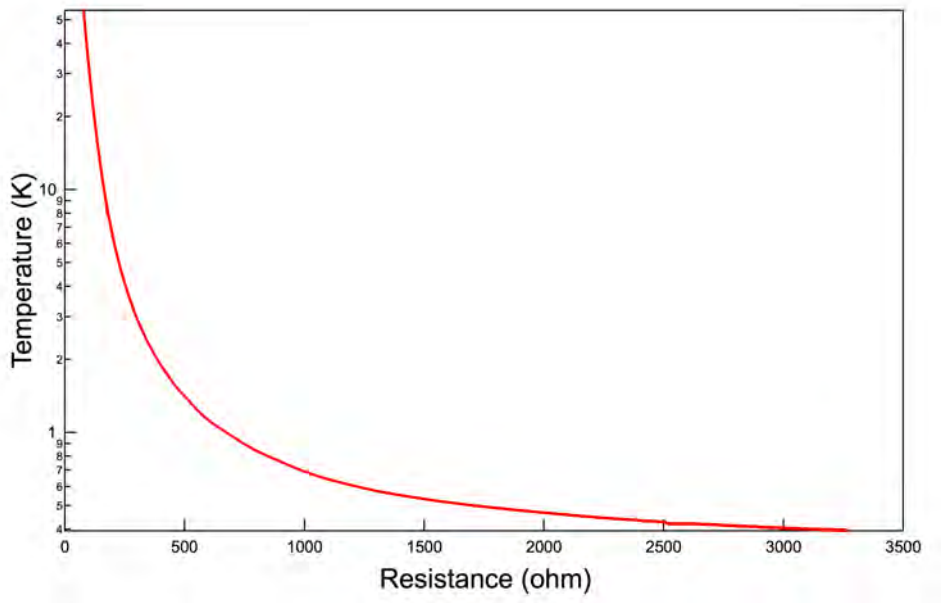

Figure 3.3: The calibration curve taken on the lemon fridge for Lakeshore®cernox thermometer from base temperature to 54 K.

Although this was exactly the same as what we have done for the thermometer calibration on ^{4}He dipper fridge, it was actually insufficient, in the

present case, to yield a satisfactory result due to a wider temperature range. Thus the calibration was performed in two parts and treated differently. The reason for this was that in the first part, which ranges from 4 K to 54 K, the resistances of sensors aren't very sensitive, thus the calibration accuracy is inevitably limited by the thermometers themselves, a crude calibration would have yield as good a result as a fine one. However, in the second part, from 0.3 K to 4.0 K, changes in the temperature can be accurately represented by that in the resistance of the sensor with much smaller tolerance from that in the high temperature range, and therefore it requires a finer calibration.

For this sensitive range of temperature, instead of continuously changing and measuring the temperature, we changed the temperature by steps, and stayed at each step for a significant length of time to ensure that the system has equilibrated. These data points are plotted in figure 3.4, and we can see that they have formed a cluster around each specific temperature point. These clusters are about 0.3 K apart from each other.

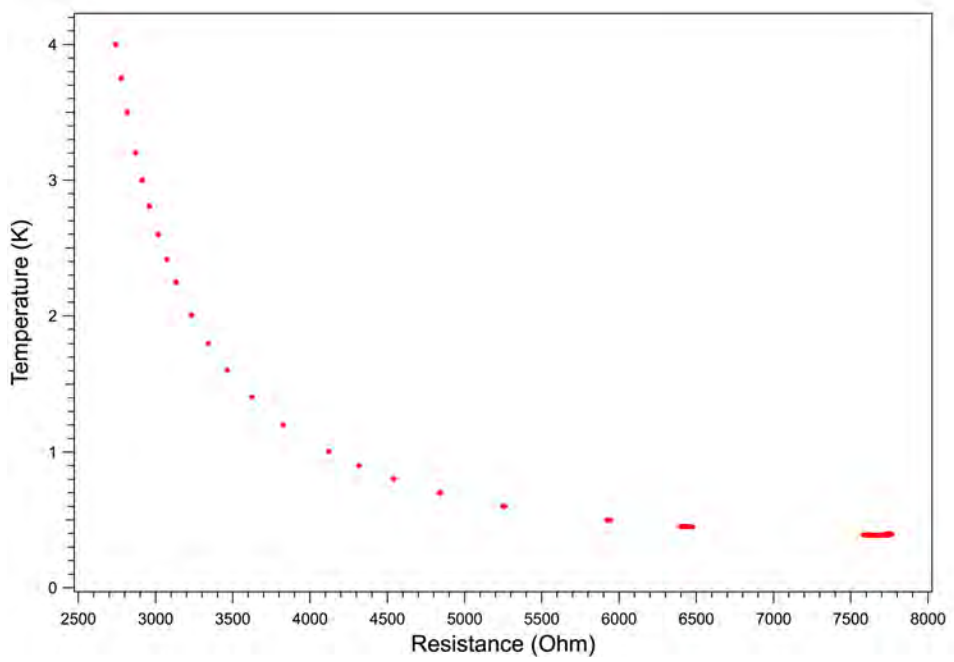

Figure 3.4: Resistance of the Lakeshore®cernox temperature sensor measured at various temperatures.

Measuring the sensors' resistances at various temperatures was only the

first step. The next one was to find the average values of these clusters of data points at different temperatures. Then an interpolation was generated base on these averages (see figure 3.5). At last, a numerical fitting on the interpolations with a polynomial function to the sixth order concluded our calibration for the thermometers at low temperature part as is seen in figure 3.6, from whose residual plot we can confirm a good agreement between the fitting and the data was achieved ($< \pm 10$ mK). Eventually, the fitting function was uploaded to Cryocon®44C so that we would be able to read temperature directly off the equipment.

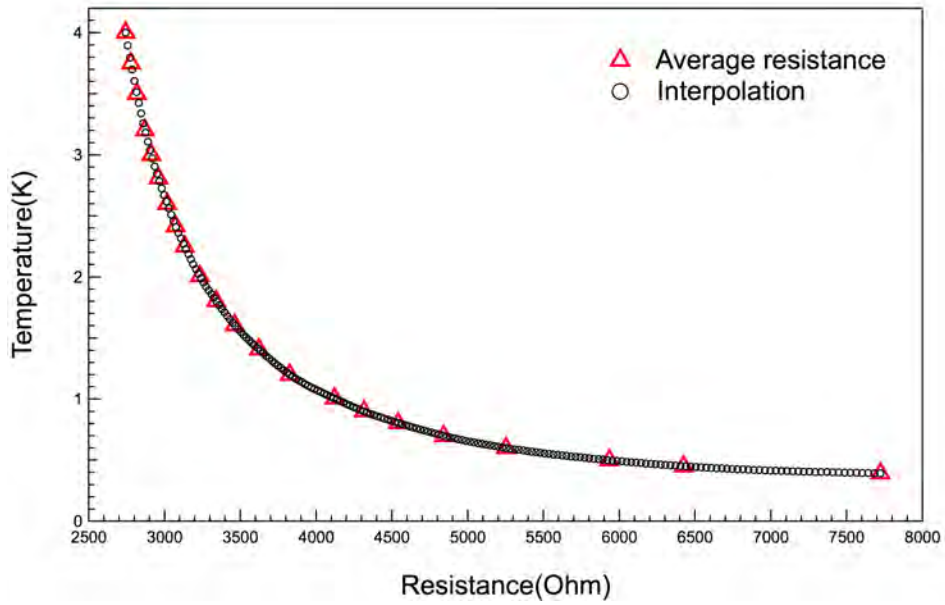

Figure 3.5: Interpolation of data points were generated to fill up gaps between averages of sensors' resistance at various temperatures.

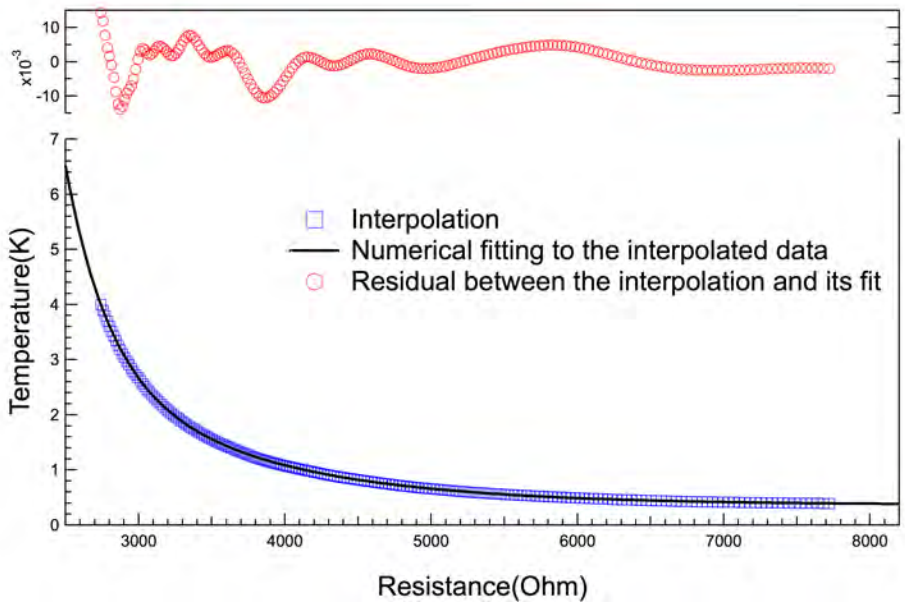

Figure 3.6: A curve fitting (black) superimposed on the interpolation (blue squares) and the residual (red circles) to show their agreement.

3.2 Zero-field measurement

All our zero-field measurements were carried out on $^{\mathrm{DRY}}\mathrm{ICE}^{\mathrm{4TL}}$ System (lemon fridge), which allowed us to go below 400 mK. The first measurement was conducted on a 56.7 nm film of pure aluminum that was thermally deposited onto a SiO_2 quartz substrate with the e-gun/thermal deposition system described in chapter 2. The sample was first cooled down to below 0.9 K, and then slowly warmed up to well above its transition temperature. Meanwhile, the temperature and resistance of the sample was recorded by a computer through Lakeshore®370 AC resistance bridge and Cryocon®44C temperature controller. The raw measurement is plotted and presented in figure 3.7.

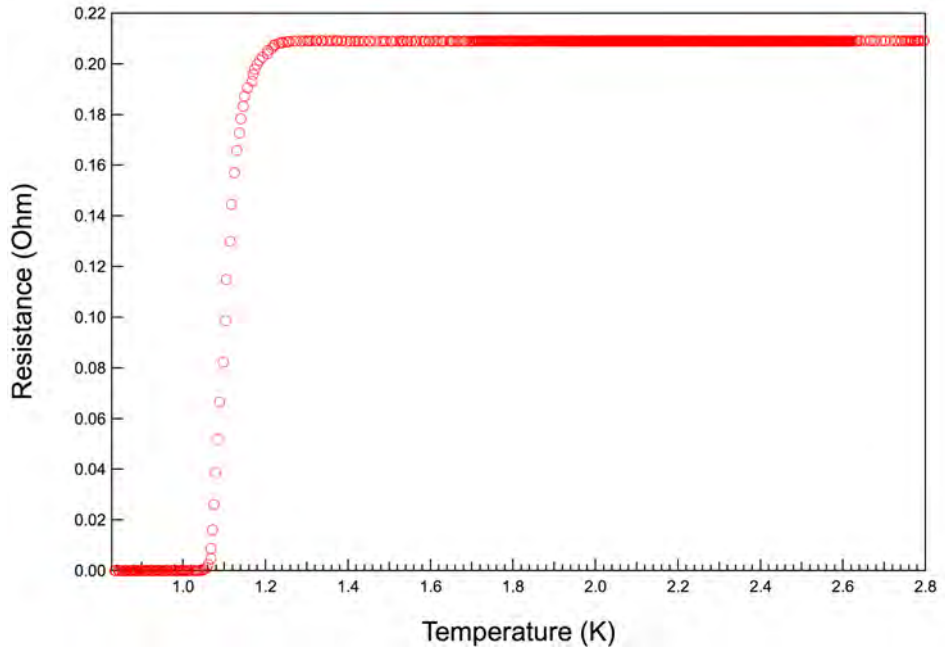

Figure 3.7: The raw data of resistance measurement of thermally deposited pure aluminum film of 56.7 nm thick.

The next step was to pinpoint the transition temperature. In order to do so, it was necessary to find out the normal resistance of the sample, thus an average value of the flat part of the plot was obtained from a histogram (see figure 3.8(a)) of values of the same part of the curve. Using this average value of normal resistance, we found the half "height" of the plot since, by convention, the temperature at which the sample resistance drops to half the value of its normal resistance is considered the superconducting transition temperature. As there was only a handful of data points in the part of the curve where a dramatic resistance drop occurred, the chance of getting one exactly located at the "half height" was next to zero. Therefore, a linear fitting on this part of the curve tackles this problem by providing essentially a continuous line at this range of data that allows us to derive a value exactly at the "half height." The fitting function used was a typical linear function: $R = a + b \cdot T$, where R stands for resistance, T stands for temperature, and a and b are just fitting parameters. The result is found in figure 3.8(b).

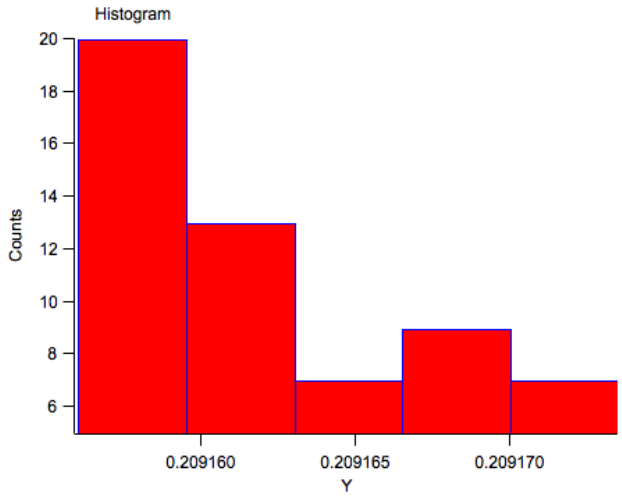

(a) The histogram used to determine an average value of the resistance of pure aluminum film (56.7 nm) well above transition temperature.

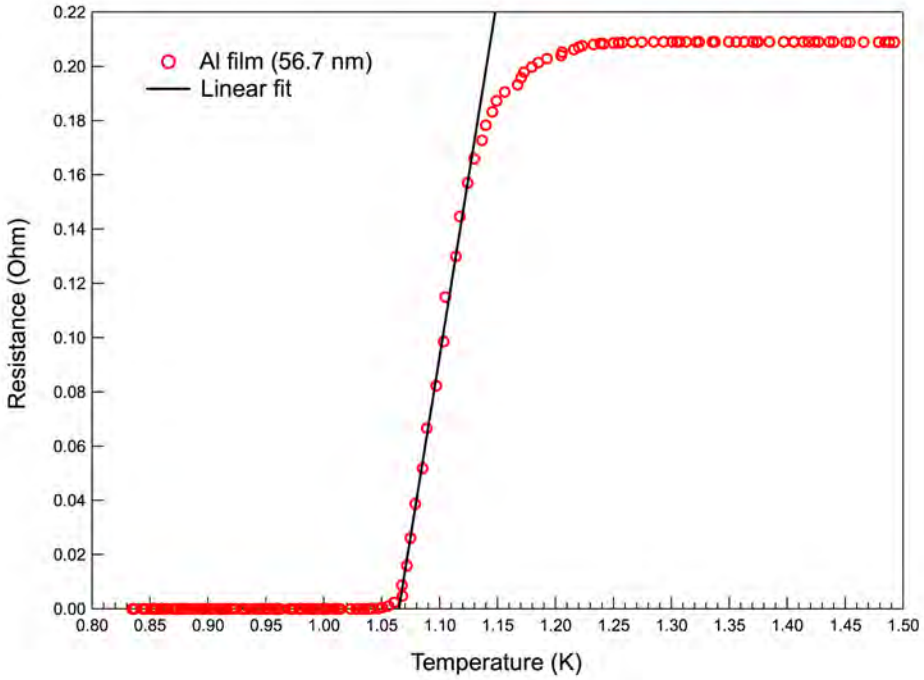

(b) The linear fit of the transition part of the resistance plot of pure aluminum film (56.7 nm).

Figure 3.8: Raw data from zero-field resistance measurement of pure aluminum film (56.7 nm) is processed to deduce its transition temperature.

By rearranging the fitting function, we obtained ($R = a + b \cdot T$), and arrived

at $T_c = \frac{R_{\text{half}} - a}{b}$, which gave $T_c = 1.108$ K. Error analysis was also carried out:

$$\delta T_c = \delta \left(\frac{R_{\text{half}} - a}{b} \right) = |T_c| \cdot \left(\frac{\delta R_{\text{half}} + \delta a}{|R_{\text{half}} + a|} + \frac{\delta b}{|b|} \right) \tag{3.2}$$

Eventually, we got $T_c = 1.108 \pm 0.123$ K. This agrees with the accepted value for bulk aluminum within tolerance (1.196 ± 0.005 K [16]) but is still off from the "centre" of it. The reason could be the size and geometry of our sample since the thickness (56.7 nm) was smaller than the coherence length of bulk aluminum ($\xi \sim 1600$ nm) and comparable to the bulk value of penetration depth ($\lambda \sim 16$ nm). But this could also be caused by a bad thermalization. Therefore, in case of the later possibility, we then repeated the same resistance measurement on the same sample but with temperature ramped up and down for several times at a consistent rate that was also used in the first measurement. If there exists a bad thermalization, then a hysteresis loop should appear in the result between the curves when ramping temperature up and that when ramping down. The result is plotted in figure 3.9, from which, although we indeed see a sign of broadening of the part of the curve where resistance drops sharply, the subsequent measurement of the transition temperature agreed with our previous measurement within error.

With this measurement method established, the last step is to derive the temperature dependence of resistivity (ρ) from that of resistance (R) we obtained directly from experiment. Following the method described in chapter 2, applying the following conversion equation:

$$\rho = \frac{\pi \delta R}{\ln 2} \cdot F(d, s) \tag{3.3}$$

where $F(d, s)$ is again the geometric correction factor. For our sample, the four pins are arranged at corners of a square of a side length $s = 10.77 \pm 1.00$ mm, the diameter (d) of the film is $3/4'' \sim 19.05 \pm 0.25$ mm. Together they give a ratio $d/s \sim 1.7688$. From the tabulated correction factors in [27], a fitting curve is generated as seen in figure 3.10, in which the red markers are values tabulated in [27], and the black curve is the fitting using the following function:

$$F(d, s) = y_0 + A \cdot exp\left(-[\frac{\ln(\frac{d}{s \cdot x_0})}{\text{width}}]^2 \right). \tag{3.4}$$

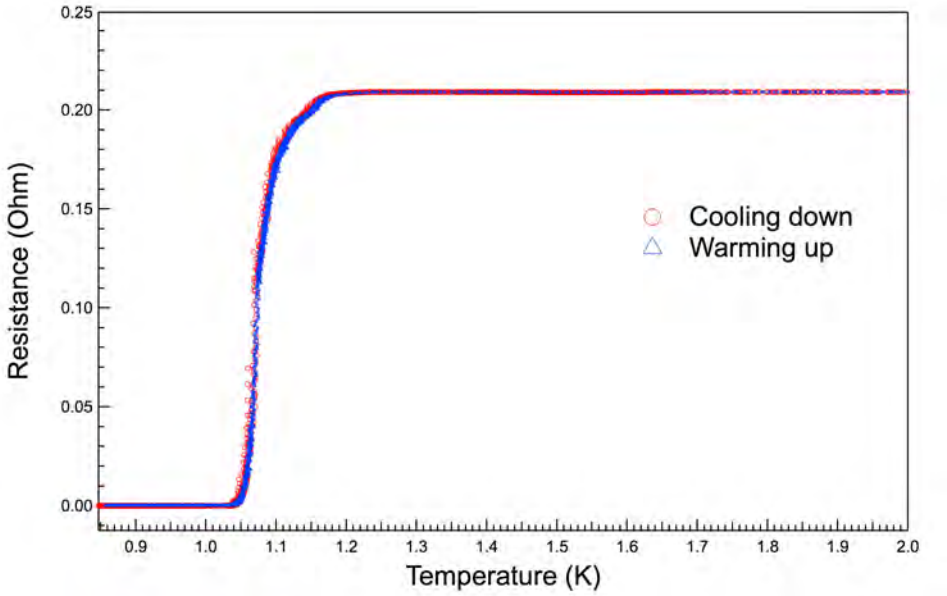

Figure 3.9: Resistance measurement of the pure aluminum film (56.7 nm) were taken for multiple times continuously to verify a satisfying thermalization was achieved. As seen in the figure, though a broadening of the superconducting transition occurred, there isn't noticeable discrepancy between measurements taken when warming up the sample and that when cooling it down.

This function takes the form of an exponential function as suggested in [27], values of the parameters (y_0, A, x_0, width) for this function were computed and displayed in the text box in figure 3.10. Plugged in the ratio, $d/s = 1.7688$, we then got the correction factor for our sample:

$$F(19.05, 10.77) \sim 1.040568 \tag{3.5}$$

Finally, knowing the thickness of the film (56.7 nm) allows us to convert our raw measurement of resistance into that of resistivity as is plotted in figure 3.11. With this method established, we were then able to take zero-field resistivity measurements on Al-Ge films of different metal concentrations, the results are presented in figure 3.12, the legend of which also shows the volumic metal concentration of each sample. Moreover, in table 3.2, the enhancement of the transition temperatures in our Al-Ge granular superconductors are listed along with their volume metal concentrations, and ratios between the transition temperatures and that for bulk pure aluminum. Due to the limiting number of samples measured by the time this dissertation is composed, it is difficult to

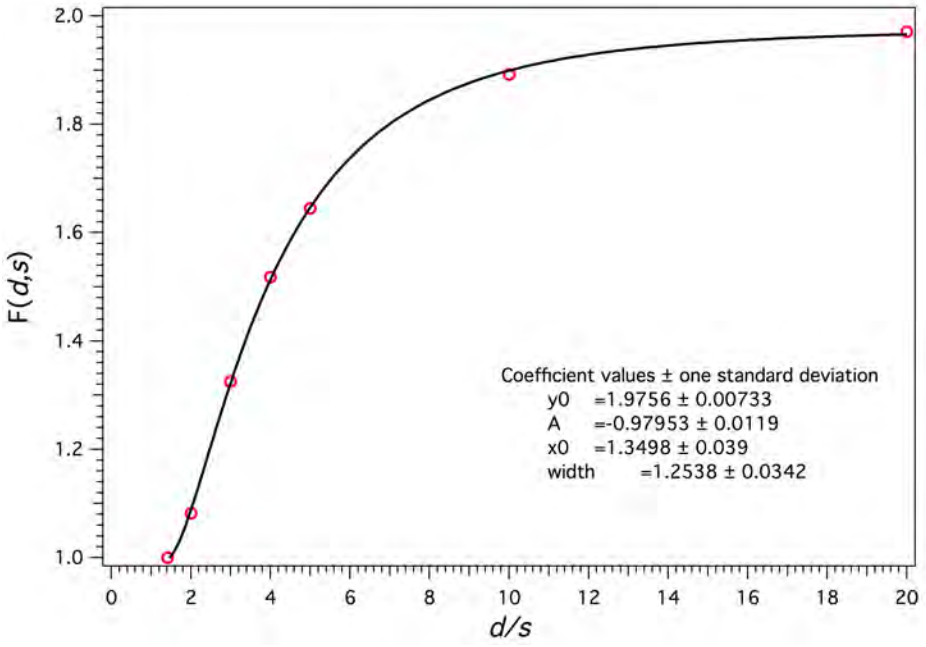

Figure 3.10: A numerical fit to the correction factors to the resistivity measurement of different ratios between the diameter of the film and the probes' spacing. "y0", "A", "x0", and "width" in the figure corresponds to y_0, A, x_0, and width in eqn. 3.4.

generalize a trend to correlate the metal concentration to the superconducting transition temperature.

Before we continue, a side note is necessary here about the metal concentration we obtained for our sample. The volume metal concentration of aluminum in our Al-Ge samples were calculated based on the mass and atomic concentrations of aluminum measured by x-ray photoelectron spectroscopy (XPS). The x-ray beam used for the measurement is typically of 1 mm in diameter, and

Sample ID	Vol. Al Conc.	T_c	T_c/T_{c0}
083113	66.1%	1.95 K	1.625
090613	65.1%	1.78 K	1.48
101013	66.1%	1.73 K	1.44

Table 3.2: A list of the superconducting transition temperatures of Al-Ge samples we made and measured by far. T_c stands for the transition temperatures of Al-Ge samples, and T_{c0} means that for pure aluminum (bulk value).

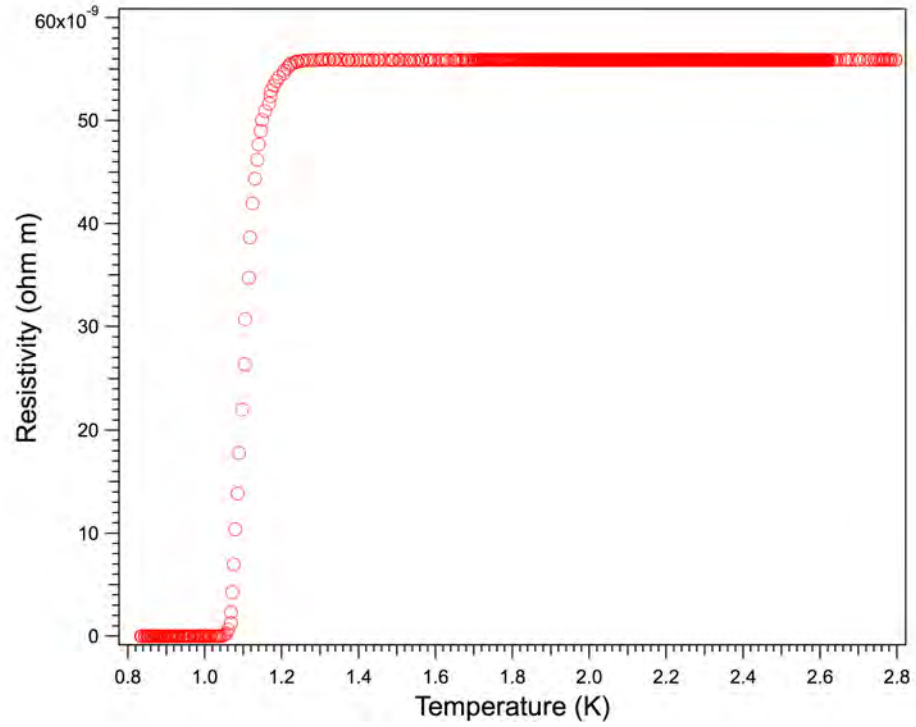

Figure 3.11: Resistivity measurement of pure Al film (56.7 nm) on SiO_2 quartz substrate.

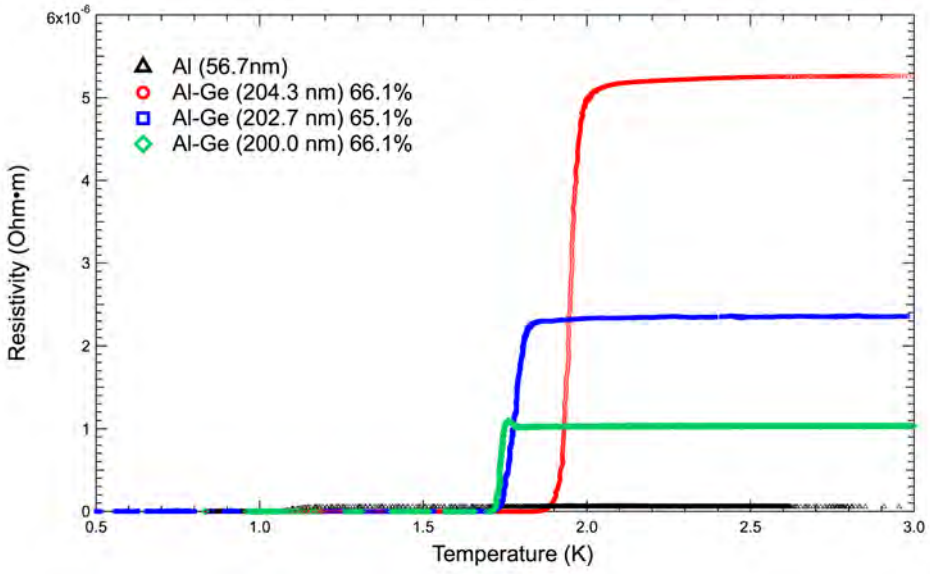

Figure 3.12: Resistivity measurements of aluminum-Germanium granular films of different volumic metal concentrations measured by X-ray photoelectron spectroscopy (XPS) measurement, which are given in the legend.

the sampling area on the surface of the sample is about 300×700 μm^2, while the entire area of the sample is of ~ 285 mm^2. It is risky to use this statistical data from the sampling area to represent that for the whole film, which is of more than 1300 times larger than it. Moreover, the accuracy of the XPS measurement is described by its reproducibility and absolute accuracy together. In terms of its reproducibility, the uncertainty in the percentage concentration measured is about 0.1%. While its absolute accuracy, meaning the maximum discrepancy between two identical measurements done by different XPS machines, is about 10% of the reading. This adds more difficulties in determining the true metal concentrations of the samples. Therefore, all the values of aluminum concentration labeled for our samples are better treated as indications rather than being taken too seriously.

Now back to the zero-field resistivity measurements of aluminum germanium samples. If one takes a close look at them, and compares the resistivity curve of sample 083113 to that of sample 101013, it appears that even though both samples seem to have identical metal concentrations, the behaviours of the resistivities at low temperature differ greatly. Specifically, an increase in sample 101013's resistivity near superconducting transition can be noticed, while not in the curve for sample 083113. Thanks to Prof. J. Beamish's insight, we were able to attribute this small increase in resistivity right before the superconducting transitions in some of our samples to the inhomogeneity of these samples. The reason behind this phenomenon is described as follows:

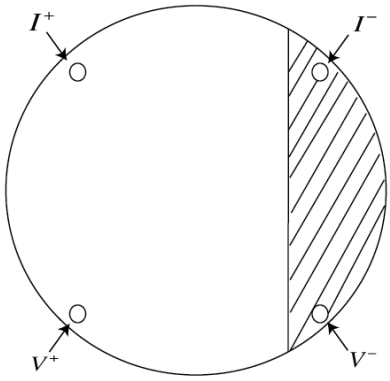

(a) A standard square-four-probe measurement on a circular shaped sample with the shaded area goes superconducting slightly earlier than the rest part. The region covers the area where both the current and voltage drains are placed, thus brings down the electric potential of the voltage drain and increases the voltage across the voltage pins.

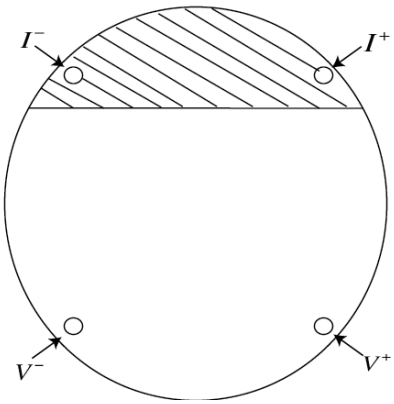

(b) A standard square-four-probe measurement on a circular shaped sample with the shaded area goes superconducting slightly earlier than the rest part. The region covers the area where the two current pins are placed, thus the current flows through this electrical short between the two pins, causing the electrical potential between the voltage pins essentially zero.

Figure 3.13: Square-four-probe measurement on circular shaped inhomogeneous sample.

Consider the square-four-probe measurement on a circular shaped film sample as in figure 2.13. If the film is homogeneous, then the whole sample will go superconducting at the same time. But when the film is inhomogeneous, then it is possible for part of the sample to become superconducting at a slightly higher temperature then the rest. If this part of the sample happens to be the region with which a current pin and a voltage pin are in contact (see figure 3.13(a)), the subsequent redistribution of the electrical field within the film will bring the electrical potential of the voltage probe up or down, depending on whether that probe is a source or a drain,. Either way, it results in an increase in the voltage across the pins and thus in the resistance readings. This explains the small "horns" that appeared in the zero-field resistivity measurements in some of our samples. To expand on this, we can further imagine another scenario when this region of higher superconducting temperature covers the area where both

the current pins are placed but none of the voltages pins (see figure 3.13(b)). Then the current will flow through this electrical short when the region goes superconducting, and leave the rest part of the sample at the same electrical potential. In this scenario, the voltage measured will be zero, which indicates a zero resistance. In experiments, this may in the end give a slightly higher superconducting transition temperature than that of the most part of the sample.

Given the various deformations (including the two examples above) of the zero-field resistivity measurement due to the inhomogeneity of the sample, two further steps already became obvious by now. The first one it that we need to improve the deposition techniques in order to have samples that are more homogeneous. The secondly one is that, by Prof. J. Beamish's advice, we should rearrange the four probes during measurements for better configurations to eliminate, or minimize at least, the influence from the inhomogeneity of the samples on our measurements.

3.3 Field sweep measurement

As we have already realized, the information conveyed by zero-field resistivity measurement was very limited. It was just the first step of a long journey! In order to learn more about the system, we then carried out resistivity measurement at not only varying temperature but also in changing magnetic field. The scheme of the measurement was described in chapter 2 and presented again here broken down into the following steps:

- Cool down the sample to the fridge's base temperature and stabilize at that temperature.
- Sweep the magnetic field, at a preset rate, up to a target value, record to a file the sample's resistance at the same time.
- Sweep the magnetic field back down to zero, record the sample's resistance to a different file from the previous step.
- Change the temperature by one step (0.025 K) and stabilize it at the new value. Then repeat the previous two steps (sweeping the magnetic field up and down).
- When the temperature reaches the preset upper limit, stop sweeping field, and finish the measurement.

The data acquired from this measurement thus can be plotted in a 3 dimensional graph as it has three degrees of freedom (temperature, magnetic field, and resistance). Take the 56.7 nm-thick-film of pure aluminum from the previous section for example again, the raw data from the measurement of it is shown in figure 3.14, and naturally, this raw data was processed and converted into resistivity, which is intrinsic to the material, as a function of temperature and magnetic field and is presented in figure 3.15.

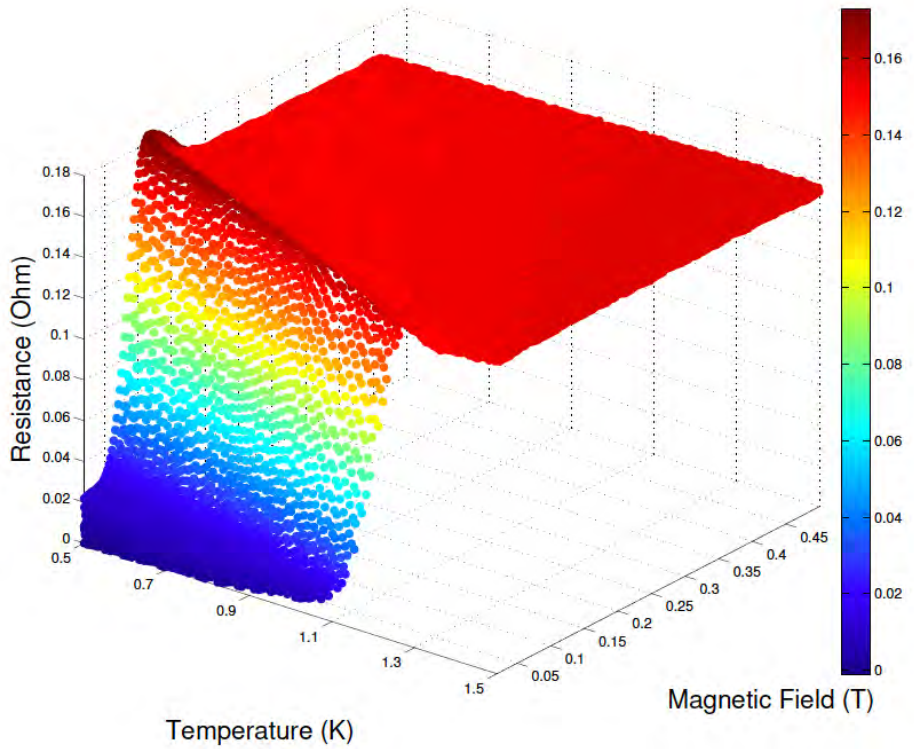

Figure 3.14: Raw data of resistance measurement at various temperatures and magnetic fields of pure Al film (56.7 nm)

In fact, this "map" of the resistivity of aluminum as a function of magnetic field and temperature contains a lot more information now. Looking at the resistivity map from different angles would provide different information about the sample. This can be seen in figure 3.15, as its top view (figure 3.15(b)) gives a general shape of $H_c(T)$ of aluminum, the front view (figure 3.15(c)) shows the landscape of the resistivity near superconducting transition. furthermore, the side view (figure 3.15(d)) recovers the shape of its zero-magnetic field resistivity.

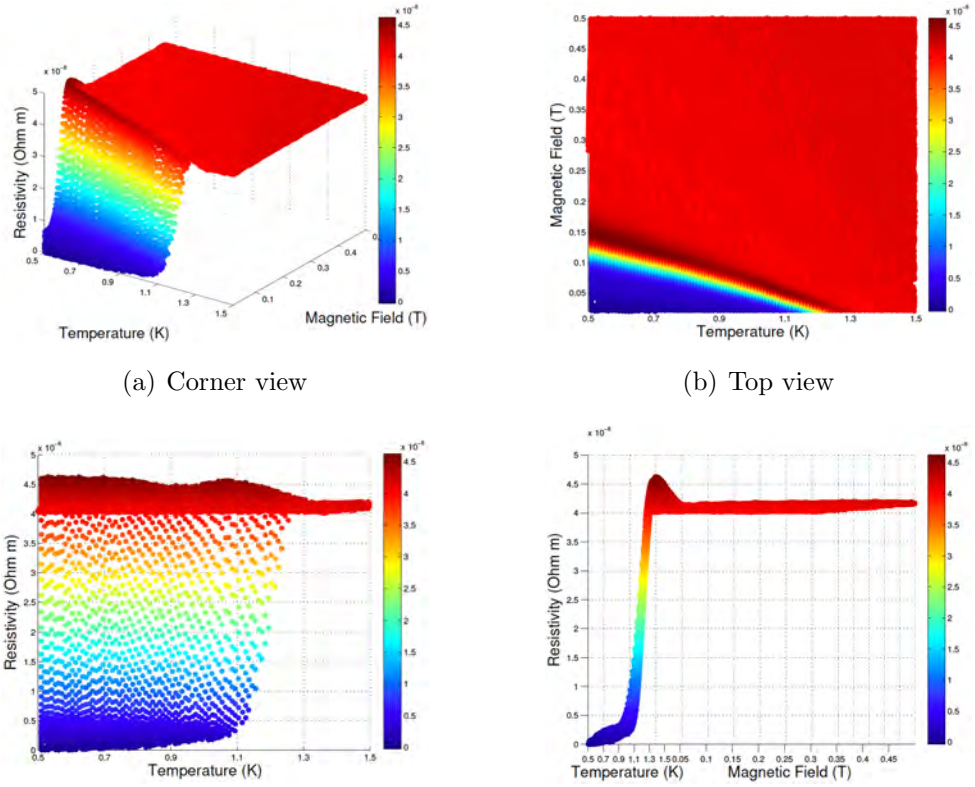

(a) Corner view

(b) Top view

(c) Front view

(d) Side view

Figure 3.15: Resistivity of pure aluminum film (56.7 nm) as a function of temperature and magnetic field derived from resistance measurement.

Following the same steps and processing procedures, the same maps for Al-Ge granular films of different metal concentration are also produced (see figure 3.16). In these figures, zero-field resistivity measurement were plotted (black curves from the corner views of figure 3.16) together with field sweep measurements. The agreement between them indicates the condition of thermalization of the sample cell as, when taking zero-field resistivity measurement, the temperature of the sample is changed continuously and constantly, while during field sweep measurement, the temperature is held at one specific value before moving onto the next when the field is ramped up and down. Thus the samples usually sit at one temperature for a minute or so during zero-field measurement but for about an hour during field sweep measurement, and agreements in the superconducting transition point therefore validate the assumption that the temperature change in zero-field measurement was slow enough that the temperatures read by the thermometer truthfully reflect that of the samples.

What else is worth noticing is that in the measurement of sample 090613 (figure 3.16(c) and figure 3.16(d)), the upturn appeared very close to the transition temperature that is only visible after zoomed in at the region (see figure 3.17), which was why we didn't even notice it at the beginning until we compared the superconducting transition temperatures from zero-field measurement and field sweep measurement. This feature has never been seen in any of the previous literatures we found, thus in the hope of that it may shed new light on granular superconductivity, we are arduously working on understanding it.

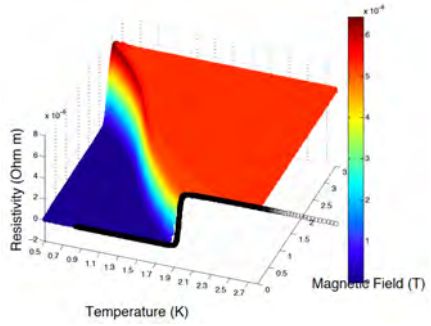

(a) Sample Al-Ge (083113), Al Vol. Conc.: 66.11%

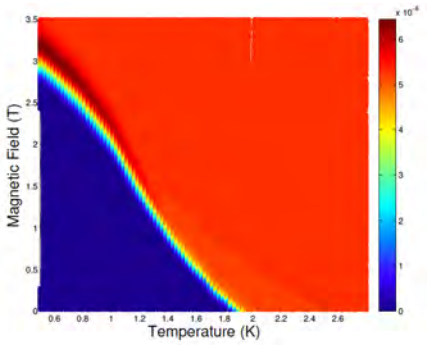

(b) Sample Al-Ge (083113), Al Vol. Conc.: 66.11%

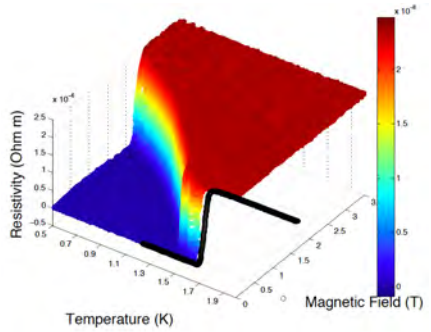

(c) Sample Al-Ge (090613), Al Vol. Conc.: 65.14%

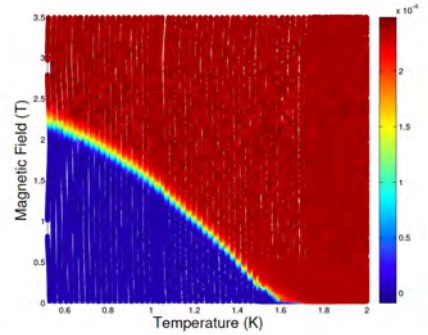

(d) Sample Al-Ge (090613), Al Vol. Conc.: 65.14%

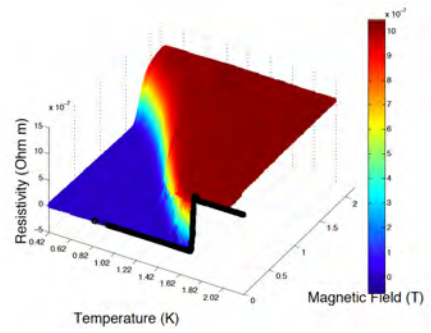

(e) Sample Al-Ge (101013), Al Vol. Conc.: 66.10%

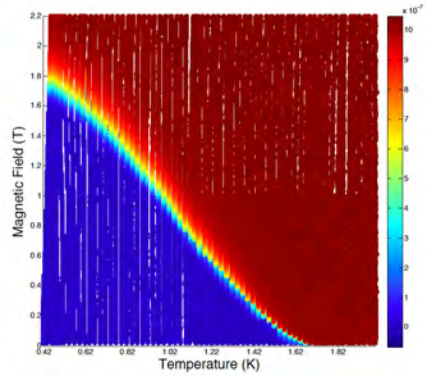

(f) Sample Al-Ge (101013), Al Vol. Conc.: 66.10%

Figure 3.16: Experimental data of resistivity as functions of temperature and magnetic field of Al-Ge films at different metal concentration. The black curves in the corner views of the measurements indicates the zero-field resistivity measurement. The data was plotted directly from raw data without interpolation or smoothing, which accounts for the occasional white spaces between sets of measurements.

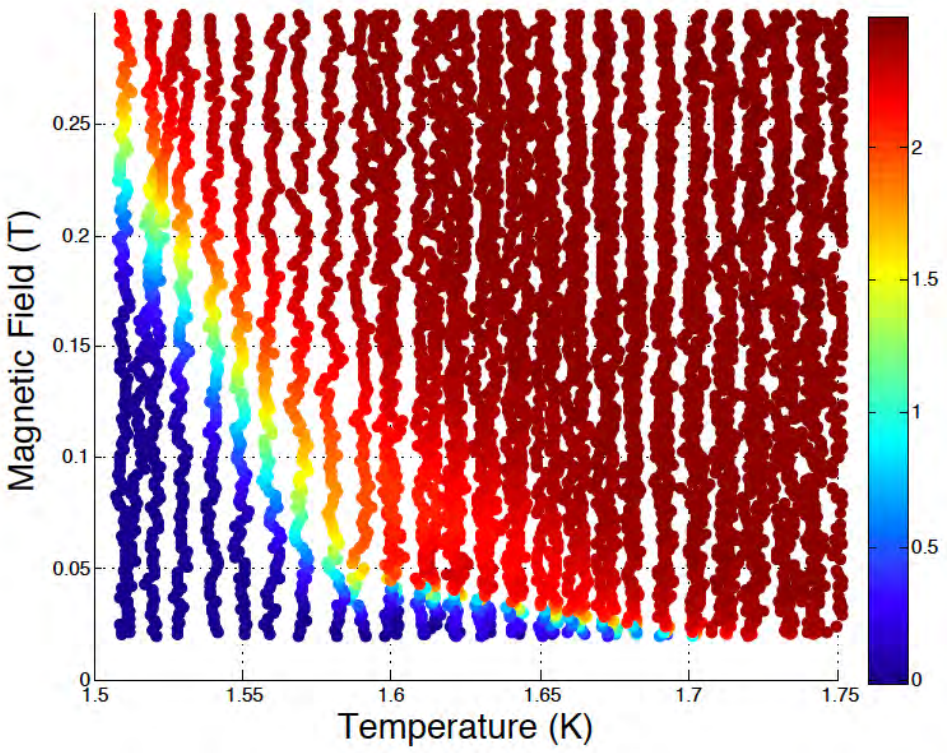

Figure 3.17: A zoomed in top view of resistivity measurement of sample 090613 at various temperatures and magnetic fields. The sudden change of curvature near the transition temperature may give hints of the superconductivity mechanism in granular superconductors.

3.3.1 Data process

With the phase diagram plotted, the natural next step was to extract the upper critical field curves for all the samples. The process is exemplified here with one of the samples. To begin with, the transition part of the phase diagram was isolated from the rest (see figure 3.18(a) and figure 3.18(b)). A linear fit to this transition part similar to the one performed in figure 3.8(b) along the magnetic field dimension was obtained at every temperature point (see figure 3.18(c)). This is linear fit to the transition part of the plot allowed us to pinpoint the points on these transition curves where the resistivity of the sample drops to half of its normal resistivity, which was acquired by averaging over the resistivity in the normal region (red parts in the phase diagrams in figure 3.16). Eventually, these points were taken out to form the curves of upper critical field of the sample. Repeating the same process for every sample, we yielded such curves for all the samples, which are plotted in figure 3.19.

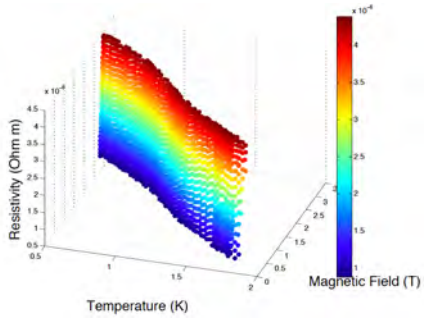

(a) The transition part of a phase diagram of an Al-Ge granular superconductor was isolated out for linear fitting.

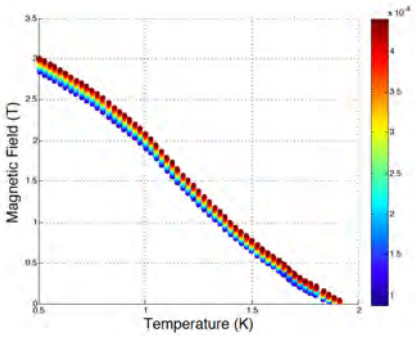

(b) The top view of the transition part of a phase diagram of an Al-Ge granular superconductor being isolated.

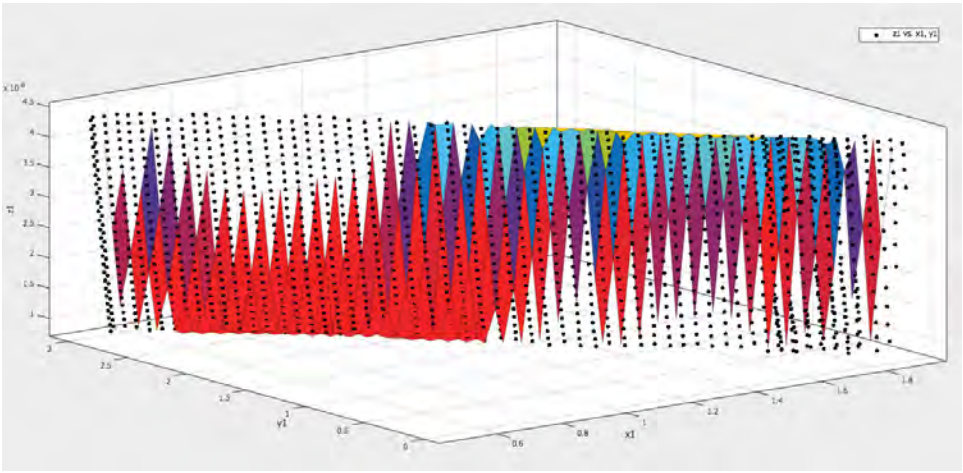

(c) Linear fit to the transition part of a phase of an Al-Ge granular superconductor diagram at each temperature point.

Figure 3.18: Transition part of a phase diagram was isolated for further process to extract upper critical field curves.

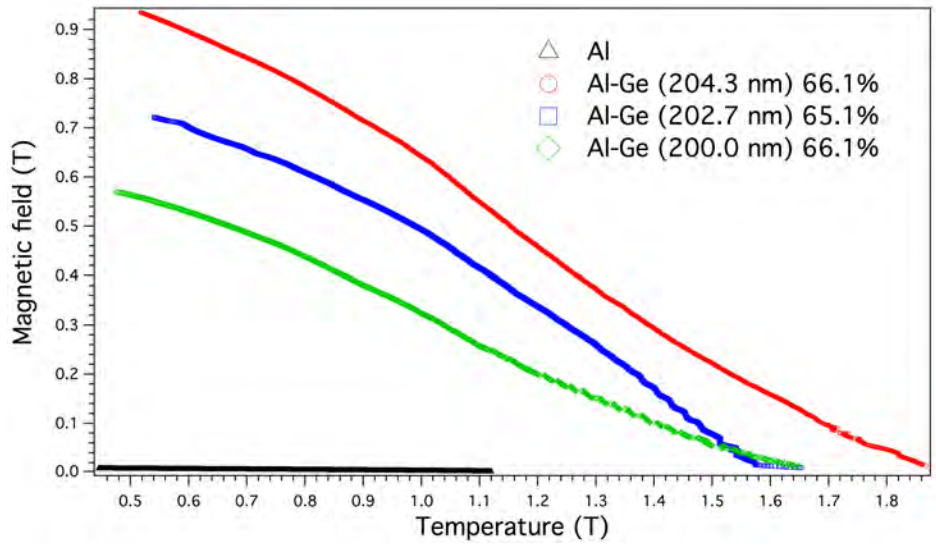

Figure 3.19: The upper critical field curves for all the Al and Al-Ge film samples.

So far we've been paying attention only to the temperature dimension and resistivity dimension, it is of course that we need some treatment, or justification, for the magnetic component before we can actually use it. We shall begin with considerations of the actual local magnetic field applied to the sample. As mentioned before in chapter 2, the ^{3}He dipper fridge came with a built-in 9 T superconducting coil. From the specification of the magnet, we find that the overall length of the field is 281 mm, which is fairly short considering the size of the fridge itself. According to elementary electromagnetism, the magnetic field applied by a tightly wound circular coil of finite length has its maximum along the solenoid's axial line and half way between the two ends of the magnet. For the local field away from the maximum point, the magnetic field decays very fast (see figure 3.20), and the computation of which can be complicated due to the surroundings' increasing influence on the distribution of magnetic flux lines.

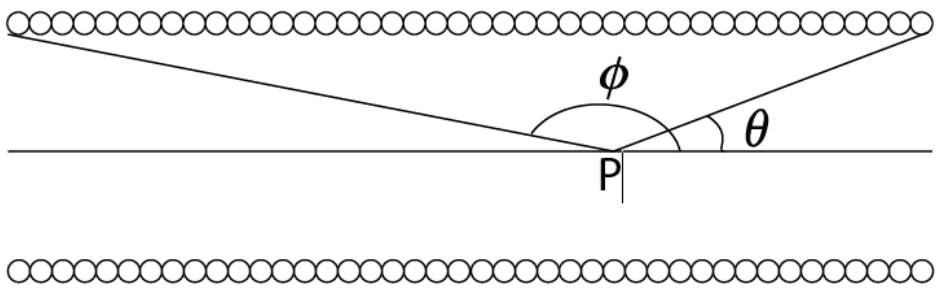

Figure 3.20: A schematic drawing of the side view of a solenoid, the central line is the axial line of the solenoid. For a tightly wounded solenoid, the local magnetic field (B_P) generated at the point "P" in the figure is given as $B_P = \frac{\mu_0 nI}{2}(\cos\phi - \cos\theta)$, where μ_0 is the permeability of free space, n is the linear density of the coil, and I is the current that runs through the solenoid.

In practice, the situation was worsened by the fact that the middle point between the two ends of the solenoid wasn't labeled on the fridge, thus we couldn't measure to tell the exact position of our samples in terms of their distances from the two ends of the solenoid. Moreover, the strength of the field returned by model 430 power supply programmer was not measured but rather calculated from real-time measurement of the current in the coil and was based on the theoretical relation between the maximum of the magnetic field and the current. Thus, just by reading values off from model 430 power supply programmer is far from enough to tell the actual magnetic field applied to the sample.

In order to tackle this technical issue, we modified our design of the sample cell so that it can accommodate a hall probe (see figure 3.21(a)) only millimetres away from the sample (see figure 3.21(b)). This modification allows us not only to measure the actual local magnetic field in the future, but also to correct the existing data prior to us obtaining this Hall probe because of that all the samples were kept at the sample position during measurements. Plus that the setup, which is here essentially the environment, has never been changed, we can safely assume that the magnetic field has been applied to every sample was identical, and therefore the correction would also be applicable to all previous samples.

(a) The LHGA-321 hall probe used in our experiments, manufactured by Lakeshore®, can take measurement of magnetic field at a large temperature range between 1.5 K to 370 K.

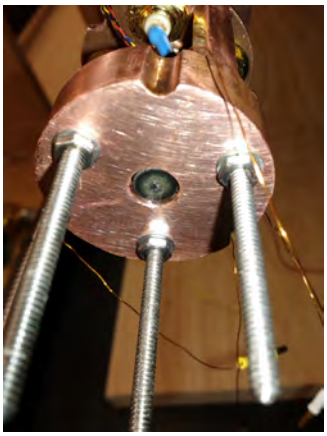

(b) A photo of the front view of the sample bed of the sample cell. The small niche was made in the centre, and a hall probe is installed inside. During experiments, the sample film will lay on top of the probe only few millimetres above.

Figure 3.21

However, just acquiring the values of the local magnetic field near the samples is not enough, because this field isn't entirely the field that the samples actually experience. This point can be illustrated by first to consider a superconductor of thin (flat) ellipsoid shape in a perpendicular magnetic field as in figure 3.22(a).

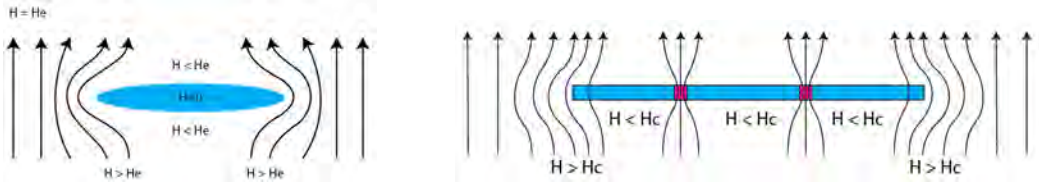

(a) A superconducting ellipsoid in a transverse magnetic field, H is the local field strength, and H_e indicates that of the external field applied.

(b) A schematic illustration of a thin superconducting film in a perpendicular magnetic field.

Figure 3.22: Schematic illustrations of considerations of the distribution of local magnetic field flux.

In figure 3.22(a), we see the magnetic field near the sample is not homogeneous, but rather being "squeezed" in some regions and "stretched" in other. The consequence of this leads the local field near the edges of the sample stronger than the rest, and when the field is just infinitesimally weaker than the critical field of superconductor, while one might expect the material stay superconducting, superconductivity has already been destroyed at the edges of the sample due the stronger local field. The same thing would happen to our film sample, the shape of which can be thought of very thin disk. When the field becomes strong enough near the critical field, the sample will enter an "intermediate" state [28, 4] as illustrated in figure 3.22(b) where some part of the sample becomes normal to allow magnetic field flux to go through to lower system's overall energy. What is worth noting is that this is different from the vortices appearing in type-II superconductors as, on the one hand, the flux through these normal regions are not quantized as they are in fluxoids, and on the other hand, the pattern of domains between normal regions and superconducting regions are fairly irregular as opposed to the Abrikosov vortex lattice in type-II superconductors. As a matter of fact, in real samples even with a regular geometric shape, one still has to determine the actual distribution of normal regions by direct measurement [4].

What makes it worse is that this isn't all. In classical electrodynamics, especially in ferromagnetic materials, when an external field (H_e) is applied to a material, depending on the magnetization (M) of the material, the strength

of the effective magnetic field (H_{eft}) inside is reduced from that of the field applied. The relationship of the three parameters is given as [29]:

$$H_{\text{eff}} = H_e - N \cdot M \tag{3.6}$$

where N is the demagnetization factors. This factor is highly dependent on the geometry of the material. For regularly shaped samples, it is calculable [29], but in reality, for irregularly shaped samples or inhomogenous demagnetization fields [30], it is often very difficult to calculate. Although an effective demagnetizing factor have been calculated for particle mixtures [31] similar to the structure of our granular superconductors, it is very sensitive to the homogeneity of the material, which we are, at this point, uncertain of its applicability to our case.

However, there is good news as well, which is that these two demagnetization factors should have only a minor influence on our samples. This is due to the fact that, to begin with, in the first scenario where magnetic fields penetrate the film and breaks down superconductivity in some irregularly patterned local areas, so long as there are superconducting regions form short circuits among the four probes, a resistance/resistivity measurement of the sample wouldn't be able to tell the difference between this situation and a purely superconducting sample. Consequently, this demagnetization factor wouldn't make a noticable difference even at fairly high field. Furthermore, both the paramagnetism in aluminum and diamagnetism in germanium are weak, meaning that their susceptibilities are very small, and thus their contribution to the demagnetizing effect are also small. Therefore we can safely assume a negligible change of this demagnetization factor from sample to sample of different metal concentrations, and all we need to do is to figure out one correction factor for all our samples.

In practice, this requires us to compare our extracted critical field ($H_c(T)$) curve for an Al film of the same geometry with every other sample to a known one from previous reports, and by shifting our data to agree with the known curve to obtain a demagnetizing factor. This was indeed what we did. After measuring and extracting the critical field curve for a pure aluminum sample of 200 nm thickness, we compared and scaled it down to agree with the exper-

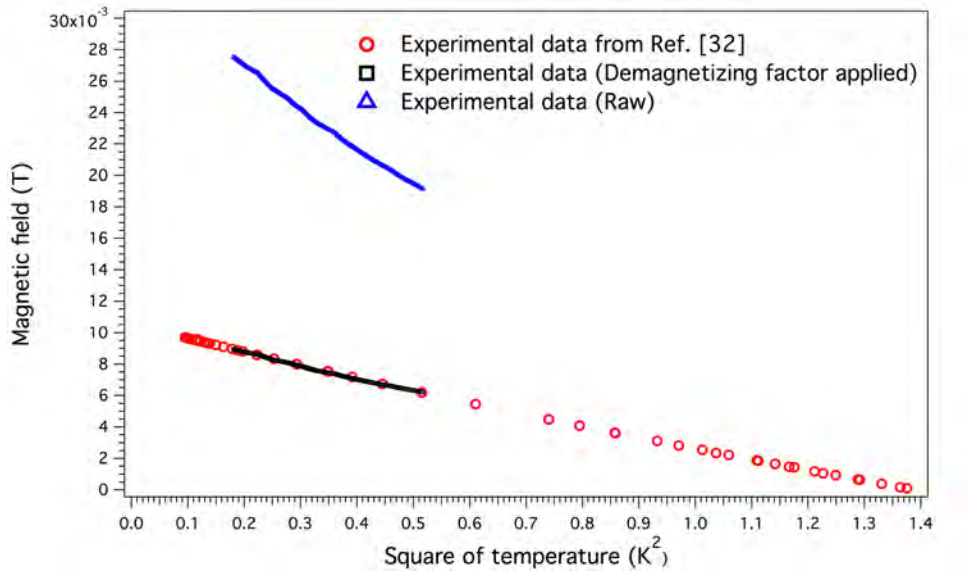

Figure 3.23: Our experiment data (blue triangles) was compared and scaled down (black squares) by an effective demagnetizing factor to agree with data (red circles) from ref. [32].

imental data from ref. [32] (see figure 3.23). The effective demagnetizing factor obtained was 3.0786, and subsequently all the data was scaled down by this factor since their positions in the solenoid during measurements were consistently the same.

3.3.2 Data interpretation

Due to limited time before the end of my program, we weren't able to conduct a thorough characterization of our samples for extensive interpretation of the experimental results. However, attempts were made toward the direction of understanding the physics behind all the observations. To begin with, we were particularly interested in the occurrence of the curvature change in all the upper critical field curves (see figure 3.19). Therefore I made effort to climb up and stand on the "shoulders of the giants" for insights into the problem by following the idea proposed by G. Deustcher, *et al.* in one of his publications in 1980 (ref. [33]).

In this paper, the authors proposed that the behaviours of the upper crit-

ical field curves (H_{c2}) of granular superconductors mainly resulted from the coupling among superconducting grains. At high metal concentrations, superconducting grains are close to each other and thus strongly coupled. At low metal concentrations, the situation is the opposite and the superconducting grains are nearly isolated from each other, hence the system falls into the weak coupling regime. However, between these two cases, there exists an intermediate regime where the system experiences a transition from strong coupling to weak coupling as the temperature goes down. At the temperature where this transition happens, the upper critical field curve will exhibit an upturn (change of curvature). We indeed made observations of such upturns in the upper critical field curves of our samples, but whether or not can we attribute this feature to the coupling strength among grains, it largely depends on the agreement between experimental data and theoretical prediction in a quantitative comparison.

The theoretical treatment of the problem in this paper was to include an extra coupling term in the Ginzburg-Landau equations and, by simplify and expanding in series with various assumptions and approximations, the equation was further transformed into two expressions of the upper critical fields in the strong coupling and weak coupling regimes respectively. Details of the derivation of their mathematical forms can be found in the original paper in ref. [33], thus won't be repeated here. Only the results is given as, in the weak coupling (strong field) regime,

$$H^2 = \left(\frac{\hbar c}{2e}\right)^2 \frac{5}{3}\frac{1}{\xi(T)^2 R^2}\left(1 - 2\frac{\xi(T)^2}{t^2}\right), \tag{3.7}$$

and in the strong coupling (weak field) regime,

$$H = \frac{\hbar c}{2e}\left(\frac{t}{S\xi(T)}\right)^2 \left\{1 + \frac{1}{4}\left(\frac{t}{\xi(T)}\right)^2 \left[\frac{1}{4} - \frac{3}{5}\left(\frac{2tR}{S^2}\right)^2\right]\right\}. \tag{3.8}$$

In both equations, R is the radius of the superconducting grains. S is called the "lattice constant" as it is the sum of the diameter of a superconducting grain ($2R$) and the thickness of the barrier (b). t stands for a coupling length defined as $t = \frac{h}{2m\eta}$, where η is the coupling energy, and thus t is independent of the

temperature, and can be treated as a constant. $\xi(T)$ is the Ginzburg-Landau coherence length of isolated grains, and is the source of the temperature dependence of the upper critical fields as it is given by $\xi(T)^2 = 4\pi^2\xi(0)^2\frac{T_c}{T_c-T}$.

Before we go further to apply these equations to our case, we can gain some insight of these two equations by looking at them in limiting situations. For eqn. 3.7, it is supposed to be responsible for the behaviours of the upper parts of H_{c2} curves, thus at the limiting case when temperature goes to zero, eqn. 3.7 should give us the zero-temperature upper critical field of the system. Plugging in some values of the variables, we have

$$H_{c2}(0)^2 = 1.809 \times 10^{-15} \cdot \frac{1}{R^2} \cdot \left(\frac{1}{4\pi^2\xi(0)^2} - \frac{2}{t^2} \right), \tag{3.9}$$

Recalling that $\xi(0) \propto T_c^{-1}$ [4], the coherence length at zero temperature for the granular system can be estimated by multiplying the zero-temperature coherence length of pure aluminum by the ratio of its superconducting transition temperature to that of the sample's. This in the case of sample 083113 yields 1010 nm, or 1.01×10^{-6} m. Now, the tricky part is to find a value for the coupling energy (t). In the original paper of Deutscher's, by considering the Josephson energy and applying Drude model to it. The coupling lengths was expressed as

$$\frac{1}{t^2} = \frac{1}{4S^2\sigma\rho_n}, \tag{3.10}$$

where S is again the sum of the diameter of a superconducting grain (2R) and the barrier thickness (b), σ is the conductivity of bulk aluminum, and ρ_n is the normal resistivity of the sample. Except for the conductivity of bulk aluminum, which at low temperature is constant (10^{12} S/m at ~ 1 K [34]), in the calculations all the rest are characteristic features belong to each individual sample. Thus the calculation of these coefficients should be treated case by case, and we arrive at the simplest form of eqn. 3.7 at zero temperature for general cases:

$$H_{c2}(0)^2 = 1.809 \times 10^{-15} \cdot \frac{1}{R^2} \cdot \left(\frac{1}{4\pi^2\xi(0)^2} - \frac{5 \times 10^{-24}}{(2R+b)^2\rho_n} \right), \tag{3.11}$$

and at finite temperature

$$H_{c2}(T)^2 = 1.809 \times 10^{-15} \cdot \frac{1}{R^2} \cdot \left(\frac{1}{4\pi^2 \xi(0)^2} \cdot \frac{T_c - T}{T_c} - \frac{5 \times 10^{-24}}{(2R+b)^2 \rho_n} \right). \quad (3.12)$$

If we plug the numbers in eqn. 3.11 at zero temperature for sample 083113, we get

$$H_{c2}(0)^2 = \frac{4.49 \times 10^{-9}}{R^2} - \frac{1.71 \times 10^{-22}}{R^2(2R+b)^2}. \quad (3.13)$$

We can't solve for "R" and "b" as we only have one equation but two unknown variables. So we can set it aside for now and take a look at eqn. 3.8, which dictates the lower parts of the H_{c2} curves. We shall examine this equation near the transition temperature ($T \sim T_c$). To begin with, we again plug in all the number we know to get

$$H_{c2}(T) = 1.32 \times 10^{-6} \cdot \frac{\rho_n}{\xi(T)^2} [1 + \frac{40\rho_n}{\xi(T)^2} (\frac{S^2}{16} - 24\rho_n R^2)]. \quad (3.14)$$

This will be the general equation for granular superconductors in weak field and strong coupling regime. Considering in the present case, we are dealing weak field but strong coupling scenario, the granular superconducting system can be regarded as in the dirty limit. Thus near the vicinity of the superconducting transition temperature, we have the following temperature dependence of the coherence length [5, 33]:

$$\xi(T) = 0.86 \left(\xi_0 l \frac{T_c}{T_c - T} \right)^{1/2}, \quad (3.15)$$

where ξ_0 is the Pippard's coherence length, which is essentially temperature independent in contrast to $\xi(T)$. Since at temperatures well below T_c, $\xi(T) \sim \xi_0$, from now on I will approximate the Pippard's coherence length, ξ_0, with $\xi(0)$. In addition to the coherence length, l in the equation denotes the electronic mean free path, which, in the original paper of Deutscher's, was approximated by the average radius (R) of the superconducting grains in the granular system

[33]. Therefore, eqn. 3.8 is further reduced to

$$\begin{aligned} H_{c2}(T) =& 1.78 \times 10^{-6} \cdot \frac{\rho_n}{\xi(0)R} \cdot \frac{T_c - T}{T_c} \cdot \\ & [1 + \frac{54.1}{\xi(0)R}\rho_n \cdot \frac{T_c - T}{T_c} \left(\frac{S^2}{16} - 24(\rho_n R^2) \right)], \end{aligned} \tag{3.16}$$

Now for the limiting case, of course we can't test the equation by making $T = T_c$ as it will vanish. But at a temperature very close to the transition temperature, $0.9T_c$ for example, we have

$$H_{c2}(0.9T_c) = 1.78 \times 10^{-7} \cdot \frac{\rho_n}{\xi(0)R} \cdot [1 + \frac{5.41}{\xi(0)R}\rho_n \cdot \left(\frac{S^2}{16} - 24(\rho_n R^2) \right)] \tag{3.17}$$

Plugging in numbers we know of from sample 083113, we get

$$H_{c2}(0.9T_c) = 1.64 \times 10^{12} \frac{(2R + b)^2}{R^2} + \frac{930}{R} - 3.34 \times 10^{20} \tag{3.18}$$

Now we have two equations of two unknown variables, we can try to solve for them and have an estimation of the applicability to our samples. From figure 3.19, we obtain rough values of $H_{c2}(0)$ and $H_{c2}(0.9T_c)$ as 0.95 T and 0.1296 T respectively. Plugging in these numbers and solving the coupled equations (eqn. 3.13 and eqn. 3.18) for solutions of the average radius of superconducting grains and the thickness of the insulating barriers among them. There exists four solutions, two of them are negative and thus abandoned, the other two positive solutions for R are 1.367×10^{-11} cm and 6.87×10^{-7} cm respectively. Apparently the second solution bears more physical sense. Thus we obtain $R \sim 6.87$ nm or $R \sim 6.87 \times 10^{-9}$ m, and subsequently the solution b = 38.4 nm or 3.84×10^{-6} cm.

Though the values we found above for the average radius of superconducting grains and average thickness of insulating barriers appeared a bit of unrealistic, it is difficult to prove or dispute them without TEM images. Furthermore, I decided to continue to fit one of upper critical field curves (sample 083113) using the coherence length, average radius of the superconducting grains, and the size of the insulating barriers as fitting parameters. For the upper part of the H_{c2} curve, in order to simplify the fitting function, eqn. 3.12 was rearranged into its

linear form by substituting $\frac{T_c-T}{T_c}$ for x as the independent variable, H^2 as the dependent variable (y). Furthermore, the numerous constants are regrouped to make the appearance of the equation cleaner:

$$y = \frac{1}{R^2} \cdot \left(\frac{4.58 \times 10^{-17}}{\xi(0)^2} \cdot x - \frac{9.47 \times 10^{-30}}{(2R+b)^2} \right). \tag{3.19}$$

This is clearly a linear equation now with three fitting parameters. Then, similarly, I simplified the other equation (eqn. 3.16) and arrived at:

$$H(T) = (\frac{S^2}{16} - 1.27 \times 10^7 \cdot R^2) \frac{9412.01}{\xi(0)^4} \cdot x^2 + \frac{0.0176}{\xi(0)^2} \cdot x \tag{3.20}$$

This time, if we plot the magnetic field ($H(T)$), instead of the square of it as in the previous equation, against $\frac{T_c-T}{T_c}$, which is again denoted by "x," then it is a quadratic function without intercept with the same fitting parameters with eqn. 3.19. Thus it would be easier to cut the upper critical field curve into two parts at the crossover point between strong and weak coupling limits. Then plot the part of the curve in weak coupling regime as the square of the field versus the reduced temperature so that it will be fitted with a linear function, and plot the part of the curve in strong coupling regime simply as the field against the reduced temperature to fit it with a quadratic function. Consequently, it becomes important to identify the crossover point where we shall split the $H_c(T)$ curve. In the original paper, authors suggested that this point is located at where $\frac{S^2 eH}{\hbar c} \sim 1$. However, due to the lack of knowledge of the lattice constant, $S = 2R + b$, I wasn't able to use this rule to judge the crossover point. The split point was eventually chose by simply estimation of the inflection point, and the results of our example (sample 083113) are presented in figure 3.24 and figure 3.25.

In figure 3.24, the upper and lower parts of the upper critical field curve are plotted and fitted separately, then both of the data and the fitted curves are plotted altogether in one plot in figure 3.25. The splitting point between the upper and lower parts of the curve was chosen by a rough estimation of the inflection point. The agreement between the numerical fit and the experimental data appears to be somewhat satisfying. However, the true test would be to retrieve values of testable physical quantities from the values of the fit-

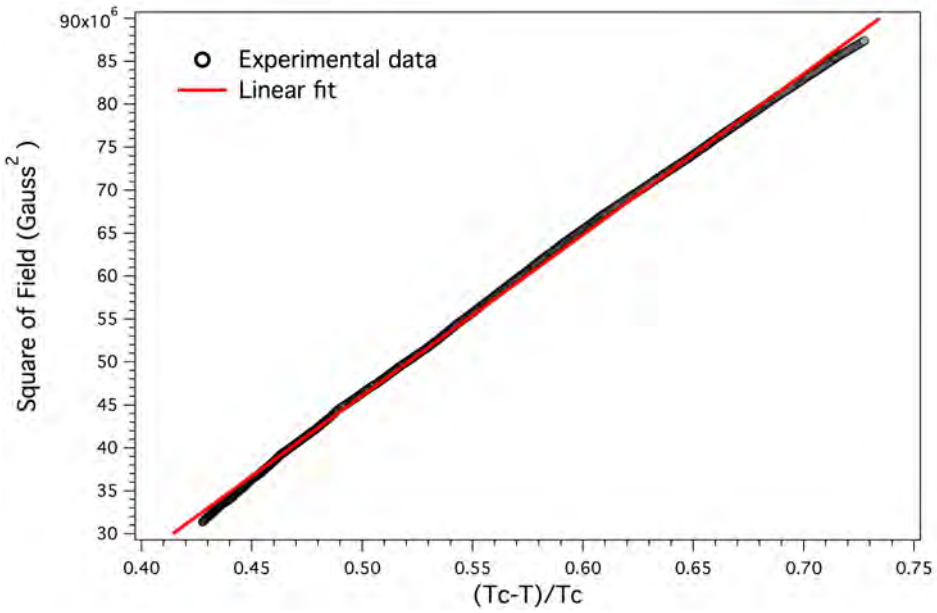

(a) The numerical fit to the part of the experimental data of sample 083113 in the strong field/weak coupling regime.

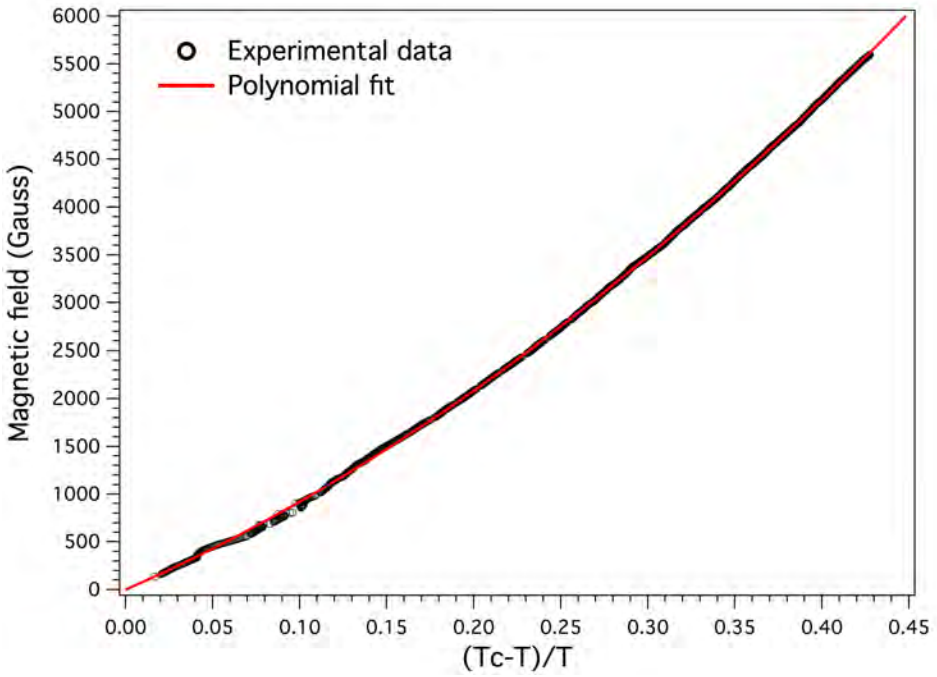

(b) The numerical fit to the part of the experimental data of sample 083113 in the weak field/strong coupling regime.

Figure 3.24: The numerical fit to the upper critical field curve of sample 083113.

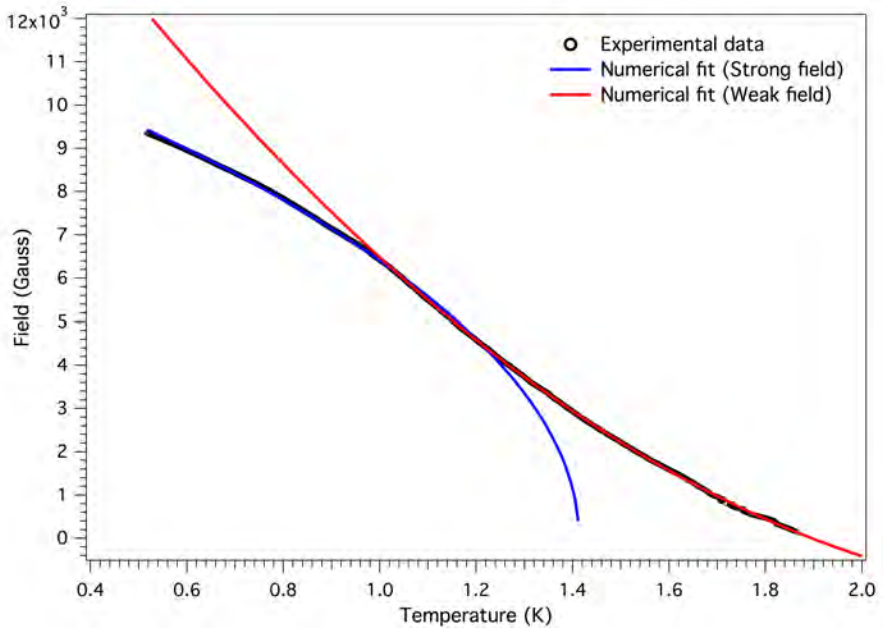

Figure 3.25: The numerical fits of both upper and lower parts of the experimental data of sample 083113 combined and plotted as the field versus reduced temperature.

ting parameters feedback from the numerical fit, and compare them with the value acquired from experiments. In the present case, the fitting parameters contained the zero-field coherence length and the lattice constant. The values returned from the numerical fits are given in table 3.3. The values obtained from the numerical fits of the two parts of the curve apparently don't agree with each other. As the origin of the discrepancies unclear to us, direct measurement of the average radius of superconducting grains (R) and average thickness of barriers (b) through TEM imaging becomes crucial in the future beyond this dissertation in testing the validity of the current theory. Lastly, I plotted, in figure 3.25, the experimental data of the upper critical field curve once again with the numerical fits to it altogether but in the most straightforward manner as plotting the field versus the temperature.

Parameter (unit)	$\xi(0)$ (cm)	R (cm)	b (cm)
Strong field part	1.96×10^{-7}	2.52×10^{-6}	5.10×10^{-5}
Weak field part	1.48×10^{-3}	7.33×10^{-10}	1.44×10^{-5}

Table 3.3: The values for fitting parameters returned from numerical fits. $\xi(0)$ is the zero-temperature coherence length, R is the average radius of the superconducting grains, and b is the average thickness of the insulating barriers.

3.4 Conclusion

Motivated by a remote hope of unraveling the mystery of granular superconductivity, I started this project two years ago in an empty lab. By the hands of my supervisor, Dr. Davis, and our almighty technician, Greg Popowich, this empty lab soon was fully renovated and equipped. Among all the intricate apparatus, there was a ^{4}He dewar that functioned both as a helium reliquefier and a part of a dipper fridge. It was on this fridge I calibrated our first thermometer, as well as then conducted co-linear four-probe-measurements using the first sample stage I designed. By setting up and operating this ^{4}He fridge, I gathered much experiences with dipper fridges in general, vacuum equipments, and programming for electronics. Furthermore, during this period of time, I had plenty of chance to learn and practice using e-gun/thermal deposition systems for sample fabrication. The knowledge and skills I picked up from this experience greatly assisted me in designing, wiring, and setting up the next fridge I used – the ^{3}He/^{4}He dipper fridge, or, the lemon fridge. With the excellent technical support provided by Greg Popowich, I soon became familiar with this new fridge once it was up and running. Though occasionally ran into problems, on this fridge, I was able to conduct not only square-four-probe-measurements of resistivity, but also that with sweeping magnetic field. Surprising and exciting results were obtained through these measurements. Although, by the end of this thesis, no effective theory was found that can adequately explain these experimental findings, we were able to confirm unequivocally enhancements of superconducting transition temperatures in Al-Ge granular films at zero magnetic field. On the other hand, we demonstrated some peculiar behaviours of the upper critical field curves for such granular superconducting films, including gradual and sharp upturns in these curves. While the task of clarifying the

reasons behind these phenomena is far from finished, we believe this has been a good start and will eventually lead us to some answers to the questions we have in our minds about granular superconductivity.

For the future development of this research project, several necessary steps to take are already clear from the current perspective. TEM imaging of each individual sample is of the most importance, since it will give us ideas about the average sizes for both the superconducting grains and insulating barriers. The information from TEM images would not only help us reduce fitting parameters, and thus improve the accuracy and reliability of numerical fits, but also allow us to further polish our skills in sample fabrication. Moreover, it is the best to take XPS measurements at multiple sampling areas on all future samples to learn the homogeneity of each sample. Last but not the least, more sample films of various metal concentrations systematically spread over a wider range should be made and tested in order to see a pattern that correlates the aluminum concentration to the superconducting transition temperature.

On the long run, we hope our current research may serve as a kick off for more comprehensive studies in granular superconductors. The purpose of our attempt in elucidating the mechanism of such systems may in the future, on the one hand, help us to a better understanding of superconductivity in general, and on the other hand, point to a possible direction to the ultimate dream of the field: room-temperature-superconductivity.

Bibliography

[1] Dirk Van Delft and Peter Kes. "The discovery of superconductivity". In: *Physics Today* 63.9 (2010), p. 38.

[2] James Annett. *Superconductivity, Superfluids and Condensates*. Oxford University Press, 2004.

[3] Y. Iwasa and J.E.C. Williams. "Direct evidence of persistent current loops in hard superconducting wire". In: *Applied Physics Letters* 9.391 (1966).

[4] A.V. Ustinov P.Müller. *The physics of superconductors*. Springer, 1997.

[5] M. Tinkham. *Introduction to superconductivity*. McGraw-Hill, Inc., 1996.

[6] H.F. Hess et al. "Scanning-tunneling-microscope observation of the Abrikosov flux lattice and the density of states near and inside a fluxoid". In: *Physical Review Letter* 62.2 (1989), pp. 214–216.

[7] V.L. Ginzburg and L.D. Landau. In: *Zh. eksper. Teoret. Fiz.* 20.1064 (1950).

[8] V. Ginzburg and L. Landau. "On the theory of superconductivity". In: *Zh. eksper. Teoret. Fiz.* 20.1064 (1950).

[9] J.Bardeen, L.N. Cooper, and J.R. Schrieffer. "Theory of superconductivity". In: *Physical Review* 108.5 (1957), p. 1175.

[10] L.P. Gor'kov. "Microscopic derivation of the Ginzburg-Landau equations in the theor of superconductivity". In: *Soviet Physics JEPT* 6.9 (1959).

[11] Q.Tang K.-H. Hoffmann. *Ginzburg-Landau Phase Transition Theory and Superconductivity*. Birkhäuser Verlag, 2001.

[12] J.R. Schrieffer. *Theory of superconductivity*. Perseus books, 1999.

[13] Y.Shapira and G.Deutscher. "Semiconductor-superconductor transition in granular Al-Ge". In: *Physical Review B* 27.7 (1982), pp. 4463–4465.

[14] G. Deutscher, O. Entin-Wohlman, and Y. Shapira. "Upper critical fields in granular superconductors". In: *Physical Review B* 22.9 (1980), p. 4264.

[15] O.F. Kammerer and M. Strongin. "Superconductivity in Tungsten films". In: *Physics Letters* 17.3 (1965), p. 224.

[16] J. Cochran and D. Mapother. "Superconducting transition in Aluminum". In: *Physical Review* 111.132 (1958).

[17] B. Abeles, R.W. Cohen, and G.W. Cullen. "Enhancement of superconductivity in metal films". In: *Physical Review Letters* 17.12 (1966), p. 632.

[18] G. Deutscher and S.A. Dodds. "Critical-field anisotropy and fluctuation conductivity in granular aluminum films". In: *Physical Review B* 16.9 (1977), p. 3936.

[19] V.L. Ginzburg. "On surface superconductivity". In: *Physical Letters* 13.2 (1964), p. 101.

[20] D. Saint-James and P.G. de Gennes. "Onset of Superconductivity in decreasing fieldsz". In: *Physics letters* 7.5 (1963), p. 306.

[21] B. Abeles, R.W. Cohen, and W.R. Stowell. "Critical magnetic fields of granular superconductors". In: *Physical Review Letters* 18.21 (1967), p. 902.

[22] R.H. Parmenter. "Size effect in a granular superconductor". In: *Physical Review* 166.2 (1968), p. 392.

[23] G. Deutscher and O. Entin-Wohlman. "Critical fields of weakly coupled superconductors". In: *Physical Review B* 17.3 (1978), p. 1249.

[24] Frank Pobell. *Matter and Methods at low temperatures*. Spinger, 2006.

[25] Jr. A. Uhlir. In: *Bell Syst. Tech. J.* 34.105 (1955).

[26] B.T.Matthias, T.H. Geballe, and V.B.Compton. "Superconductvity". In: *Review of Modern Physics* 35 (1963), pp. 1–22.

[27] H.H.Wieder. *Laboratory Notes on Electrical and Galvanomagnetic measurements*.

[28] P.G. deGennes. *Superconductivity of metals and alloys*. Perseus Books, 1999.

[29] J.A. Osborn. "Demagnetizing factors of the general ellipsoid". In: *Physical Review* 67.11 (1945), p. 351.

[30] R. Dickinson et al. *Distribution of non-uniform demagnetization fields in paramagnetic bulk solids.*

[31] R. Skomski, G.C. Hadjipanayis, and D.J. Sellmyer. "Effective demagnetizing factors of complicated particle mixtures". In: *IEEE transactions on magnetics* 43.6 (2007), p. 2956.

[32] E.P. Harris and D.E. Mapother. "Critical field of superconducting aluminum as a function of pressure and temperature above 0.3K". In: *Physical Review* 165.2 (1968), p. 523.

[33] G. Deutscher et al. "Transition to localization in granular aluminum films". In: *Physical Review Letters* 44.17 (1980), p. 1150.

[34] P.D. Desai, H.M. James, and C.Y. Ho. "Electrical resistivity of aluminum and manganese". In: *J. Phys. Chem. Ref. Data* 13.4 (1984), p. 1131.

Appendix A

Technical problems and solutions

A.1 Calibration

A.1.1 Mounting

A significant amount of effort was put in thermometer calibrations since, in my opinion, it is as important as the experiment itself. In performing calibrations for the thermometers, I encountered many problems, but with the help from my supervisor and our postdoc Xavier, we were able to tackle them one by one, and eventually have well calibrated thermometers that give temperature readings with high precisions. During the two-year-master's program, I, in total, calibrated three thermometers. However, here I only intend to provide a brief document of relevant problems and solutions if any was found, thus I not all the details of all three calibrations will be included.

In order to calibrate a thermometer, one often has to read its resistance at various temperatures using another calibrated thermometer. This requires the two thermometers to be in very good thermal contact. In our experiments, the calibrated thermometer was thermally glued into a bobbin, which was made from oxygen-free-copper (see figure A.1). In the course of usage, the surface of the bobbin will gradually be oxidized, which deteriorates its thermal conductivity. Therefore, in order to achieve as good thermal contact as possible, every time before mounting the bobbin onto the sample stage where the un-

Figure A.1: The bobbin in which a thermometer is mounted.

calibrated thermometer was also mounted, we had to use sand paper to take off the thin layer of oxidized copper from the contact face of the bobbin and that of the sample stage, clean them with diluted Ethanol solution, and then tightly mount the bobbin onto the stage.

As for the uncalibrated thermometers, usually they were buried inside of the sample stage if not in bobbins. Sometimes when the diameter of the hole in which the uncalibrated thermometer was supposed to be installed was slight bigger than that of the thermometer. In order to make sure of a tight fit, a thin piece of copper sheet was used to wrap around the thermometer, and then low-temperature thermal grease was applied to it before fitting it into the hole on the sample stage. This usually will guarantee a good thermal contact between the thermometer and the stage.

A.1.2 Data collecting

At low temperature, it in general takes much longer time for two pieces in thermal contact to strike a thermal equilibrium than it does at room temperature. Thus when changing, and reading with the calibrated thermometer, the temperature of the uncalibrated one, even though a great deal of effort was made in advance when mounting them to make sure of a good thermal contact, it may still take a long time before the two thermometers reach the same

temperature. Because of this, it is important to ramp the temperature slowly enough to allow relaxation to happen between the two thermometers. However, even a very slow ramping rate of temperature wouldn't be able to guarantee a truthful reading of the uncalibrated thermometer as that, the lower the temperature gets the poorer the thermal conduction between the two (see figure A.2). A discrepancy between the resistance measurements at low temperature when being warmed up slowly and cooled down slowly can usually reveal this point, an example is seen in figure A.3.

An even better way (in my opinion) is to take discrete measurement at different temperatures. The argument is that no matter how dense the data points are along the curve, it is never a continuous measurement, and every temperature monitor/controller will only take finite number of data points and postulate the temperature when it is not among those data points. Thus, just as what we did in calibrating the thermometer on ^{3}He dipper fridge, we warmed the two thermometers to a specific temperature and dwell at that temperature for quite some time to allow them to reach thermal equilibrium before start taking measurements of the uncalibrated sensor's resistance at this temperature for a while, then stop the measurements and move onto the next temperature to repeat the process. In the end, we take averages at each temperature and use it to generate a calibration curve. By calibrating in this way, we guaranteed the temperatures read by the calibrated sensor was the temperature of the uncalibrated thermometer since, if it was not, the data points collected at each temperature would drift away from its initial centre of the data cloud as time goes by (see figure A.4). Figure A.5 displays a zoomed in view from figure 3.4 of one set of resistance measurements of the uncalibrated sensor at a specific temperature, from which as we can see although the temperature fluctuation would stretch the shape of the data cloud, the long dwelling time assures that the corresponding change in the resistance of the uncalibrated sensor also to be recorded.

Upon finishing collecting all the data clusters at various temperatures, an average value was calculated for each cluster to be used for interpolation, and eventually a continuous calibration curve.

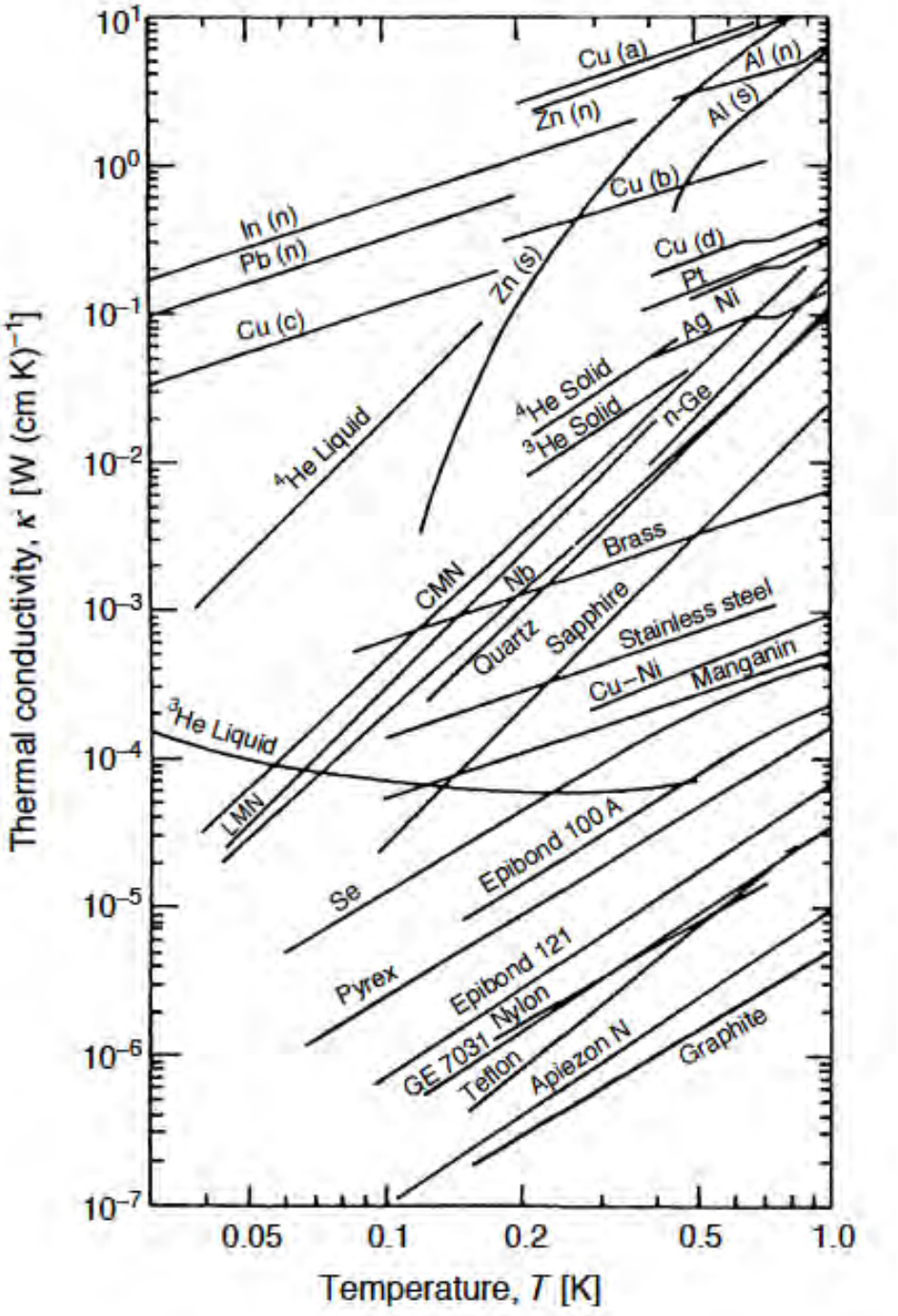

Figure A.2: Thermal conductivity of various materials. Figure credit to ref. [24]

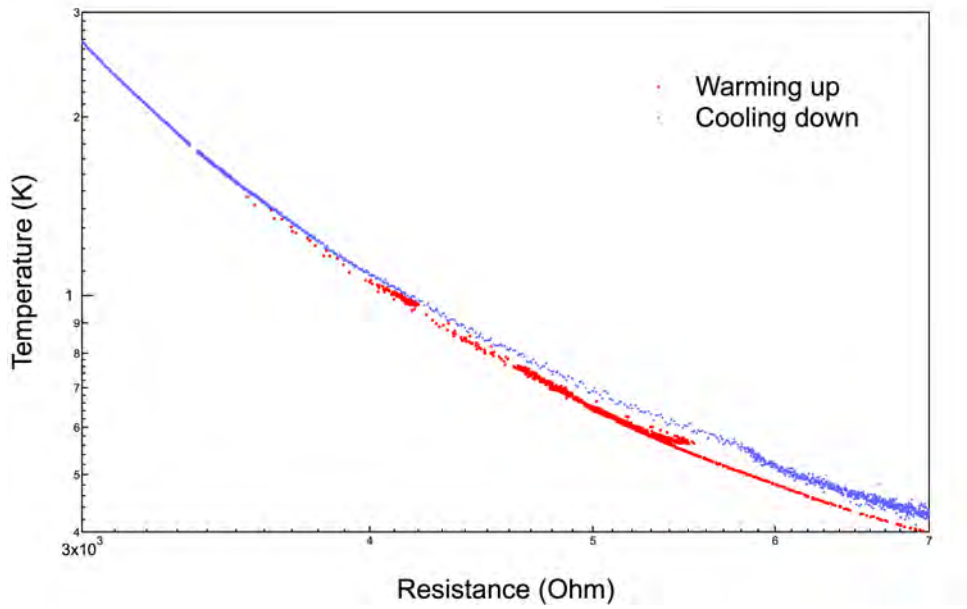

Figure A.3: The discrepancy between measurements of the same sample (uncalibrated thermometer) when being warmed up and cooled down indicates a temperature difference between the calibrated thermometer and the uncalibrated one.

A.2 Substrate

For quite sometime, I was struggling with my experiments for the substrate problem. This section is thus dedicated to the description of the problem and the solution in the end. In order to achieve a good thermalization on the substrate, the importance of which goes without saying, the initial design of the material of the substrate used on ^{3}He dipper fridge was oxygen-free copper. It was machined to be circular shaped, whose diameter was of precisely the size of the sample stage (see figure A.6(a)), and of only few millimetres thick. A mask was made for such substrates to restrict the size and area of the sample when they were deposited (see figure A.6(b)).

Though being made from copper guarantees a good thermal conduction at low temperature, the problems come in as it is electrically connected to our superconducting sample if we directly deposit the film on top of the substrate. Therefore, it is necessary to create a thin insulating layer between the copper substrate and the sample so that it is thin enough to allow heat transfer at low temperature from the sample to the substrate, but at the same time electrically separate the two. In practice, this became very difficult as when attempting to

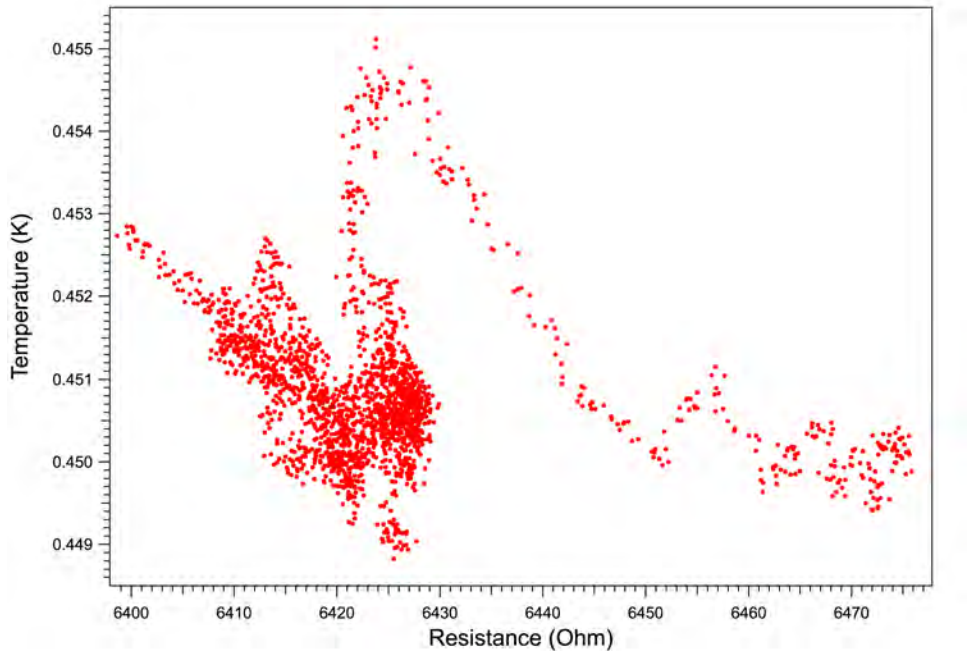

Figure A.4: A cluster of data points of the resistance of an uncalibrated thermometer at 450 ± 3 mK. From the shape of the data cluster, a drift in resistance of the uncalibrated sensor can be observed, which appeared to be uncorrelated to the temperature fluctuation. This was due to that the deteriorated thermal conduction at low temperature resulted in a prolonged time to strike a thermal equilibrium between the two sensors. Thus the temperature read, at the beginning, by calibrated thermometer can not reflect the true temperature of the uncalibrated thermometer for quite sometime until they both relaxed to the same temperature.

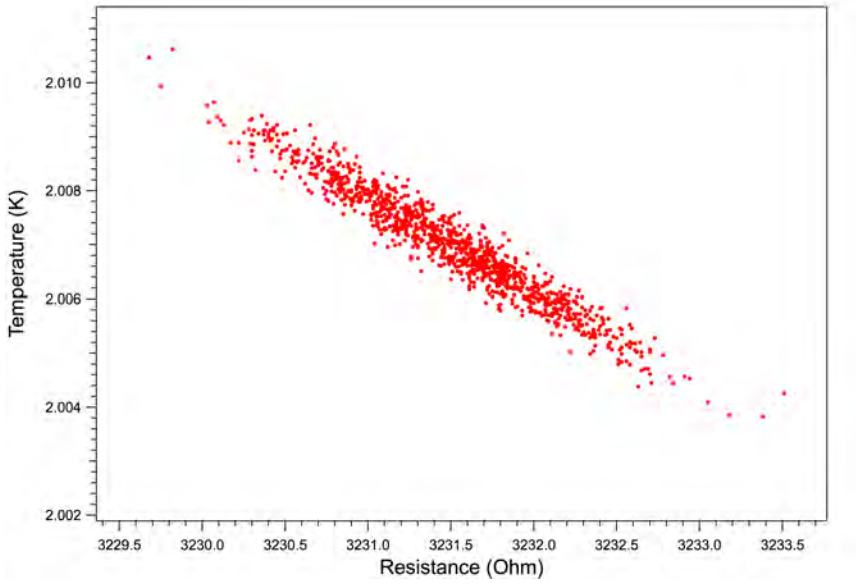

Figure A.5: A cluster of data points of the resistance of an uncalibrated thermometer at 2.007 ± 0.003 K.

(a) The piece on the left side is a copper substrate made for the sample stage used in ^{3}He dipper fridge. The three clearance holes are for substrate mounting, and the dents on the edges were designed for the convenience of running wires through. The piece on the right side by the substrate is a washer used to mount the substrate onto the sample stage.

(b) The mask used on top of substrates during depositions to restrict the size and position of the area on where the sample film would be deposited.

Figure A.6: The copper substrate, copper washer made for the ^{3}He fridge, and the mask used for deposition.

deposit a thin insulating layer ($\sim 2\ \mu$m) of SiO_2, it wouldn't stick to the copper substrate even when the surface of the substrate was polished with fine sand paper and Brasso®. Thus I would have to first deposit an adhesion layer onto the substrate first, which was either chrome (see figure A.7(a)) or titanium (see figure A.7(b)) usually of less than 30 nm thick, and then deposit SiO_2 on the adhesion layer.

(a) The copper substrate with an adhesion layer of chrome deposited on it.

(b) The copper substrate with an adhesion layer of titanium deposited on it.

Figure A.7: The copper substrate with different adhesion layer materials deposited on it.

After depositing the adhesion layer and the insulating layer, the sample film was deposited on top. However, a new problem showed up as, apparently there were some tiny tunnels in the SiO_2 insulating layer, and when the film was deposited onto the layer, the material of the film will get into these tunnels and reach the adhesion layer underneath it, which is metallic, thus create an electrical short between the sample film and the substrate. It was later turned out that this is not something new at all but rather a prominent problem in semiconductor industry. Those small tunnels were called "pin holes", and the reason of their formation was due to either presence of impurities or "bumps" on the flat surface or lattice mismatch. In both scenarios, the deposited material will regard them as disturbance and won't stick to them, but instead, "grow" around them, and eventually form a channel centred at the spot. Since, in my case, the SiO_2 was amorphous and the copper substrate was by no means sin-

gle crystal, the later reason appears less compelling comparing to the former. However, due to the restriction of accessibility, we could not process the copper substrates in a clean room before depositing insulating layers. But, it occurred to me that since the sample material (aluminum) can go into these channels, it means that I can fill these pin holes up with aluminum first, and if I can oxidize the aluminum afterwards to turn it into Al_2O_3, which is an insulator, then I should be able to electrically isolate the subsequently deposited sample film.

Later this idea was implemented during a deposition with aid of an oxygen background created using the gas nozzle installed at the back of the bell jar in the e-gun/thermal deposition system (see figure 2.5(d)). However, it didn't turn out working well as, on the one hand, I wasn't able to thoroughly oxidize the aluminum in the tunnel, and, on the other hand, the idea of a close contact between aluminum oxides layer and aluminum-germanium film (the sample film) could be problematic as it may create a different system than the one we intended to study. Thus this idea was abandoned eventually, and a new substrate was adopted.

The new substrate was designed to be made of single crystal silicon, it was of less than one millimetre thick. At low temperature, silicon was considered electrically yet not thermally insulating. In making such a substrate, I decided to cut it out from a piece of silicon wafer as it was among the most accessible and economic materials (see figure A.8(a)). However, because it was near impossible to cut a piece off in circular shape from the wafer, it was thus then scribed off as a triangle piece (see figure A.8), which conforms the symmetry of the sample cell design (mostly due to the three threaded rods that hold all parts together). A mask was made subsequently for film deposition (see figure A.8(c)), and the size of the deposition area was made the same as previous. However, in the end, this design of substrate was abandoned as well when a new better design came into being, which was the one described in chapter 2 and used throughout the entire program since then.

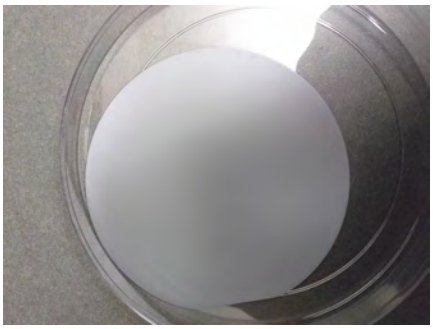

(a) A photo of a complete single crystal silicon wafer, which is a very common in semiconductor industry and easy to purchase.

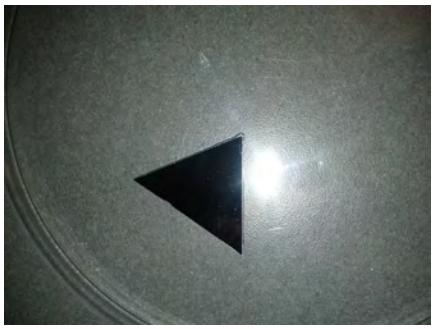

(b) The triangle shaped silicon substrate cut out from a silicon wafer.

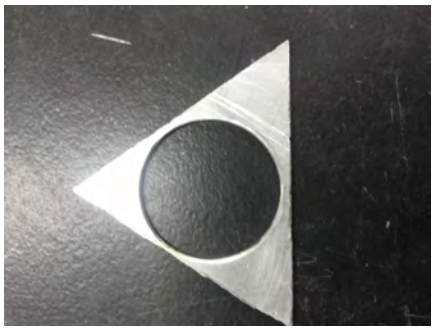

(c) The mask made for the triangle shaped silicon substrate to restrict the size and the position of deposition area.

Figure A.8: Photos of one of the experimental designs for substrates.

Although a new substrate solved one problem, another persisted. The design of using four pogo pins to take resistance measurements required that the pins are pressed against the sample film for electric conductance as well as thermal conductance since, with the new 1/16-inch quartz substrate, this was the only way of thermalizing the sample. It turned out that even though the pressure from those spring-loaded pins was very gentle, they can scratch the sample film easily and damage the sample (see figure A.9(a)). In the worst scenario, it can cause cause the electrical circuit to break as it penetrates the whole film and making contacts with nothing but only the surface of the insulating substrate.

One of the solutions was to remove this pressure entirely by, instead of

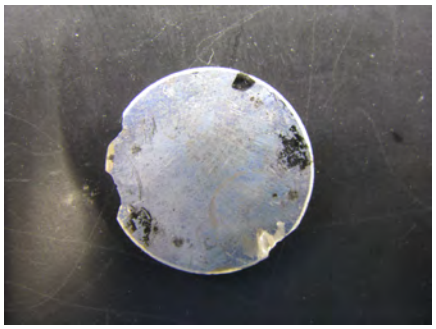

(a) A sample film scratched/pierced by the pogo pins when they were pressed against it to take measurements. In some worst cases as in the photo presented here, the pressure can even break the quartz substrate.

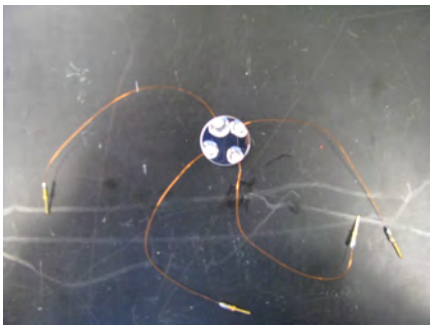

(b) A sample film with four striped copper wires attached to it as leads to take resistance measurements. The wires were glued to the substrate with silver paint and then stycast epoxy for reinforcement of strength. On the other end of each copper wire was a quick connector soldered to it for the convenience of changing sample.

Figure A.9: A technical problem caused by the pogo pins and one of the solutions.

using pogo pins, using striped copper wires as leads to be attached to the sample films, glue them with silver paint for electrical conduction, and then apply epoxy onto them to release pressure and strengthen the connection. Though this method works perfectly fine, it causes trouble in calculating the resistivity from resistance measurement as it is very difficult to make sure point contact between the lead and the film, and to arrange them into a square shape.

Another solution, which was eventually adopted for all the measurements, was much simpler. Instead of removing the pressure from the pogo pins, I tried to lessen the stress on the film by applying silver paint, as landing pads, to points of contact on the sample film prior to pressing the pins against it. This method turned out to be very effective in eliminating the chance of pogo pins penetrating the film with the additional advantage of preserving the design of using aligned pogo pins for measurements.

A.3 Concentration variation by thermal deposition

As mentioned before in chapter 2 that, due to the fact that the source for thermal deposition is located not right under the substrate, but rather on the side (see figure A.10), it results in a variation of the material concentration in the final product. Here in this part of the appendix, I will try do demonstrate how I quantitatively estimated this variation.

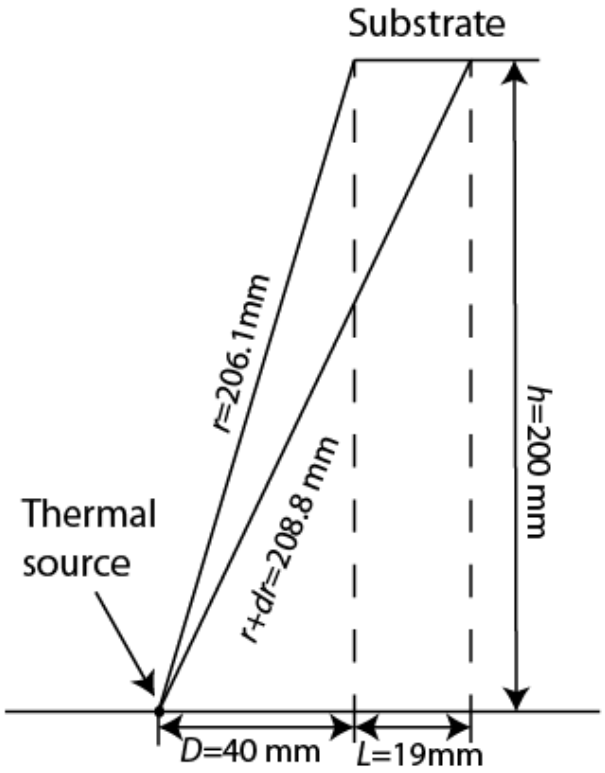

Figure A.10: A schematic illustration of the location of the thermal deposition system used in our experiments.

Consider the setup illustrated in figure A.10, where the source is on the side below the substrate ("$h = 200$ mm" stands for the vertical distance) at some distance (*e.g.* $D \sim 40$ mm). The length "$L = 19$ mm" stands for the diameter of the substrate. "r" is the distance from the thermal source (germanium in our case) to the closer edge of the substrate, and "$r + dr$" stands for

that from the source to the further edge of the substrate. The corresponding material concentration at these two edges are denoted by "C_n" and "C_f" respectively, where "n" is intended to mean "near by", and "f" means "far side".

By applying Pythagorean theorem to the scheme, we have:

$$r = \sqrt{h^2 + D^2} = 206.1\text{mm}, \text{and} r + dr = \sqrt{h^2 + (D + L)^2} = 208.8\text{mm}. \quad \text{(A.1)}$$

This results in $dr \sim 2.7$ mm. Now if we consider the thermal deposition process as if a radiation process, then it wouldn't be hard for us to picture that, at a given steady evaporating rate R_e, the deposition rate (R_d) at a distance of r from the source is given by: $R_d(r) = \frac{R_e}{4\pi r^2}$. Therefore, the concentration ratio between the parts of the film on the near by edge (C_n) and on the far side edge (C_f) is determined as:

$$\frac{C_n}{C_f} = \frac{R_{dn}}{R_{fn}} = \left(\frac{r + dr}{r}\right)^2. \quad \text{(A.2)}$$

This correlation between the difference in the material concentration and that in the distances from the two edges to the source eventually gives $\frac{C_n}{C_f} \sim 102.6\%$, meaning a 2.6% concentration difference is introduced in the final product. In our opinion, this is a rather small contribution to the inhomogeneity.

A.4 Programming

A.4.1 Wiring

The very first problem I encountered was to even connect the equipments to a computer. While it was not difficult the Cryocon®temperature controller and Lakeshore AC resistance bridge to link since they were designed to use serial and GPIB card for communication respectively, connecting to model 430 power supply programmer for the magnet in ^{3}He fridge wasn't an easy task as it employs 10/100Base-T Ethernet interface, uses either static or dynamic IP address, subnet mask, and gateway IP address. If the computer that collects data is to be connected to model 430 programmer through a network, then the

ethernet cable should be straight-through (standard) type, yet if the computer is to be directly connected to model 430, then the cable has to be of "null-modem" ("crossover") type.

Pin number	Colour code	Pin number
1	orange	3
2	orange/white	6
3	green/white	1
4	blue/white	7
5	blue	8
6	green	2
7	brown	4
8	brown/white	5

Table A.1: Configuration of pins for EIA/TIA T568B "crossover" ethernet cable, the number indicates the order of pins.

In our experiment, the current setup connects the computer to the model 430 directly, thus we had to use a home-made "crossover" ethernet to do so. Unlike the "straight-through" ethernet cable that the 8 pins go through the cable without switch positions, the order of pins on the two ends of a "crossover" ethernet are not the same, and there are many different ways of reordering, eventually, I found out that the EIA/TIA T568B cable works for the system and its configuration is illustrated in table A.1. With this home-made cable, we were then able to connect and communicate with the model 430 power supply programmer to perform operations with the magnet installed inside the ^{3}He fridge.

A.4.2 Data collecting

Usually when using a computer to collect data from a piece of equipment, the basic process can be described as that: the computer sends a command that triggers the equipment to output a piece of information to its buffer, and the computer copies this piece of information to its memory from the equipment's buffer and display it to the screen or write it to a file. Normally, the information

is the complete answer to the computer's inquiry and it takes only a small fraction of second to complete such a task, this is the case for both Cryocon®44C temperature controller and Lakeshore®model 370 AC resistance bridge. However, the model 430 power supply programmer does this task in a very unusual way: when the model 430 programmer receives an inquiry, it doesn't write the whole answer to the buffer at once but rather bit by bit. For example, when the computer asks model 430 programmer a question such as "what's the current strength of magnetic field?", instead of replying by writing to its buffer the value (*e.g.* 137.0359...), it only writes one digit (in the present case, "1") at a time, only after that digit was read by the computer, it writes the next digit ("3") and thus forth, when all the digits are written, then the last bit will be a linefeed that hints the computer this is the end of the answer. Therefore, a program that would normally works for most of the equipment wouldn't work for model 430 programmer as it will only be able to extract one digit of the whole value when collecting data. In order to overcome this inconvenience, eventually, I wrote a program that uses a while loop to read the value bit by bit until being terminated by the condition of reading a linefeed.

Another problem with data collecting was how to display the data. In order to have a computer to display a piece of information, it requires the computer to store this information in its random-access memory (RAM) to show it on the screen. In our case, when plotting a curve on the screen, the computer will store a coordinate system as well as the corresponding coordinates of each data point from the curve in its RAM, and then find its position on the screen to display. Usually, this isn't really a problem since modern PCs have enormous random-access memory (RAM). Take the computer we've been used for data collecting, it has 2 GB RAM, which, in another word, can store 10^9 bits of information, in equivalent of one million three-digit-numbers. However, when taking the 3D measurements of the phase diagram of superconductors, one measurement usually takes around 60 hours non-stop, and the sheer number of data points were too much for the computer that it eventually will cause the program either to crush or to slow down significantly.

This problem was eventually solved in two ways: one was that I just simply stopped showing data on the screen since storing it to a file doesn't require

showing them real-time. Another ways was to create a FIFO (first-in first-out) array to display the data, once the number of data points exceeds the preset limit, the next data input would replace the another one that was first displayed. In this way, there will be always a finite number of elements in the data array, and thus the occurrence of memory leak was prevented.